Diplomarbeit

Sapphire capillaries for laser-driven wakefield acceleration in plasma

fs-laser micromachining and characterization

Jan-Patrick Schwinkendorf

Hamburg, May 2012

Universität Hamburg
Fachbereich Physik
Institut für Experimentalphysik

Saphirkapillaren für die Laser-Plasma-Beschleunigung

fs-Lasermicromachining und Charakterisierung

Referees
Dr. Jens Osterhoff
Prof. Dr. Jörg Roßbach

This exposition was compiled with LyX and KOMA-Script.

Abstract

Plasma wakefields are a promising approach for the acceleration of electrons with ultrahigh (10 to 100 GV/m) electric fields. Nowadays, high-intensity laser pulses are routinely utilized to excite these large-amplitude plasma waves. However, several detrimental effects such as laser diffraction, electron-wake dephasing and laser depletion may terminate the acceleration process. Two of these phenomena can be mitigated or avoided by the application of capillary waveguides, e.g. fabricated out of sapphire for longevity. Capillaries may compensate for laser diffraction like a fiber and allow for the creation of tapered gas-density profiles working against the dephasing between the accelerating wave and the particles. Additionally, they offer the possibility of controlled particle injection.

This thesis is reporting on the set up of a laser for fs-micromachining of capillaries of almost arbitrary shapes and a test stand for density-profile characterization. These devices will permit the creation of tailored gas-density profiles for controlled electron injection and acceleration inside plasma.

Zusammenfassung

Laser-Plasma-Beschleunigung ist eine vielversprechende neue Beschleunigertechnologie, welche extrem hohe elektrische Feldstärken von 10 bis 100 GV/m liefert. Heutzutage sind die technischen Rahmenbedingungen gegeben, um durch hochintensive Laserpulse starke Plasmawellen zu treiben. Allerdings treten dabei einige störende Eigenschaften auf, die den Beschleunigungsprozess beenden: Divergenz des Laserstrahls, Auseinanderlaufen der Phasenbeziehung zwischen Elektronen und Plasmawelle sowie die Leistungsabnahme der propagierenden Laserpulse. Die ersten beiden Phänomene können dabei durch den Einsatz von kapillarartigen Wellenleitern verhindert oder zumindest abgeschwächt werden. Für eine möglichst lange Lebensdauer werden diese aus Saphir gefertigt. Die mit Gas gefluteten Kapillaren können zum Einen die Divergenz des Laserstrahles wie eine Faser kompensieren und gestatten es zum Anderen konische Profile der Gasdichte zu erzeugen, die dem Auseinanderlaufen von Elektronen und beschleunigender Welle entgegen wirken. Außerdem ermöglicht ihr Einsatz eine kontrollierte Teilcheninjektion.

In dieser Arbeit wird über den Aufbau eines Lasers zur fs-Microstruktur-Herstellung von Kapillaren mit nahezu beliebigen Formen und einem Prüfstand für die Charakterisierung der Dichteprofile berichtet. Diese Anordnungen werden es ermöglichen strukturierte Profile der Gasdichte für die kontrollierte Injektion von Elektronen und die Beschleunigung innerhalb des Plasmas herzustellen.

Contents

List of Figures

List of Tables

1. Introduction

Particle accelerators deliver high-energy particle beams. These are used for either tunable light sources, such as synchrotrons or free-electron lasers (FELs) in life science and material science, or collider experiments in particle physics. Conventional particle accelerators are limited in their maximum electric field gradients to about 0.1 GV/m due to electric or thermal breakdown [Sol09]. In order to reach ever higher energies the facilities had to grow in size (km-scale) and became more and more expensive (billions). As a result the Large Hadron Collider (LHC) near Geneva and the European X-Ray Free-Electron Laser (XFEL) in Hamburg could only be realized in collaborations of many different nations. The next generation of particle accelerators will thus require even higher energy levels at still affordable costs.

In 1979 Tajima et al. [TD79] proposed plasma wakefield acceleration (PWA), based on high power lasers, which required at that time non-existing laser technology. Meanwhile this has developed into a promising approach for acceleration physics delivering ultrahigh electric field strengths of about 10 to 100 GV/m [LNG$^+$06]. Thereby allowing the construction of much smaller devices which will potentially also reduce the costs.
For the development of plasma based colliders there are several problems, for example staging of single accelerator modules, which have to be solved in order to construct a smaller-sized, possibly more powerful and more cost efficient PWA based accelerator. Therefore, this development will require significant time.
Nevertheless, there might also be practical applications of plasma wakefield acceleration realized in the near future. In 2007 Grüner et al. [GBS$^+$07] presented a design of a table-top free electron laser (TT-FEL) based on a PWA source. Due to ultrashort electron bunches in the fs-scale and high peak power they suggested a meter-scaled miniature undulator to be sufficient for a capable free electron laser. So the dimension of a FEL might be reduced from kilometer to meter scale allowing smaller institutes, e.g. universities, to own their own FEL instead of applying for beamtime at a big research center to use the on-site facilities.

2. Theoretical Principles

2.1. Light and Laser

2.1.1. Light fundamentals

Light can be described as either an electro-magnetic wave or as a particle, termed photon. The characteristic quantities of the wave are the electric and magnetic field $\vec{E}$ and $\vec{B}$, which are generally space $\vec{r}$ and time t dependent. Using the vector potential $\vec{A}$ and the scalar potential Φ these fields can be expressed as follows [Jac75]:

$$\begin{aligned} \vec{E} &= -\frac{\partial}{\partial t}\vec{A} - \vec{\nabla}\Phi \\ \vec{B} &= \vec{\nabla} \times \vec{A} \end{aligned} \tag{2.1}$$

Taking into account the Lorenz gauge the Maxwell equations deliver the wave equations which must be fulfilled by the potentials:

$$\begin{aligned} \Box\vec{A} &= \tfrac{1}{c^2}\tfrac{\partial^2}{\partial t^2}\vec{A} - \vec{\nabla}^2\vec{A} = \mu_0\vec{j} \\ \Box\Phi &= \tfrac{1}{c^2}\tfrac{\partial^2}{\partial t^2}\Phi - \vec{\nabla}^2\Phi = \tfrac{\rho}{\varepsilon_0} \end{aligned} \tag{2.2}$$

The constants c, ε_0 and μ_0 are the vacuum speed of light, the electric permittivity of free space and the vacuum magnetic permeability, respectively. They are related through $c = (\varepsilon_0\mu_0)^{-1/2}$. Furthermore, ρ describes a charge density and $\vec{j}$ represents an electric current density. A solution of (2.2) propagates with c and in the absence of any charge and current can be given as:

$$\vec{A}(\vec{r},t) = \vec{A_0}\cos\left(\omega t - \vec{k}\cdot\vec{r} + \phi\right) \tag{2.3}$$

This expression describes a plane wave. The amplitude and the polarization is determined by $\vec{A_0}$. The wave propagation direction is defined by the so-called wave vector $\vec{k}$. The angular frequency $\omega = 2\pi f = 2\pi c\lambda^{-1}$ defines the frequency f and the wavelength λ. ϕ represents an absolute phase offset. Under the assumption of charge and current free space the solution of the vector potential is equivalent for the wave equation of the scalar potential Φ because of the coupling by the applied gauge.

Hence, it is possible to obtain simple expressions for the electric and magnetic fields by taking into account (2.1) and (2.3):

$$\begin{aligned}\vec{E}(\vec{r},t) &= \vec{E}_0 \sin\left(\omega t - \vec{k}\cdot\vec{r} + \phi\right)\\ \vec{B}(\vec{r},t) &= \vec{B}_0 \sin\left(\omega t - \vec{k}\cdot\vec{r} + \phi\right)\end{aligned} \tag{2.4}$$

The electric and magnetic field amplitudes are related to the vector potential amplitude by $|\vec{E}_0| = c|\vec{B}_0| = \omega|\vec{A}_0|$. From the Maxwell equations it follows that $\vec{E}\perp\vec{B}$, $\vec{B}\perp\vec{k}$ and $\vec{E}\perp\vec{k}$. The latter is not valid anymore in the case of optical anisotropy. The combination of (2.2) and (2.3) yields the dispersion relation for light in vacuum:

$$|\vec{k}|^2 = \frac{\omega^2}{c^2} \tag{2.5}$$

Electro-magnetic waves do not need a carrier media like other waves to transport their energy. The energy flux density is given by the Poynting vector [Poy20]:

$$\vec{S} = \varepsilon_0 c^2 \left(\vec{E}\times\vec{B}\right) \tag{2.6}$$

The corresponding intensity I may be found by temporal averaging over one oscillation period of the fields in (2.6) and using the relationship between $\vec{E}$- and $\vec{B}$-field:

$$I = \left\langle|\vec{S}|\right\rangle = \varepsilon_0 c \left\langle|\vec{E}|^2\right\rangle \tag{2.7}$$

Generally, the intensity is expressed as $I = W_L\left(A_L\tau_L\right)^{-1}$. $W_L$is the energy transported by a light wave during the time τ_L through an area A_L. Nowadays high power laser systems can reach intensities at the focus of more than $10^{18}\,\mathrm{W\ cm^{-2}}$. Comparing this intensity value with (2.7) derives an electric field strength in the focal area of about $2\cdot10^{12}\,\mathrm{V\,m^{-1}}$. This electrical field strength is significantly higher than the fields inside a hydrogen atom tying an electron to the core ($\sim 5\cdot10^{11}\,\mathrm{V\,m^{-1}}$).
As mentioned before light might also be described as a particle. Electro-magnetic waves interact with their environment by exchanging energy only in discrete quantities [Pla01, Ein05]. This discrete quantity, the energy of a photon E_{Ph}, can be defined by the wavelength or the angular frequency, respectively:

$$E_{Ph} = \hbar\omega \tag{2.8}$$

with $\hbar$ the reduced Planck constant. The visible light spectrum ranges from $\lambda = 800\,\mathrm{nm}$ in the red to $\lambda = 400\,\mathrm{nm}$ in the blue. This corresponds to a photon energy range of 1.5 eV - 3.1 eV (cf. (2.8)). Today's laser systems store several joules of energy within a few tens of femtoseconds reaching peak powers $P = W_L\tau_L^{-1}$ of more than 100 TW. Therefore the number of photons in a 800 nm light pulse, such as in frequently employed titanium sapphire systems, can be estimated to be on the order of 10^{19}.
Besides energy, the photons also carry quantized momentum [Ein09]:

$$\vec{p}_{Ph} = \hbar\vec{k} \tag{2.9}$$

2.1.2. Light matter interaction

2.1.2.1. Particles in electro-magnetic fields

The equation of motion for a free electron in a light field is given by the Lorentz force [Max61]:

$$m_e \frac{d}{dt}(\gamma \vec{v}) = -e\left(\vec{E} + \vec{v} \times \vec{B}\right) \tag{2.10}$$

Here m_e, e and $\vec{v}$ are the mass, charge and velocity of the electron, respectively. The relativistic factors are $\gamma = (1-\beta^2)^{-1/2}$ and $\beta = |\vec{v}|\, c^{-1}$. For non-relativistic velocities $\gamma \approx 1$ and the $\vec{v} \times \vec{B}$ term is negligible due to $\left|\vec{B}\right| = \left|\vec{E}\right| c^{-1}$ (cf. sec. 2.1.1). Hence (2.10) reduces to $m_e \frac{d}{dt}\vec{v} = -e\vec{E}$. Integration easily yields the electron velocity:

$$\vec{v}(\vec{r},t) = -\frac{e}{m_e}\int \vec{E}_0(\vec{r},t) \cdot \sin\left(\omega t - \vec{k}\vec{r} + \phi\right) dt + \vec{v}_0 \tag{2.11}$$

$\vec{v}_0$ is the initial electron velocity, which generally will be set to zero for simplicity. The energy of the quivering electron in the light field is defined as $E_q = \frac{1}{2} m_e |\vec{v}|^2$. The time-average over one oscillation of E_q leads to the ponderomotive potential:

$$U_P = \langle E_q \rangle = \frac{e^2}{4 m_e \omega^2} |\vec{E}_0|^2 \approx 9.33 \cdot 10^{-6} I \lambda^2 \text{ in eV} \tag{2.12}$$

This utilizes the slowly varying envelope approximation which implies that the amplitude of the electric field $\vec{E}_0(\vec{r},t)$ must not change significantly on the time scale of the field. From the ponderomotive potential U_P the ponderomotive force $\vec{F}_P = -\vec{\nabla} U_P$ can be derived. This force is directed perpendicular to the laser propagation direction towards lower intensities of the laser envelope. Thus electrons will be pushed aside of the laser focus. Remember these conclusions are valid for sub-relativistic accelerations and slowly varying envelopes. A more rigorous explanation can be found in [BMS95, SM97, QM98] but does not relieve the understanding of this topic.
To determine the relative electro-magnetic pulse strength and therewith the relativistic effects of the light-matter interaction the normalized vector potential is defined as [Gib05]:

$$a_0 = \frac{e|\vec{A}|}{m_e c} \approx 8.5 \cdot 10^{-6} \sqrt{I}\lambda \tag{2.13}$$

The latter results from (2.7) and the relations of electric field and vector potential as well as angular frequency and wavelength. If the kinetic energy gain of an electron in half a light wave oscillation is comparable to its rest mass equivalent energy $E_{rest} = m_e c^2$ then a_0 is equal to unity. Consequently $a_0 = 1$ displays the threshold

in between the sub-relativistic $a_0 \ll 1$ and the relativistic case $a_0 \gtrsim 1$. Present-day systems exceed this characteristic value by achieve ultra-high laser intensities of more than

$$I_{rel} \overset{(2.7)}{=} \frac{\varepsilon_0 c}{2}|\vec{E}|^2 = \frac{\varepsilon_0 c}{2}\omega^2|\vec{A}|^2 \overset{a_0=1}{=} \frac{2\pi^2\epsilon_0 m_e^2 c^5}{e^2\lambda^2} \approx 1.37 \cdot 10^6 \lambda^{-2}\,\mathrm{in\,W\,cm^{-2}}$$

In cases of such high intensities the $\vec{v} \times \vec{B}$ simplification in (2.10) is no longer applicable any more. Hence, the electron motion will be influenced by an additional electro-magnetic force component directed along the propagation axis $\vec{k}$ of the laser beam. Compared to the non-relativistic regime the electron will then be ejected under an angle Θ against $\vec{k}$ of less than 90°. This angle Θ may be estimated by comparing the momentum components perpendicular $p_\perp$ and parallel $p_\parallel$ to $\vec{k}$ [Ost09]:

$$\tan\Theta = \frac{p_\perp}{p_\parallel} = \sqrt{\frac{2}{\gamma - 1}}$$

This result was verified by [MKM95, Mey97] in both experiments and simulations. In the case of small angles Θ an ultra-relativistic electron can be caught in the laser field and travel nearly parallel with the pulse over a long distance thus being accelerated to energies exceeding 1 GeV [WHY+01]. This does not contradict the Lawson-Woodward Theorem [Woo47, Law79] which prohibits net energy gain by electro-magnetic field interaction, because the underlying restrictions are not fulfilled unlike within the infinite interaction region.

2.1.2.2. Ionization

Powerful lasers provide intense laser pulses and strong fields for the ionization of atoms. This entails the production of plasma which is used for wakefield acceleration and observable during laser machining. It has to be distinguished between two interaction-strength dependent ionization cases. The Keldysh parameter is defined as [Kel65, PPT66]

$$\gamma_K = \sqrt{\frac{I_P}{2U_P}}$$

This describes the ratio of the atomic ionization potential I_P to the ponderomotive potential of the electromagnetic field U_P and for this reason categorizes the strength of the ionization process. If $\gamma_K > 1$ the electric field inside the atom is not significantly modified by the light field. The electromagnetic wave can be treated as a small perturbation of the atomic Coulomb potential. In this case multi-photon ionization will occur. For $\gamma_K \ll 1$ the bound electron states may escape from the atom either by tunneling through the deformed Coulomb barrier or by escaping over the distorted potential walls. Hence the perturbative approach is not valid anymore. These processes are termed tunnel or barrier-suppression ionization (BSI).

With (2.12) and a first ionization step of typically $I_P \sim 20\,\mathrm{eV}$ an intensity of the order $I \sim 10^{14}\,\mathrm{W\,cm^{-2}}$ can be estimated for $\gamma_K = 1$, therefore for intensities higher than this the latter process can be assumed to dominate.

Multi-photon ionization

If the light does not notably change the electron binding potential, ionization by a multi-photon process will occur. Usually an atom interacts with a single photon which excites an internal electron state. But for the complete release of an electron from its bound atomic state, the amount of energy a single photon is carrying E_{Ph} is not large enough in the visible light spectrum (cf. (2.8)). Therefore an initial bound electron state $|i\rangle$ has to absorb N photons of frequency ω to cross the border of the ionization potential I_P. Thus the condition $N\hbar\omega > I_P$ has to be fulfilled in order for the electron to reach the final free state $|f\rangle$ (cf. Fig. 2.1). The probability of occurrence for this mechanism depends on the photon density respectively the intensity. Through perturbation theory the corresponding ionization rate is given by [MM91]

$$\Gamma_{i\to f} = \sigma^{(N)}_{i\to f} I^N$$

taking into account Fermi's golden rule for the cross-section $\sigma^{(N)}_{i\to f}$ [Dir27, Fer50].

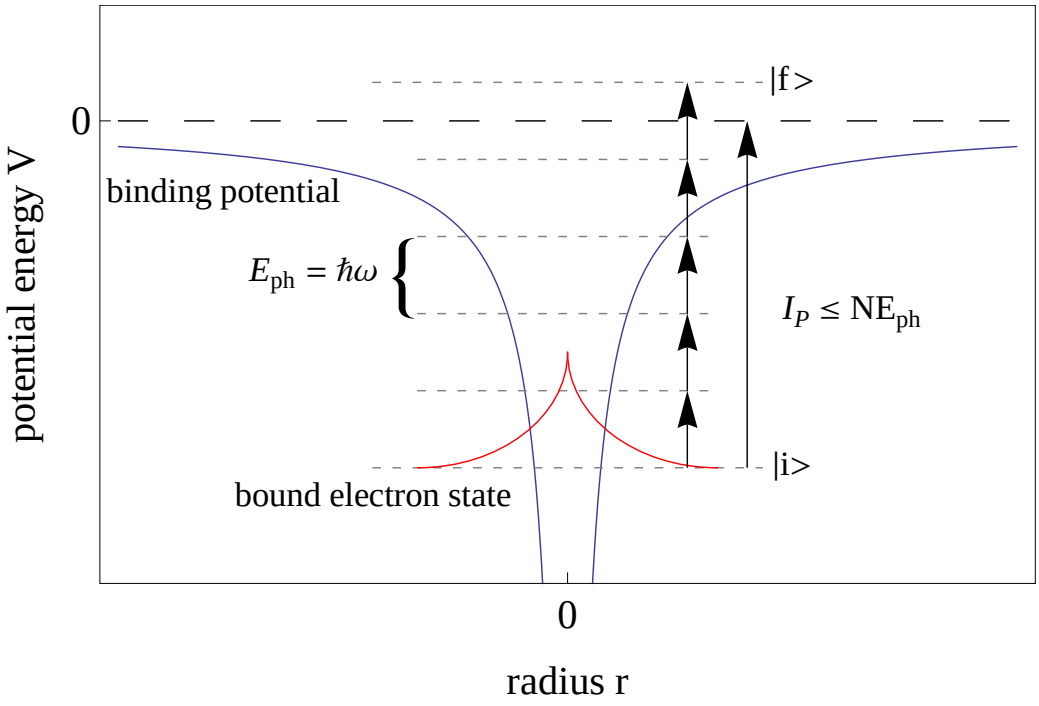

Figure 2.1.: Multi-photon ionization is a process in which an atomic bound electron is shifted from its initial state $|i\rangle$ to the final unbound state $|f\rangle$ passing over the ionization potential $I_P < NE_{Ph}$ by absorbing N photons of energy E_{Ph}.

Tunnel ionization and Barrier suppression ionization (BSI)
If an incoming light wave significantly modifies the electric field of an atom the applied perturbation theory is no longer appropriate. The electromagnetic light field cannot be seen as a disturbance because it is actively changing the shape of the Coulomb potential. Thereby the potential barriers are varied in a way the electron perceives a lesser binding probability due to a finite wall thickness on one side and thus is able to tunnel through the bend potential branch (cf. Fig. 2.2). Applying the WKB-approximation [Wen26, Kra26, Bri26] the interaction leading to the tunneling process can be treated quasi-classically and the tunnel ionization describing ADK-model [ADK86] could be derived.

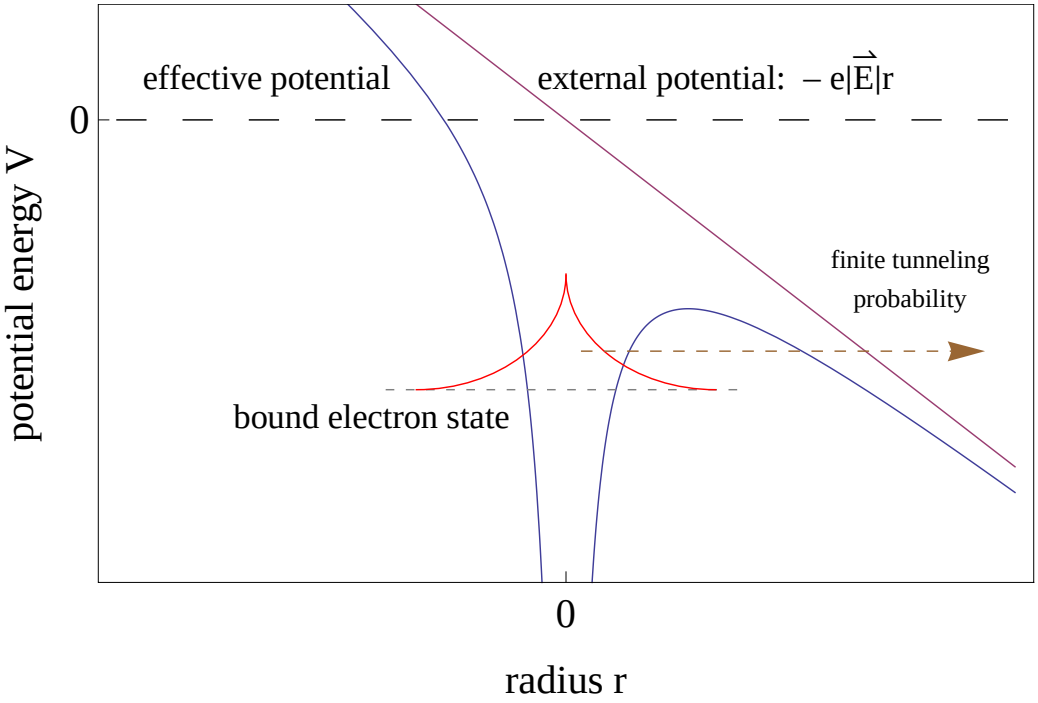

Figure 2.2.: Tunnel ionization is a process in which an atomic bound electron may tunnel through a deformed atomic potential barrier. This mechanism is forbidden in an undisturbed potential due to the infinite Coulomb wall thickness and thus the vanishing probability of presence in the far-field of the atom. But applying a strong electric field will make the thickness and thereby the tunneling probability finite.

For even higher intensities the deformation of the atomic potential through the electric field strength of the approaching light might be so strong that the electron binding potential on one side of the atom is suppressed below the energy of the electron state. Hence, the electron is released leaving an ionized atom. This procedure is reasonably called barrier suppression ionization (BSI). This is a extreme case of the beforehand mentioned tunnel ionization which is lowering the potential barrier below the ionization potential I_P. Although the ADK-model is applicable by

reason of the prior alluded analogy there is a simpler way of description by simple classical electrodynamics. Therefore a superposed electric potential V consisting of the Coulomb potential, for an electron bound to an atom, and a radius-dependent, linearly varying external electric field $\vec{E}$ has to be compiled as drawn in Fig. 2.2:

$$V(r) = -\frac{Ze^2}{4\pi\epsilon_0 r} - e|\vec{E}|r$$

Setting the derivative of this function to zero ends up in a radius r_{max} pointing out the barrier peak. Thus it is possible to estimate the intensity threshold for BSI I_{BSI} by evaluating $V(r_{max}) = I_P$:

$$I_{BSI} \geq \frac{I_P^4 \pi^2 c \epsilon_0^3}{2Z^2 e^6} \approx 4.00 \cdot 10^9 \frac{I_P^4}{Z^2} \,\text{in}\,\text{W}\,\text{cm}^{-2} \text{ with } [I_P] = \text{eV}$$

2.1.2.3. Laser ablation

Laser ablation describes a process of material removal from solids which utilizes lasers, e.g. cutting, drilling or engraving. If the incident energy exceeds the material specific damage threshold ablation begins. Depending on the applied laser pulse length the material removal is characterized by thermal heating and dielectric breakdown or plasma formation due to avalanche and multi-photon ionization. The typical heat diffusion time inside the bulk material is in the picosecond range [BCS11]. Hence, laser pulses with a duration of some picoseconds or shorter, like femto- or attoseconds, are in the following called short or ultrafast whereas pulses longer than several picoseconds are determined as long pulses.

For long pulses the electromagnetic wave respectively the photons transfer their energy to the electrons inside the sample. Therefore generally free unbound electrons have to be available inside the material (e.g. the conduction band inside a crystal), either through its natural structure or due to impurities. Due to the long pulse duration the energy is also transferred from the electrons into the bulk of the target, e.g. via collisions or phonons. Thus the matter is heated, starts to boil and melt. As shown in Fig. 2.3 the melting entails many negative effects. The expansion of the heat affected zone (HAZ) leads to shock waves, which yield micro or even macro cracks within the bulk and riffles at the surface. Due to the ongoing energy input the molten material is ejected and can contaminate the surface. In consequence of the high temperature, the debris is fused to the surface and is therefore just hard to remove. The whole process is not greatly precise by creating a damage larger than the laser beam focus with an additional recast layer.
As a consequence of the connection between pulse length τ and energy transfer the damage threshold depends on the pulse length by $\tau^{1/2}$ [SFH+96b]. This denotes that longer pulses have to contain more energy than shorter ones for ablation because a part of the energy is lost by diffusion into the material causing structural changes but is not used for the machining.

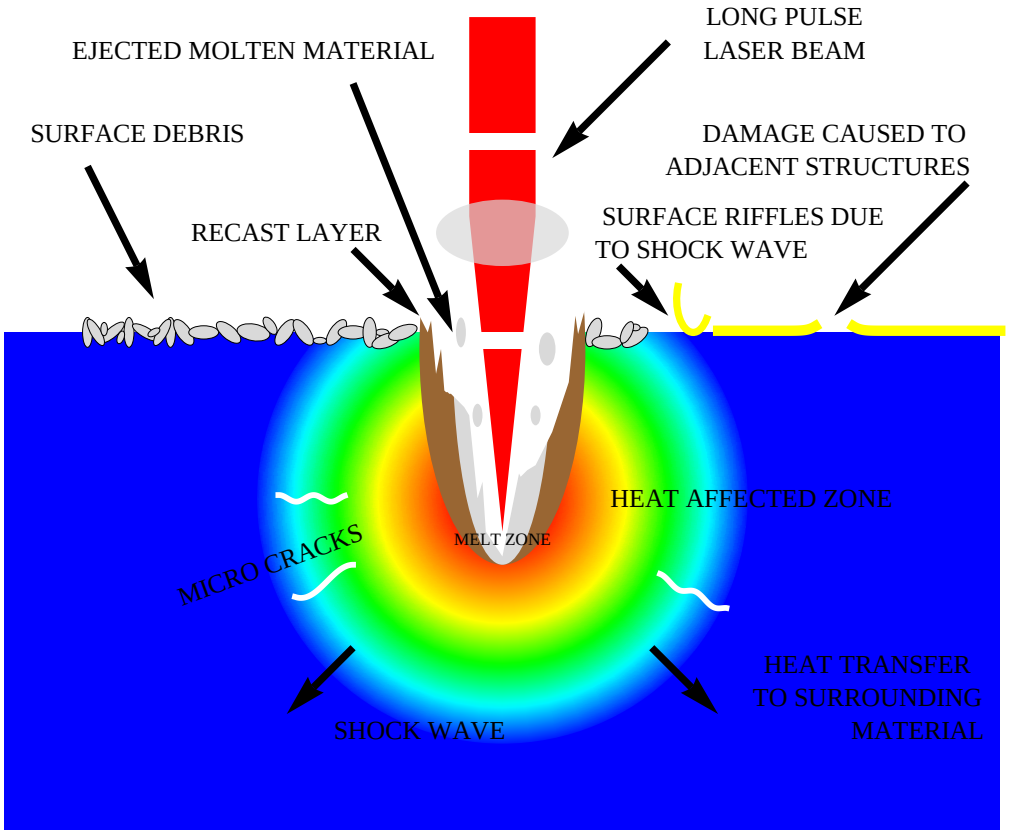

Figure 2.3.: Illustration of long pulse interaction. The long interaction time entails an energy transfer to the bulk material. Adapted from [BCS11].

Short pulses have totally different characteristics. Because of their short duration, they have, compared to longer pulses, higher intensities and the whole energy can be considered to being applied instantaneously. Thus no heating can occur. The ablation happens due to ionization. In contrast to the long pulse case no free electrons are needed in the bulk. They are created anyway by multi-photon ionization. This is why short pulse lasers, compared to long pulses, can readily machine transparent material. The ionization spreads out in an avalanche cascade via oscillations and collisions of electrons and ends up in the formation of a plasma [SFH+96a]. The pressure inside the plasma leads to the so-called Coulomb explosion. The light electrons are ejected first. The charge separation then causes the ions to follow and leave the bulk material. So the energy is carried out of the working volume. Therewith there is no HAZ, no shock waves, no micro cracks and no riffles. Additionally the plasma structure, consisting of charged ions, avoids the creations of debris. The ions are repelling each other due to the Coulomb forces and therefore do not agglutinate so there is no unremovable structure left on the surface as shown in Fig. 2.4. Another positive feature is that the damage size is proportional to the laser beam focus size and can be adjusted by tuning the laser energy. Hence, precise

micromachining is possible even on a scale smaller than the laser beam diameter in the focus. Furthermore, short-laser-pulse ablation implicates a high shot-to-shot repeatability and machining below the surface inside transparent material e.g. by changing the refractive index.

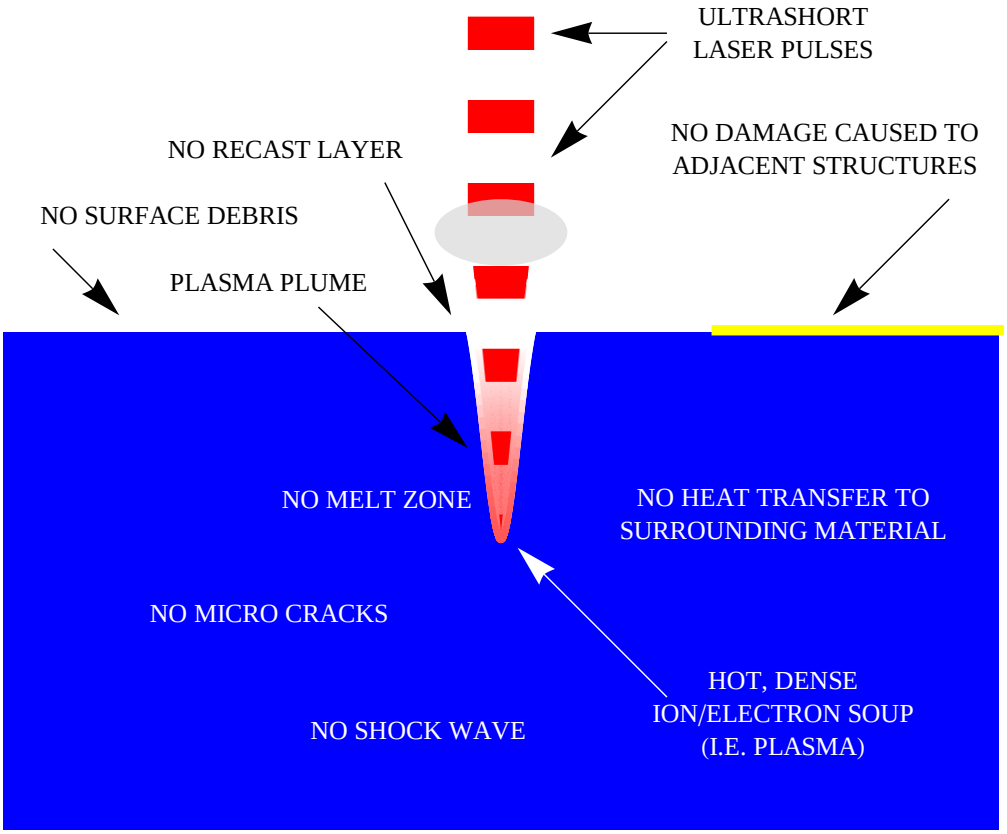

Figure 2.4.: Illustration of short pulse interaction. Adapted from [BCS11].

In conclusion, short laser pulses offer the possibility of precise and reproducible material processing, regardless of the materials melting point and hardness. No material can withstand the forces at work at these power densities. Besides machining, laser ablation is also used in medicine for minimally invasive procedures.

2.1.3. Gaussian beam optics

The propagation of laser beams can be described by Gaussian beam optics. In cylindrical coordinates with longitudinal direction z and transverse distance r the characteristic distributions energy and intensity of a fundamental Gaussian beam are given by:

$$\vec{E}(r,z) = \vec{E}_0 \frac{w_0}{w(z)} e^{-\left(\frac{r}{w(z)}\right)^2} e^{-i|\vec{k}|\frac{r^2}{2R(z)}} e^{i\left(\zeta(z)-|\vec{k}|z\right)} + c.c.$$

$$I(r,z) = I_0 \left(\frac{w_0}{w(z)}\right)^2 e^{-\frac{2r^2}{w^2(z)}}$$

with i the imaginary unit, $\vec{k}$ the wave vector and $I_0 = \frac{2P}{\pi w_0^2}$ the peak intensity which is proportional to the power P as aforementioned and derived by integration. The term describing the electric field is composed of three parts.
The first one is an amplitude factor with a transverse Gaussian distribution. The beam radius w is defined as the distance to the beam axis z where the amplitude or intensity is reduced to $1/e$ or $1/e^2$ respectively. While propagating the intensity distribution retains the shape but the transverse size w changes along the expansion direction z (cf. Fig. 2.5). The minimum spot size w_o is at $z = 0$ what is called the beam waist.

$$w(z) = w_0 \sqrt{1 + \left(\frac{z}{z_R}\right)^2}$$

$$z_R = \frac{\pi w_0^2}{\lambda} \tag{2.14}$$

The Rayleigh range z_R represents the distance after which the beam radius is increased by a factor of $\sqrt{2}$: $w(z = \pm z_R) = \sqrt{2} w_0$ and thus the intensity is halved. In the far field ($z \gg z_R$) w increases linearly with z according to $w(z) \approx w_0 z / z_R$. In this region beam divergence due to diffraction can be defined as

$$\theta = \arctan\left(\lim_{z\to\infty} \frac{w(z)}{z}\right) = \arctan\left(\frac{\lambda}{\pi w_0}\right).$$

The latter both terms of the electric field represent a transverse and a longitudinal phase factor respectively. The transverse phase factor is similar to a spherical wave in paraxial approximation. R is the radius of curvature of the spherical wavefront marking the transverse depending phase shift. Hence, the Gaussian beam can be described with spherical wavefronts for which the radius of curvature is varying along propagation:

$$R(z) = z\left(1 + \left(\frac{z_R}{z}\right)^2\right)$$

This curvature has a minimum at z_R: $R_{min} = R(z = z_R) = 2z_R$. R increases linearly with z for $z \gg z_R$ ending in $\lim_{z\to\infty} R \to \infty$ same as for $z = 0$. This means there is a flat wavefront as for plane waves at the beam waist and at large distances and curved wavefronts as for spherical waves in between due to the non-constant transverse intensity profile.
The longitudinal phase factor includes, in addition to the usual phase kz of plane waves, the Gouy phase $\zeta(z) = \arctan(z/z_R)$. This factor is a longitudinal phase shift slowly varying with z from $-\frac{\pi}{2}$ to $\frac{\pi}{2}$ going from $z \ll -z_R$ to $z \gg z_R$. Descriptively spoken this phase shift symbolizes the wavefront flipping when crossing the

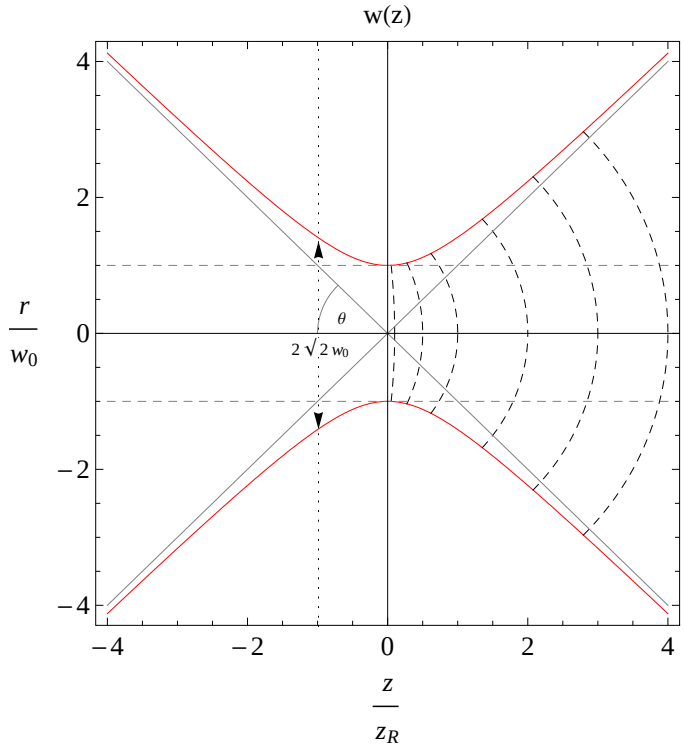

Figure 2.5.: Illustration of Gaussian beam parameters. The red curve illustrates the laser beam, the solid gray lines follow the far-field approximation with divergence θ and the black dashed lines the wavefronts of curvature R. The minimum beam diameter w_0 is increased by a factor $\sqrt{2}$ after one Rayleigh length z_R.

beam waist.
For further information about laser and Gaussian beam optics it is referred to literature e.g. [HLL+07, Sie86, Hec91, BW99].

2.1.4. Time bandwidth product

To reach high power or high energy density for light matter interactions short pulsed lasers are used. Short laser pulses like femtosecond pulses require large bandwidths in their spectral domain. Therefore a plane electro-magnetic wave with a temporal Gaussian shape and a central frequency ω_0 is considered which can be described mathematically by:

$$\begin{aligned} \vec{E}(t) &= \vec{E}_0 e^{-at^2} e^{i(\omega_0 t + \phi(t))} \qquad \text{with} \quad \phi(t) = bt^2 + \mathcal{O}(t^3) \\ &= \vec{E}_0 e^{-(a-ib)t^2} e^{i\omega_0 t} \end{aligned} \tag{2.15}$$

and thus leading to a temporal intensity profile of:

$$I(t) \propto \left|\vec{E}(t)\right|^2 \propto e^{-2at^2}$$

$2a$ is the inverse, squared $1/e^2$ pulse length in the intensity profile and relates to the full width at half maximum (FWHM) pulse duration $\triangle\tau = (2\ln 2/a)^{1/2}$. The size b declares the quadratic phase; higher orders are neglected.
The imaginary part of (2.15) displays the total phase ϕ_{tot} of the electric field. Hence, the time derivative yields an expression for the instantaneous frequency

$$\omega_i(t) = \frac{d\phi_{tot}}{dt} = \omega_0 + 2bt\,.$$

The quadratic phase term in time domain corresponds to a linear time dependance of the instantaneous frequency of the pulse, thus characterizing a linear chirp. By applying a Fourier transform to $E(t)$ the frequency spectrum is obtained:

$$\begin{aligned}\tilde{E}(\omega) &= \tfrac{1}{\sqrt{2\pi}}\int_{-\infty}^{\infty} E_0 e^{-(a-ib)t^2+i\omega_0 t} e^{-i\omega t} dt \\ &= \tfrac{E_0}{\sqrt{2(a-ib)}} e^{-\frac{(\omega-\omega_0)^2}{4(a-ib)}}\end{aligned}$$

Hence the spectral intensity is:

$$\tilde{I}(\omega) \propto \left|\tilde{E}(\omega)\right|^2 \propto e^{-\frac{1}{2}\frac{a}{a^2+b^2}(\omega-\omega_0)^2} \propto e^{-4\ln 2\left(\frac{\omega-\omega_0}{\triangle\omega}\right)^2}$$

In analogy to $\triangle\tau$, $\triangle\omega$ represents the FWHM spectral range. Then the FWHM frequency is:

$$\triangle\nu = \frac{\triangle\omega}{2\pi} = \frac{\sqrt{2\ln 2}}{\pi}\sqrt{a\left[1+\left(\frac{b}{a}\right)^2\right]}$$

The presence of a chirp leads to an increasing spectral bandwidth for a given pulse duration. Correspondingly, a chirp yields an elongation of the temporal pulse profile for a fixed spectral bandwidth. This relation is described by time-bandwidth-product (TBP) as a measure of phase distortions. For Gaussian pulse shapes it takes the form:

$$\triangle\tau\,\triangle\nu = \frac{2\ln 2}{\pi}\sqrt{1+\left(\frac{b}{a}\right)^2} \approx 0.441\sqrt{1+\left(\frac{b}{a}\right)^2}$$

The TBP for Gaussian pulses has a minimum at $\triangle\tau\triangle\nu \to 0.441$ for $b \to 0$. If this is the case the pulse is called transform limited, meaning all spectral components are in the same phase thus resulting in the shortest possible temporal pulse length for a given spectral shape. For achieving a laser pulse with Gaussian shape of about 30 fs FWHM duration a minimum FWHM bandwidth in the spectral range of $\sim 31.4\,\mathrm{nm}$ around a central wavelength of 800 nm is required, which is the typical wavelength of high power titanium:sapphire (Ti:Sa) laser systems (calculated by the relation: $\triangle\nu = c\,\triangle\lambda/\lambda^2$). The TBP is comparable to Heisenberg's uncertainty principle. By applying root mean square (RMS) values instead of FWHM his equation is fulfilled: $\triangle\omega_{RMS}\,\triangle t_{RMS} \geq 1/2$. The previously covered TBP refers to Gaussian pulse distributions. Other commonly used temporal pulse profiles and their TBP are listed in Tab. 2.1.

Table 2.1.: Full width at half maximum (FWHM) time-bandwidth-products (TBPs) and pulse durations for selected commonly used temporal laser pulse envelopes. Θ is the Heaviside step function. Numbers taken from [Dre10]

Field envelope	Intensity profile in time t	Intensity profile in frequency ω	Min. TBP (FWHM)	Duration $\triangle\tau$ (FWHM)
Gaussian	$\propto \exp\left[-2\left(\frac{t}{\tau_{Ga}}\right)^2\right]$	$\propto \exp\left[-\frac{1}{2}\left(\tau_{Ga}\omega\right)^2\right]$	0.441	$1.177\tau_{Ga}$
Lorentzian	$\propto \left[1+\left(\frac{t}{\tau_{Lo}}\right)^2\right]^{-2}$	$\propto \exp\left[-2\tau_{Lo}\left\|\omega\right\|\right]$	0.142	$1.287\tau_{Lo}$
Hyperbolic secant	$\propto \mathrm{sech}^2\left(\frac{t}{\tau_{Sec}}\right)$	$\propto \mathrm{sech}^2\left(\frac{\pi}{2}\tau_{Sec}\omega\right)$	0.315	$1.763\tau_{Sec}$
Rectangular	$\propto \Theta\left(\frac{\tau_{Rec}}{2}-\left\|t\right\|\right)$	$\propto \mathrm{sinc}^2\left(\tau_{Rec}\omega\right)$	0.443	τ_{Rec}

2.1.5. Chirped Pulse Amplification (CPA)

Conventional laser oscillators typically synthesize pulses within the energy range of up to nJ or μJ. To reach higher energies an amplification is needed during which two significant issues must be overcome. First, interactions during amplification might lead to a reduction in beam quality. Second, the intensity of an amplified pulse may cross the damage threshold of the reflective and transmissive optics used thus destroying the laser components. Therefore the amplifying medium has to fulfill several requirements. The bandwidth of the amplifier has to be large enough to cover the whole spectrum of the seed pulse, the fluence of the pulse must be near the saturation fluence of the medium $F_S = h\nu/\sigma$, with σ the stimulated emission cross section, and finally the intensity inside the amplifier has to stay below a critical level. Otherwise nonlinear effects become significant leading to distortion of the spatial and temporal pulse profile, e.g. by self-phase modulation (SPM) or self-focusing and filamentation. With rising intensities the intensity dependence of the refractive index η becomes important. In the lowest order approximation it can be written as:

$$\eta = \eta_0 + \eta_2 I$$

Here η_0 is the commonly used refractive index as in the linear low intensity case and η_2 is a material constant specifying the linear intensity relation. For some typical values of η_0 and η_2 see Tab. 2.2. To avoid beam distortions and protect the laser optics the negative effects can be estimated using the B-integral:

$$B = \frac{2\pi}{\lambda}\int \frac{\triangle\eta}{\eta}\,dl = \frac{2\pi}{\lambda}\int_0^L \eta_2 I\left(z\right)\,dz$$

This contains the line-integrated nonlinear index of refraction along the laser beam path of length L. It represents the accumulated phase delay experienced by the

Table 2.2.: Selection of the refractive index η_0 and the intensity dependent part η_2 of materials often implemented in laser beamlines. Wavelength validations are specified in the quoted reference.

Material	η_0	$\eta_2 \left(\mathrm{W^{-1}cm^2}\right)$	Data origin
Sapphire	1.8	$2.9 \cdot 10^{-16}$	[Web95]
Fused silica	1.47	$3.2 \cdot 10^{-16}$	[Web95]
BK-7	1.52	$3.4 \cdot 10^{-16}$	[Web95]
Air	1.0003	$5.0 \cdot 10^{-19}$	[PHH89]
Vacuum	1.0	$1.0 \cdot 10^{-34}$	[EK35]

high intensity beam owing to η_2 at any position across the beam and is normalized to the laser wavelength λ. The critical intensity, above which nonlinear effects must be considered or become problematic, belongs to a B-integral value of about 1. Higher values result in the preferentially amplification of high spatial frequencies which must then be removed by spatial filtering. Hence, the maximum intensity to which a laser pulse can be directly amplified inside an active amplifier medium is on the order of 10 $\mathrm{GWcm^{-2}}$ ([MSB+88]).

The reduction of nonlinear effects by decreasing the intensity during the amplification process to solve the prior explained challenges can be achieved by either enlarging the laser beam diameter or by increasing the pulse duration. The former approach is no feasible solution. The reason is twofold. On the one hand, a larger beam would require bigger optics throughout the hole laser setup which in turn would be much more expensive and thus economically unfavorable. On the other hand, much more important is the fact that the energy extraction efficiency of a laser beam inside an excited gain material in the amplifier depends on the energy fluence. As mentioned at the beginning of this paragraph this has to be in the order of the saturation fluence of the medium F_s thus being relatively high and contradicting intensity reduction by spatial size increase. In the end it is just possible to boost a laser pulse in energy beyond the energy flux density threshold by expanding its temporal profile.

There was a similar complicacy in radar which was compensated by stretching the pulses. This concept was transposed to the optical range by introducing the chirped pulse amplification (CPA) technique ([SM85]). Through temporal stretching, subsequent amplification and reliable recompression laser pulses with TW to PW peak powers are available (Fig. 2.6). In CPA a light pulse is sent through a dispersive element most common a grating structure. This introduces positive group delay dispersion (GDD) and chirps the pulse positively, meaning higher frequencies travel longer distances than lower ones, and therefore the pulse gets stretched by a factor usually on the order of 10^3 to 10^5. During the temporal stretching the different frequency components are spatially sorted and guided along different paths inside the stretching device (for example an arrangement of gratings) resulting in different runlines and GDD. This can be characterized by a stretcher specific frequency

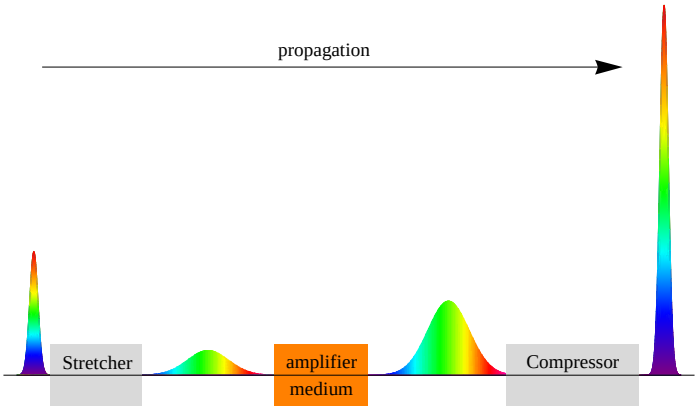

Figure 2.6.: The concept of chirped pulse amplification (CPA). A short laser pulse is stretched in time to reduce the intensity in the subsequent amplification process due to dispersion of the broad bandwidth by temporal frequency separation. This chirp is afterwards reversed by passing through a matched compressor. CPA allows the synthesis of fs pulses with PW peak power.

dependent phase shift:

$$\phi(\omega) = \phi_0 + \phi_1(\omega - \omega_0) + \phi_2(\omega - \omega_0)^2 + \phi_3(\omega - \omega_0)^3 + \ldots \quad \text{with} \quad \phi_n = \frac{1}{n!}\frac{d^n\phi}{d\omega^n}\bigg|_{\omega_0}$$

ϕ_0 is a frequency independent shift of the carrier envelope phase and ϕ_1 is the time delay of the whole laser pulse. Non of these, neither ϕ_0 nor ϕ_1, contribute to the pulse duration stretching unlike phase orders of $n \geq 2$. The whole function $\phi(\omega)$ with all its terms depends on the stretcher setup and thus is quite complex. That is the reason why it is important to match the compressor, which is needed for the creation of high peak powers after amplification, to the stretcher such that the stretcher-induced phase ϕ_{str} is compensated for as much as possible by the phase shift, mainly an inverse down-chirp, generated by the compressor ϕ_{comp}. All orders of $\phi(\omega)$ could be compensated for, if there were no more dispersive material in the beamline. In reality the transmissive and reflective optical components, and even air, introduce additional dispersion and thus a phase ϕ_{mat}. Hence, the relation $\phi_{str} + \phi_{comp} + \phi_{mat} \approx 0$ has to be fulfilled. Besides using gratings for CPA and introducing positive and negative dispersion there is also the possibility to apply prisms although grating structures have a much higher expansion-compression ratio. In the beginnings, fibers have also been used for pulse stretching.

2.2. Plasma

2.2.1. Definition of plasma

Plasma ($\pi\lambda\alpha\sigma\mu\alpha$, gr.: formation, structure) may be regarded as an additional state of matter to the commonly known: solid, liquid and gas. Generally it can be described as material consisting of ionized matter, showing a collective behaviour and if watched from the outside seems to be neutral. For a proper and accurate definition ionized matter must fulfill the following conditions to be considered a plasma [Ost11]:

- Spatial quasi-neutrality. The Debye screening length λ_D has to be small compared to the physical dimensions of the plasma volume and the studied processes.
- Temporal quasi-neutrality. The plasma frequency ω_P has to be large compared to a characteristic frequency describing the time scale of the process such that charges are rapidly shielded.
- Ideal plasma conditions. Inside an ideal plasma binary particle collisions must be dominated by collective electrostatic interactions. Hence the relation $\Lambda \gg 1$ has to be valid (cf. (2.16)).

2.2.2. Debye length

On length scales larger than the Debye length λ_D plasmas appear electrically neutral because different charged particles shield each other [GR98]:

$$\lambda_D = \sqrt{\frac{\epsilon_0 k_B}{e^2}\left(\frac{n_e}{T_e} + \sum_{ion\ sorts}\frac{Z_i n_i}{T_i}\right)^{-1}}$$

k_B is the Boltzmann's constant, n_e and T_e are the electron density and temperature, respectively. Similarly n_i and T_i relate to the ion species whose charge state is given by Z_i.
The Debye length is coupled to another important characteristic measure, the plasma parameter:

$$\Lambda = \frac{4\pi}{3} n_x \lambda_D^3 \propto n_x^{-1/2} \tag{2.16}$$

It represents the number of particles of a species x and density n_x placed in a sphere of radius λ_D [Fit06]. It has to distinguished between two cases. If $\Lambda \ll 1$, the plasma is called strongly coupled. Thereby the volume enclosed by the Debye sphere is sparsely filled. The kinetics of the charged particles is dominated by single scattering due to particle collision. Electrostatic interaction is shielded and

does not contribute. This situation is cold and dense and cannot be considered as a plasma due to the lack of collective behaviour. In contrast to that, hot and dilute real plasmas are described by $\Lambda \gg 1$. The Debye sphere is racily populated what causes the domination of electrostatic collective interaction over individual scattering. Hence, this regime is called weakly coupled.

2.2.3. Plasma frequency

Owing to the acting electric effects inside the Debye sphere, a small displacement $\delta\vec{x}$ of a slice of electrons against the ion plasma background will result in a restoring force $\vec{F}_r = -q_{dis}\vec{E}_r = -m_{dis}\ddot{\delta\vec{x}}$ with $q_{dis} = -en_eA_{dis}|\delta\vec{x}|$ and $m_{dis} = m_en_eA_{dis}|\delta\vec{x}|$ the displaced charge and mass, respectively. A_{dis} stands for the area of the slice displaced by $\delta\vec{x}$ and therefore the product of both forms the containing volume. The electric field strength $|\vec{E}_r| = \sigma/\epsilon_0$ calculated using Gauss' Law, with $\sigma = -en_e\delta\vec{x}$ the surface charge density. This yields the differential equation:

$$\frac{d^2}{dt}|\delta\vec{x}| + \frac{e^2n_e}{m_e\epsilon_0}|\delta\vec{x}| = 0$$

This equation of motion describes a harmonic oscillator with the frequency:

$$\omega_p := \omega_{p,e} = \sqrt{\frac{e^2n_e}{m_e\epsilon_0}} \tag{2.17}$$

The electron plasma frequency $\omega_{p,e}$ is the basic angular oscillation frequency defining the time scale τ_e for the collective electron effects inside a plasma. It is also called the plasma or Langmuir frequency ω_p. For the ions of the plasma background with mass m_i the time scale τ_i can be derived in a analogous way: $\omega_{p,i} = Z_ie\left(n_i^{-1}m_i\epsilon_0\right)^{-1/2}$. Since the ion mass is much higher and therefore their reaction time is much slower compared to the electrons, the ion motion is negligible and the plasma frequency will refer to the electron motion as indicated in (2.17). This is true for plasma acceleration but not in the case of laser ablation due to the longer time scale. In addition the Debye length can be rewritten disregarding the ion terms due to the just mentioned explanation.
At least the dispersion relation of a plasma wave is given by using the plasma or Langmuir wave vector $\vec{k}_L$ (Bohm-Gross-dispersion-relation [BG49]):

$$\omega_L^2 = \omega_p^2 + \frac{3k_BT_e}{m_e}|\vec{k}_L|^2 \tag{2.18}$$

2.3. Plasma wakefield acceleration (PWA)

2.3.1. Principles of PWA

Plasma wakefield acceleration requires a plasma. This is usually created by ionization of a gas, e.g. via a high voltage discharge or laser pulse. Typical gas species are hydrogen or helium since they are simply available , relative cheap and easy to ionize. A relativistic driver pulse entering the plasma will then excite a plasma wave. The ponderomotive force of the driver expels the plasma electrons in both the transverse and longitudinal directions. After the driver has passed by, a positively charged region is left behind due to the presence of the plasma ion background. As a result of their relatively high rest mass the ion motion can be neglected and they can be assumed to be static. That is the reason why they stay at their position and do not take part in the interaction. The transverse deflected electrons are then attracted by this positive charge and oscillate back around their original position due to the resulting Coulomb field. This yields an electron density modulation with a density peak behind the pulse-following, ion dominated low density area. Hence, the wave characterized by the plasma electron density modulation is created. This is called the wakefield. It is analogous to a ship sailing across the sea entailing waves in its back. The plasma wave follows the driving pulse with a phase velocity determined by the laser pulse group velocity. The wakefield induces a longitudinal charge separation on the axis of propagation between the electron density spikes and the background ions. The resulting Coulomb force can be used for acceleration. The reachable electrical field strength is depending on the density amplitude n_0 [ESKT96]:[1]

$$\left|\vec{E}_0\right| = cm_e\omega_p e^{-1} \simeq 0.96 n_0^{1/2} \quad \text{in V/cm with } [n_0] = \text{cm}^{-3}$$

Taking into account all electrons participating in the plasma wave and densities of about 10^{18}cm^{-3} field gradients in the GeV/cm are conceivable. These gradients are several orders of magnitude higher than for conventional radio frequency (RF) accelerators. Well injected electrons may ride on the plasma wave and be accelerated to relativistic energies in the direction of laser propagation. Depending on the nature of the driving pulse, either a pulse from a laser or a particle beam, this procedure is called particle-driven wakefield acceleration (PWFA) or laser-driven wakefield acceleration (LWFA). The normalized electron density of a plasma wave for LWFA is shown in Fig. 2.7.

Since the proposal of wakefield acceleration in 1979 [TD79] lasers have gone through a development in power output. Nowadays, sufficient intensities are reached required by the laser wakefield acceleration. LWFA is most efficient using short laser pulse,

[1] In general the electric field additionally depends on the intensity $\left|\vec{E}_z\right| = \left|\vec{E}_0\right| \frac{a_0^2}{\sqrt{1+a_0^2}}$. For simplicity just $\left|\vec{E}_0\right|$ was evaluated.

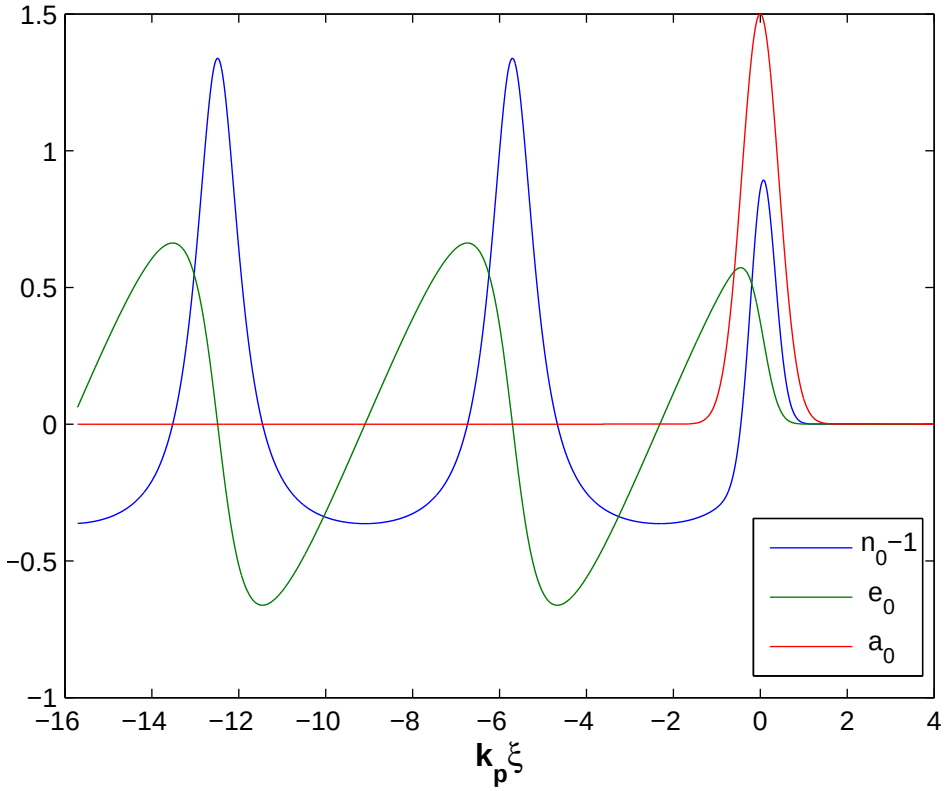

Figure 2.7.: Simulated plasma wave showing the normalized plasma-electron density modulation $n_0 - 1$ (blue) created by a pulse of $a_0 = 1.5$ (red). Additionally, the resulting normalized electric field $e_0 = \left|\vec{E}_z\right| / \left|\vec{E}_0\right|$ is displayed in green. The first density peak on the right, which is a bit smaller than the others, indicates the electrons which are directly pushed by the wakefield driving pulse. Electrons can be accelerated after injection into the buckets in between the density peaks.

i.e. those for which the plasma wave length $\lambda_p = 2\pi c/\omega_p$ is longer than the laser pulse length $c\tau$, with τ the pulse duration: $\lambda_p < c\tau$. If a large number of electrons acquire a velocity close to the phase velocity of the plasma wave, wave-breaking occurs. The electrons are injected into the wakefield and accelerated. This can be pictured as electrons surfing the wake of the plasma wave. If the laser pulse length is longer than the plasma wave length $c\tau < \lambda_p$ a self-modulation instability develops. The front of the laser pulse starts to drive a plasma wave. The created electron density modulation of the plasma wave δn_e results in a periodic change of the refractive index [Ost11]:[2]

$$\eta \approx 1 - \frac{1}{2}\left(\frac{\omega_p}{\omega}\right)^2 \left(1 + \frac{\delta n_e}{n_e} + ...\right) \tag{2.19}$$

[2]With the phase velocity $v_\phi = \omega|\vec{k}|^{-1}$ and the dispersion relation $\omega^2 = \omega_p^2 + c^2|\vec{k}|^2$ (cf. (2.18)) a general expression for the refractive index is: $\eta = c/v_\phi = \sqrt{1 - (\frac{\omega_p}{\omega})^2}$.

The modulation of the refractive index acts back on the trailing position of the laser pulse. It breaks up into a train of shorter pulses which are individually shorter than the plasma wavelength and can resonantly drive a plasma wave. This is called self-modulated laser wakefield acceleration (SM-LWFA). Although this procedure is less efficient high energy electrons beam might still be generated [MND+95, ESKT96, HLL+07].

2.3.2. Injection schemes

For PWA first of all electrons have to be injected into the wakefield. The ostensibly simplest way might be self-injection. This happens via wave-braking [BNPS98, TGG+03, TMK97, EHHT98]. However, this process is a statistical, highly nonlinear one which cannot be well controlled and thus varies with each laser shot. This prevents the achievement of the desired stable and reproducible system. To reliably generate high quality electron bunches from a PWA based accelerator, controlled particle injection is essential. This can for example be done by external injection [KLI+06]. Thereby a pre-accelerated electron bunch from a conventional accelerator is injected into the correct phase of the wakefield. Such a bunch can be fully characterized and therefore measurements of the bunch properties after PWA can determine the effect of the process. All its qualities are known due to accompanied diagnostics and should be maintained while the energy is increased by the plasma wave. However, this requires a conventional accelerator. Additionally, attention has to be paid to the injected pulse length. In general it has to be small compared to the plasma wavelength λ_p which is typically in the μm range and thus requires ultrashort electron-bunch durations with femtosecond accuracy in the injection. It is an ambitious venture and needs cutting-edge synchronization. There is also the possibility of controlled internal injection. This can be realized by three injection schemes: colliding pulse injection, ionization injection or density down-ramp injection.

2.3.2.1. Colliding pulse injection

The technique of injection by colliding pulses was proposed by [EHL+97]. For this purpose three laser beams are recommended. The first laser, further indicated by subscript 0, provides the ordinary driver pulse whereas the other two laser pulses account for the injection. One of them (indexed with 1) follows the driving pump pulse with a well defined temporal offset determining the position e.g. the phase of injection while the other one is sent from the the opposite direction to counter propagate (index 2). This is illustrated in Fig. 2.8. The normalized intensity, the wave number and the angular frequency are denoted by a_i, k_i and ω_i with $i = 0, 1, 2$ referring to the different pulses. The relations concerning wave vector and frequency are: $k_0 \simeq k_1 \simeq -k_2$ respectively $\omega_1 - \omega_2 = \triangle\, \omega \gg \omega_p$. The wave-driving pulse is polarized perpendicular to the others to avoid interaction between them. The driver and thus the plasma wave, the pursuer and the counter pulse

move with a velocity near the speed of light v_g, $v_p \simeq c$. As soon as the injection pulses collide some distance behind the driver pulse the intensity raises up and a so-called ponderomotive beat wave is generated (cf. (2.12)) which is described by $a_1 a_2 \cos(\triangle kz - \triangle \omega t)$ with the phase velocity $v_{p,b} \cong |\triangle \omega| / \triangle k \ll c$ and $\triangle k = k_1 - k_2 = 2k_0$. The resulting axial force responsible for injection and trapping of the electrons is then:

$$F_z = -\frac{m_e c^2}{\gamma} \frac{\partial}{\partial z} a_1 a_2 \cos(2k_0 z - \triangle \omega t) \sim \frac{m_e c^2}{\gamma} 2k_0 a_1 a_2$$

A two-stage acceleration process can occur during the overlapping time of the injection pulses. The slow beat wave heats and traps plasma background electrons. These can be injected in the fast wakefield and accelerated as a result of their shift in momentum and phase.
Concluding, the concept of colliding pulses offers the possibility of precise injection control. The temporal offset of the co-propagating pulses controls the injection phase as aforementioned whereas the backward propagating pulse duration corresponds to the duration of the injection process and thus the number of injected electrons. The beat wave phase velocity and the injection energy are controlled via $\triangle \omega$ and the pulse amplitudes respectively. Among others, the procedure of colliding pulses for controlled injection has been used by [FRN+06].

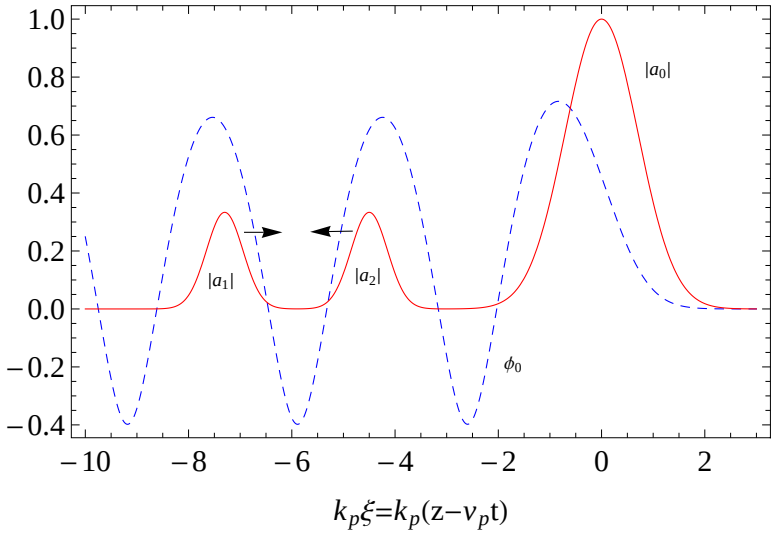

Figure 2.8.: Colliding pulses injection scheme. Plasma wave indicated by the electric potential ϕ_0 (dashed blue curve) and the profiles of the driving laser pulse $|a_0|$ with the two injection pulses $|a_1|$ in forward and $|a_2|$ in backward direction (solid red curve). Everything is stationary in the $k_p\xi = k_p(z - v_p t)$ frame besides the counter propagating laser pulse $|a_2|$.

2.3.2.2. Ionization injection

The concept of ionization injection [ODK+07] necessitates two different gas species. The first one is used to create the background plasma and the wave whereas the second is employed for the electron injection. The latter must have at least an ionization state separation with a large gap $\triangle I = I_i - I_{i-1}$ to the next highest state where I_i indicates the ionization potential for the state i. The LWFA driving pulses have typical intensities in the $10^{18}\,\mathrm{W\,cm^{-2}}$ range. Therewith a pulse has sufficient intensity for first gas ionization even at more than a five σ pulse width ($I \sim 10^{12}\,\mathrm{W\,cm^{-2}}$), σ being the rms pulse width. This means the plasma is created by the wings of a pulse long before the intensity increases and the wakefield is triggered. For the injection the intensity has to surmount the ionization energy of the afore introduced second gas highly separated ($\triangle I$) special electron state. This has to be achieved close to the peak intensity of the pulse or as a result of additional focusing of the laser beam. The density modulation of the wakefield entails a change in the refractive index (cf. (2.19)) and self-focusing of the laser beam can occur. After all, the intensity in the focus should be just high enough to generate new free electrons which can be captured and accelerated in the plasma wave. This is due to the ponderomotive force. At the focus the intensity profile is approximately constant so the ponderomotive force, which is proportional to the intensity gradient (cf. (2.12)), is weak (Fig. 2.9) and the electrons can be injected into the wave. The injection phase is therefore controlled by the position of the beam focus and the electron quantity by the gas mixture.

2.3.2.3. Density down-ramp injection

As seen in the previous sections the plasma (electron) density is an important, permanently occurring measure affecting the most important parameters of PWA. Additionally, it can be utilized for particle injection via density down-ramp [BNPS98, FESL06] as demonstrated by Geddes and co-workers [GCME+08, GNP+08]. Fig. 2.10 shows an exemplary density profile for down-ramp injection in PWA.
A plasma density decrease on a length scale L_{tr} much longer than the plasma wavelength λ_p could be used for local self-trapping of electrons in the plasma wave. Therefore, consider the initial electron phase before the density transition to be $\phi_i = k_p \xi_i = k_p N_p \lambda_{p,i}$ which is located N_p plasma periods behind the driver beam at the co-moving coordinate $\xi = z - v_p t$. The phase after the transition has changed to $\phi_f = k_p \xi_f = k_p N_p \lambda_{p,f}$. The subscripts i and f stand for the initial and final status before and after the density transition. Due to the down-ramp, the density is decreased $n_i > n_f$ and the plasma wavelength is increased $\lambda_{p,i} < \lambda_{p,f}$ (cf. (2.17)). Hence, the density transition changes the position (phase) by the relative amount of $\triangle \xi = N_p \left(\lambda_{p,i} - \lambda_{p,f}\right)$. Over the transition distance of length L_{tr} the change in the phase velocity is then $\triangle v_p/c \simeq N_p \left(\lambda_{p,i} - \lambda_{p,f}\right)/L_{tr}$ which increases proportional to N_p, the distance behind the driver pulse, as well as the magnitude of the density

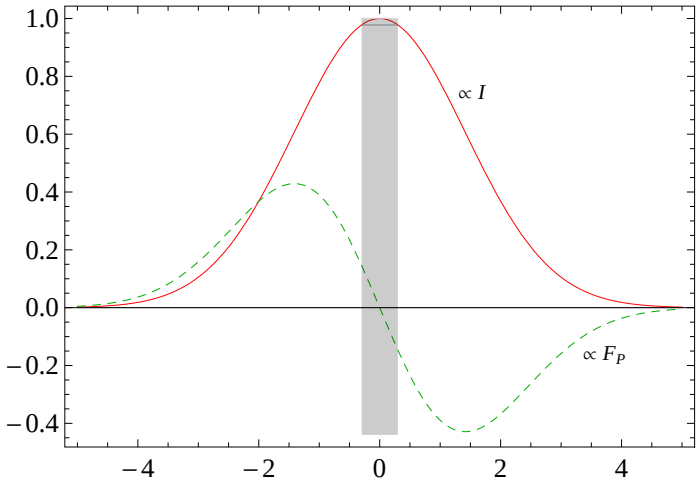

Figure 2.9.: Illustration for the understanding of ionization injection. The solid red curve showing a Gaussian shaped pulse and depicts the intensity distribution I. Its derivative is shown in dashed green and represents the strength of the ponderomotive force F_P. Lasers for LWFA usually allocate much higher Intensities than needed for gas ionization. Hence, the front wing of the pulse lead to ionization followed by wakefield creation with rising intensity. A second gas species chosen with much higher ionization threshold will be ionized at higher intensities where F_P got back to minor values. Thus generated electrons are not expelled and get injected into the wakefield, marked by the gray shaded area. The topic of ionization injection is still a actual field of research [CES+12].

gradient $(\lambda_{p,i} - \lambda_{p,f})/L_{tr} \simeq d\lambda_p/dz = -(\lambda_p/2n)\, dn/dz$.
In general the phase velocity is derived from the phase $\phi = k_p(z) - ct$ by

$$v_p/c = \frac{1}{c}\frac{\omega_{p,eff}}{k_{p,eff}} = \frac{1}{c}\frac{\frac{\partial\phi}{\partial t}}{\frac{\partial\phi}{\partial z}} = \left(1 + \frac{\xi}{k_p}\frac{dk_p}{dz}\right)^{-1}$$

For small variation this leads to:

$$\frac{v_p}{c} - 1 \simeq -\frac{\xi}{k_p}\frac{dk_p}{dz} = \frac{\xi}{\lambda_p}\frac{d\lambda_p}{dz} = -\frac{\xi}{2n}\frac{dn}{dz} \tag{2.20}$$

Since everything occurs behind the driving pulse ($\xi < 0$) the velocity will decrease for decreasing density gradients $dn/dz < 0$. The electrons will be injected and trapped approximately when their velocity equals the plasma wave phase velocity $v_p = v_e$.
The trapping process can also be visualized in phase space (Fig. 2.11). Free and trapped trajectories are separated by the so-called separatrix which also indicates the plasma wavelength. By changing the density the separatrix is varied. A decrease in density and thus an enlargement of the wavelength results in electron injection. Free electrons which have been outside the separatrix find themselves enclosed within the separatrix after its increase in volume.

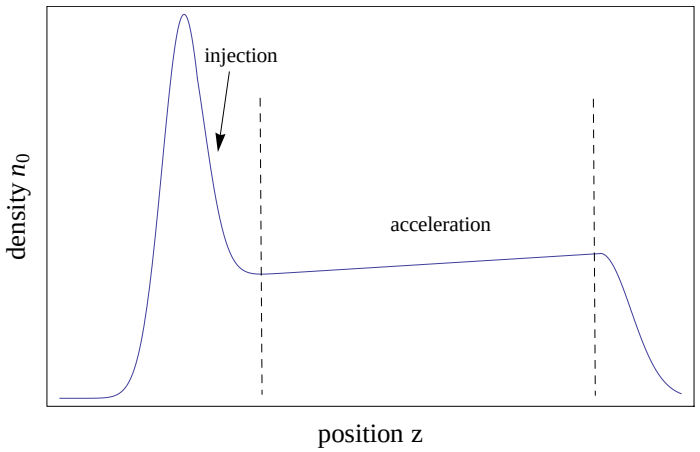

Figure 2.10.: Plasma density outline for density down-ramp injection and subsequent acceleration.

2.3.3. Limits of laser wakefield acceleration

Laser-induced plasma-based wakefield acceleration is limited by three basic mechanisms which terminate the acceleration process - the three D's: laser-energy depletion, electron dephasing and laser diffraction.

2.3.3.1. Depletion

A laser pulse continuously transfers its energy to the plasma while exciting and driving the plasma wave. The distance over which this is occurring and after which the energy is depleted is called laser energy or pump depletion length L_{pd} [TES90, BIK+92, TBB94]. This length can be derived through a comparison of the energy stored inside the wakefield along L_{pd} and the energy contained inside an electromagnetic field of length $L_L = \lambda_p/2$ representing the driver pulse: $\left|\vec{E}_z\right|^2 L_{pd} \simeq \left|\vec{E}_L\right|^2 L_L$. $\left|\vec{E}_z\right|$ denotes the longitudinal electric field strength (cf. p.20 footnote 1) and $\left|\vec{E}_L\right|$ the electric field of the laser pulse. With $a_0 < 1$ the depletion length L_{pd} can then be estimated using:

$$L_{pd} \simeq L_L \frac{\left|\vec{E}_L\right|^2}{\left|\vec{E}_z\right|^2} = \frac{\lambda_p}{2} \frac{\frac{I(a_o)}{\epsilon_0 c}}{\left(\frac{cm_e\omega_p}{e}\frac{a_0^2}{\sqrt{1+a_0^2}}\right)^2} = \frac{1}{2}\frac{\lambda_p^3}{\lambda^2}\frac{1+a_0^2}{a_0^2} \overset{a_0\lesssim 1}{\approx} \frac{\lambda_p^3}{\lambda^2}\frac{1}{2a_0^2} \propto n_e^{-3/2}$$

A bit more general expression is given by [ESKT96]:

$$L_{pd} \simeq \left(\frac{\omega}{\omega_\mathrm{p}}\right)^2 \lambda_p \cdot \begin{cases} a_0^{-2} & \text{for } a_0 \lesssim 1 \\ a_0(3\pi)^{-1} & \text{for } a_0 \gg 1 \end{cases}$$

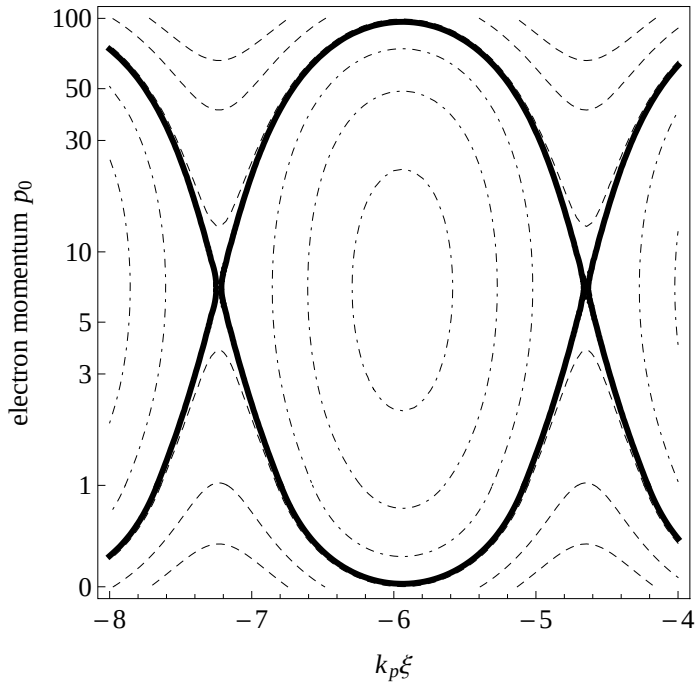

Figure 2.11.: Plasma electron phase space showing the separatrix (thick, solid line) which separates the free or open (dashed lines) and the closed electron trajectories (dot-dashed lines).

For laser amplitudes $a_0 \lesssim 1$ the potential energy and thus the wakefield-energy-coupling grows with a_0^2 so that L_{pd} decreases. For the other case $a_0 \gg 1$ the opposite holds true. The coupling decreases with $a_0 \to \infty$ since then $\left|\vec{E}_z\right| \propto a_0$ and $L_L \propto a_0$ [TES90]. Although this is simply a one dimensional approach the depletion length can be estimated for a typical parameter set of LWFA ($n_e = 7 \cdot 10^{18}\text{cm}^{-3}$, $a_0 = 0.9$ and $\lambda = 800$ nm) by $L_{pd} = 3.9$ mm.

2.3.3.2. Dephasing

After injection and acceleration the electrons travel with a velocity approaching c. The laser and thus the wakefield propagates with a velocity less than c due to traversing a medium, the plasma. The electrons slowly start to overtake the wave, outrunning the accelerating phase and entering decelerating field regions. Therefore the electron dephasing is an inherent effect of LWFA. The longest distance over which electrons can travel in phase inside the wake and thus can be accelerated is called the dephasing length L_d [LSE+96, VEL99]. For $a_0 \lesssim 1$ this distance can be estimated by:

$$\triangle v \frac{L_d}{c} = \frac{\lambda_p}{4} \qquad \Rightarrow \qquad L_d = \frac{\lambda_p^3}{2\lambda^2} \propto n_e^{-3/2}$$

with the velocity difference $\triangle v = c - v_g$. A more rigorous expression is given by [ESL09]:

$$L_d \lesssim \frac{\lambda_p^3}{2\lambda^2} \cdot \begin{cases} 1 & \text{for } a_0 \lesssim 1 \\ \frac{\sqrt{2}a_0}{\pi N_p} & \text{for } a_0 \gg 1 \end{cases}$$

N_p is again the number of plasma periods behind the driver. As for the depletion case the distance increases with decreasing density $L_d \propto n_e^{-3/2}$. To avoid dephasing, a slight density up-ramp along the acceleration path would match the electron velocity to the plasma wave phase velocity [RSE+10] (cf. (2.20)). This is in some case an inverted effect of down-ramp injection and is also indicated in Fig. 2.10. For the parameter set given above, the dephasing length evaluates to $L_d = 1.6$ mm. This is quite similar to the corresponding depletion length.

2.3.3.3. Diffraction

As depicted on page 11 lasers can be described by Gaussian beam optics and therefore laser diffraction occurs. In order to accelerate to high energies a long acceleration distance is desirable. This implies that the laser pulse has to maintain an intensity sufficiently high for driving the wake over the whole acceleration length. That is technically only feasible for distances on the millimeter to centimeter scale. If the acceleration length exceeds the achievable confocal laser parameter $b = 2z_R$ the laser pulse needs to be confined and guided e.g. via self-guiding or by preformed plasma density gradient channels. Without any guiding the diffraction length $L_{diff} = b$ limits the acceleration process to the millimeter range which is comparable to the other two mentioned circumstances and usually it is even shorter.

2.3.3.4. Maximum electron energy gain

The maximum energy gain W_e of an electron inside the plasma wave can be estimated considering all the above listed limits. Longitudinal and transverse plasma channel shaping compensates for dephasing and diffraction, respectively. The pump depletion cannot be counterbalanced thus being the crucial factor. Hence, the final energy is:

$$W_e = eE_z L_{pd} = m_e \omega_p v_p L_{pd} \propto \frac{1}{n_e}$$

For the parameter set given above and approximating $v_p \simeq c$ this yields a maximum electron energy $W_e \approx 990$ MeV over an acceleration distance of $L_{pd} \approx 3.9$ mm.

This reveals the general problem for high energy acceleration machines. Even if L_{pd} is enlarged by minimizing the plasma density the distance is to short to cross the TeV level. A possibility of overcoming this problem is the concept of staged acceleration

in which several single LWFA based accelerators subsequently accelerate the same electron bunch. Such an arrangement is technically demanding and has not been demonstrated yet.

For a further introduction and a general overview on LWFA it is referred to [ESL09].

The latter two of the three terminating D's, dephasing and diffraction, can be compensated by the application of capillaries; only depletion cannot. Gas or plasma filled capillaries can be compared to commonly known fiber waveguides counteracting laser diffraction. Specially designed gas targets, e.g. capillaries with inlets, offer the possibility of plasma density gradient structuring. Therewith capillaries can be applied to avoid dephasing. Additionally, the injection schemes such as density down-ramp or ionization injection can be used. Hence, this thesis is about the design, the machining and the characterization of capillaries for LWFA.

3. Simulation

As a first step of the gas target manufacturing process special attention has to be paid to the design. As introduced in the previous chapter the plasma density is a important parameter for the control of electron acceleration in PWA. The design should take this circumstance into account to allow for the generation of features such as a smooth density increase along the acceleration distance for dephasing prevention or a density peak at the beginning of the target for down-ramp injection. Besides these theory-based prerequisites, practical limitations must also be kept in mind; examples are the producibility, the laser parameters or the in- and outlet distances and spacings for the gas supply.

If a suitable target geometry is found, the plasma particle distribution and evolution in the target can be evaluated by the application of Computational Fluid Dynamics (CFD) simulations. To obtain reasonable results with CFD simulations the underlying dynamics and the numerical methods should be known and understood. The first is necessary to choose the correct basic equations and boundary conditions, which describe the investigated problem, the latter for the correct choice of discretization schemes, the underlying mesh, and for the interpolation of the results. The motion of fluids is represented by the Navier-Stokes equation which in most cases has no analytical solution. That is why numerical methods are required. Therefore the partial differential equations are applied onto a mesh for discretization and approximated by a system of computer solvable algebraic equations. The solution is returned at discrete points in time and space. Hence, the resulting accuracy depends on the quality of the mesh structure. A more rigorous introduction to CFD can be found within [FP08].

The simulations are performed using the free, open source CFD software package called OpenFOAM (Open Field Operation and Manipulation) [Ope11]. It is a flexible and efficient C++ based toolbox and includes numerous pre-configured solvers, pre- and post-processing utilities and libraries to solve a lot of different kinds of CFD problems. Since it is open source, it is free to access and additionally offers complete freedom to customize and extend the functionality, e.g. by special problem solver and model development which are not included in commercial CFD codes. Thus it is utilized by a large user community in science and research, offering the finite volume method and providing native support for parallel computing.

The first and simplest gas target design is illustrated in Fig. 3.1. It consists of a capillary and two inlets as gas feeds. The design can be expanded to add further in- and outlets for creating special, desirable density profiles as required for the

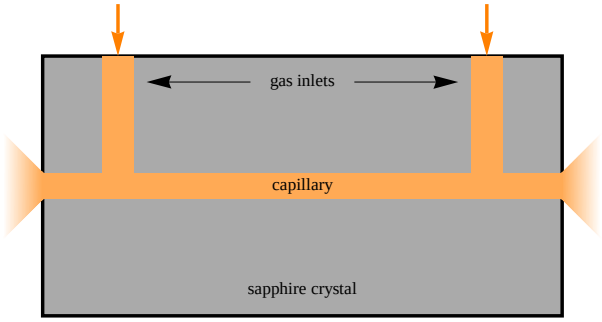

Figure 3.1.: Simple gas target design consisting of a capillary and two inlets for gas filling.

previously alluded injection. Each of the inlets has a width of 600 μm, a depth of 400 μm and a length of 10 mm and is displaced by 2 mm with respect to the edge of the crystals. The distance between the inlets is halved from originally 27.8 mm to 13.9 mm for faster simulation without changing the physics. Therewith the capillary length is analogously reduced from 33 mm to 19.1 mm. The diameter of the cylindrical capillary is 250 μm. It is placed in the middle of the crystal with its center distanced by 10 mm from the top edge. These are typical dimensions for such a gas target.

Fig. 3.2 shows the results of a 2D and a 3D simulation, in blue and purple respectively, of this hydrogen filled gas target for the density ρ, the pressure p, the velocity v and the temperature T. The 2D case stands for a two dimensional mesh with an additional cell in the third dimension whereas the 3D case implies a completely three dimensional structured mesh. The applied pressure at the gas inlets was 200 hPa. Pressure and density were additionally converted to particle density using the ideal gas equation. The few ticks along the z-axis indicate the positions of the capillary characteristic features: The inlets (marked via dashed lines), the total capillary length and the total observed length including the enclosing vacuum. It can be ascertained that the measures between the gas inlets, which is the important part for the acceleration process, do not significantly differ in the 2D and 3D case. Minor and major differences can be observed outside the capillary and at its ends especially for the velocity and the temperature. However, these regions are not important for PWA and thus the discrepancy between 2D and 3D simulation is negligible and therefore the faster 2D simulations seem to be sufficient.
The simulations were running until steady-state conditions were reached; meaning the velocity in the important middle part of the capillary was approximately zero and constant. For the 200 hPa input pressure the simulated steady state parameters in this region were: $\rho = 15.0\,\mathrm{g/m^2}$, $p = 186\,\mathrm{hPa}$, $n = 45.0 \cdot 10^{23}\,\mathrm{m^{-3}}$, $T = 300\,\mathrm{K}$.

In order to be applied in LWFA with ultra-high-power laser beams and high voltage discharges, the gas containing target has to be manufactured from a robust material.

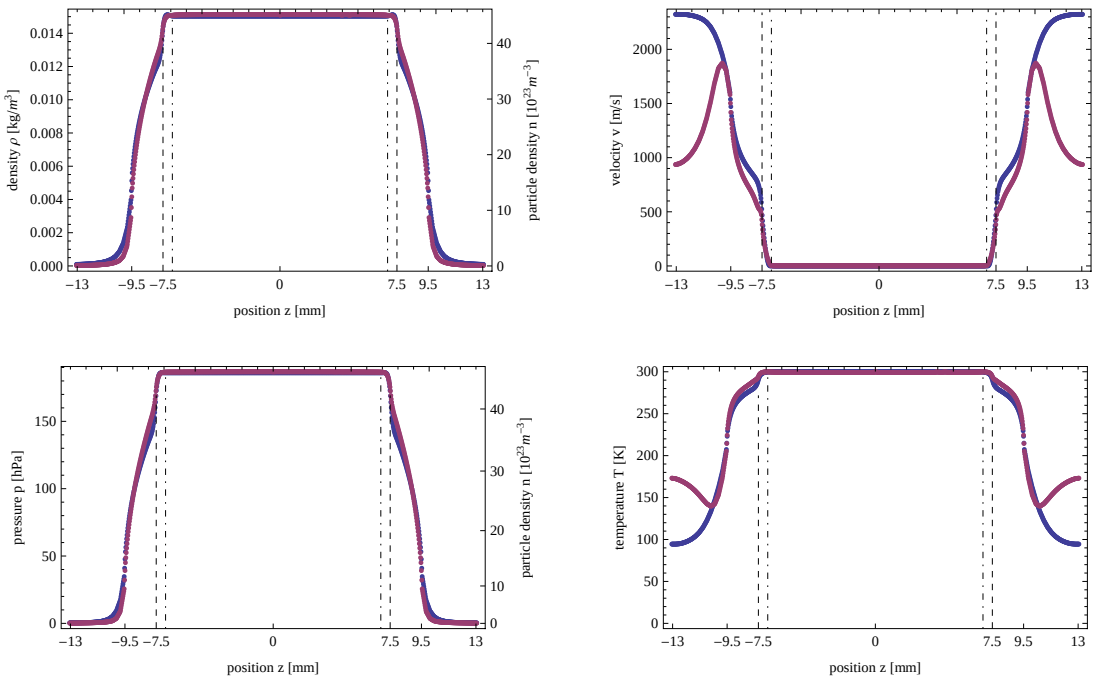

Figure 3.2.: Simulation results along the middle of a simple round capillary gas target (cf. Fig. 3.1). On the left it is shown the density ρ (top) and the pressure p (bottom) respectively the particle density n of H_2 molecules. On the right the velocity v (top) and the temperature T (bottom) can be seen. The simulation was done in 2D (blue) and 3D (purple) for comparison. The 2D case stands for a two dimensional mesh with an additional cell in the third dimension whereas the 3D case implies a completely three dimensional structured mesh. As it can be seen, the difference at the important part inside the capillary bordered by the inlets (marked by the dashed lines) is negligible. Major deviation just occur for v and T and there especially in the vacuum part outside of the capillary.

The hardest material available is diamond. However, it is quite expensive and thus not economically viable. For this reason sapphire was chosen for longevity. It is the next hardest choice and much cheaper. The usage of such hard and robust materials demands a great deal of the fabrication process. The only material which can be employed for cutting or drilling is the expensive diamond. Other processing schemes include water jet milling or of course laser ablation machining, as introduced in the former chapter. This will be the main topic of the next chapters.

4. The Setup

4.1. Laser system

The laser system used in the gas target manufacturing process is build from commercial titanium doped sapphire lasers [Mou86], consisting of an oscillator and a regenerative chirped pulse amplifier.

The oscillator is the Micra-5 Titanium:Sapphire Oscillator provided by Coherent Inc.[1] It provides pulses with a full-width at half maximum (FWHM) duration of $\tau \simeq 30.5\,\mathrm{fs}$ [Wun12] and a repetition rate of $f_{rep} = 81.25\,\mathrm{MHz}$ at a central wavelength of $\lambda = 797 \pm 5\,\mathrm{nm}$ with a FWHM bandwidth of $\triangle\lambda = 47 \pm 5\,\mathrm{nm}$. The pulsing is achieved by passive mode-locking via Kerr-lensing and prism dispersion compensation for pulse compression [SKS91]. It is pumped by a VERDI, a frequency doubled [FHPW61] continuous wave (cw) Nd:YVO_4 laser at $\lambda = 532\,\mathrm{nm}$, with a power of $P_{pump} = 5\,\mathrm{W}$ yielding a output power of $P_{seed} = 493 \pm 92\,\mathrm{mW}$. The oscillator layout is pictured in Fig. 4.1.

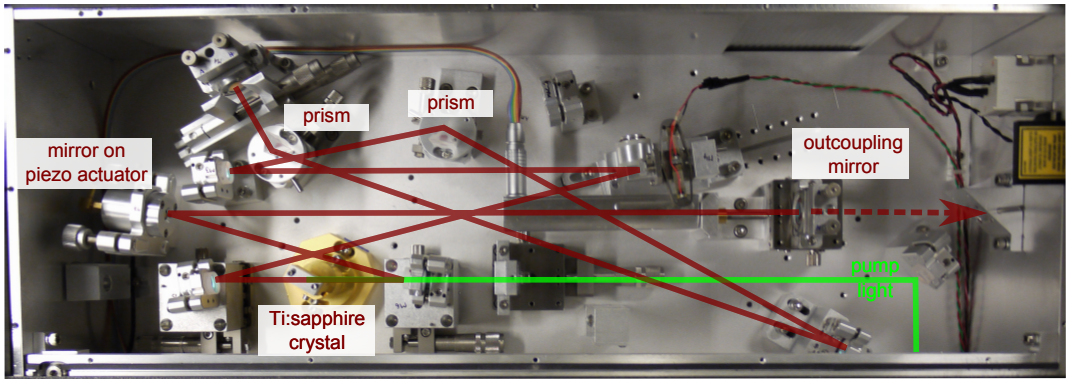

Figure 4.1.: Cavity layout of the Micra oscillator. (By courtesy of S. Wunderlich [Wun12].)

The amplifier seeded by this oscillator is the Spitfire Pro XP Ultrafast Ti:Sapphire Amplifier from Spectra-Physics.[2] The system contains an incoupling beam line, a stretcher, the regenerative amplifier and a compressor. The incoupling includes two iris apertures and an optical diode with a Faraday rotator (FI), which rotates

[1] http://www.coherent.com/downloads/Micra_DS_Final.pdf
[2] http://www.newport.com/images/webdocuments-en/images/11815.pdf

the polarization, to avoid back-reflected seed pulses damaging the oscillator. The stretcher, same as the compressor, is a four time passed single grating device with an additional diode based bandwidth detector (BWD) protecting the system from damage by pulses of narrow bandwidth or even a cw mode. After stretching, one pulse from the seed train is picked by the first Pockels cell (PC1) and inserted into the cavity containing Ti:Sa crystal. The crystal is pumped from both sides by an EMPOWER, an intracavity frequency-doubled and acousto-optic Q-switched [MH62, JZK06] Nd:YLF laser at $\lambda = 527\,\mathrm{nm}$ ($\tau_{pulse} \sim 100 - 300\,\mathrm{ns}$, $f_{rep} = 1\,\mathrm{kHz}$), with a power of $P_{pump} \sim 20\,\mathrm{W}$. A second intracavity Pockels cell (PC2) determines the number of round trips for maximum amplification and releases the amplified pulse before the energy starts to be restored by the crystal. At one end of the cavity a photodiode is attached to observe the amplification process through the leakage of the end mirror. After amplification the beam diameter is increased by a telescope mirror arrangement. Pulses after the final compression have a duration of $\tau \lesssim 35\,\mathrm{fs}$ with a repetition rate of $f_{rep} = 1\,\mathrm{kHz}$. Output powers of $P_{out} \simeq 3\,\mathrm{W}$ can be reached. Admittedly, this is much more power than required for the machining. Hence, the power is reduced to $P_{out} \simeq 0.2\,\mathrm{W}$ by a tunable attenuator consisting of a $\lambda/2$-plate and a polarizer, which are adjustable with respect to each other. This yields enough power for a subsequent finer power adjustment at the machining device and decreases the risk of laser related injury during the beam transport across the optical table. However, the pulse energy is still increased by more than four orders of magnitude during the amplification. The e^{-2} beam diameter of an approximated spatial Gaussian pulse profile was measured to be $d \sim 8\,\mathrm{mm}$. The layout and beam paths are illustrated in Fig. 4.2.

4.2. Machining device

After amplification the beam is transferred through an aperture and by two lenses and a periscope across the optical table to the machining device. The layout is shown in Fig. 4.3. All included parts (coatings) are matched to the laser radiation. The pulsed laser beam is coupled into the setup via two mirrors and sent through two iris apertures, which are separated by 50 cm. These are used for alignment. In the space between of them several neutral density (ND) filters are placed in addition to an adjustable attenuator, again consisting of a $\lambda/2$-plate and a turnable polarizer. Thereby the power is reduced to $P \sim 30\,\mathrm{mW}$, which was found to be a favourable working point (cf. chapter 6). After the alignment, the beforehand $D \sim 8\,\mathrm{mm}$ beam is focused by a $f = 100\,\mathrm{mm}$ plan-convex lens down to a measured focal radius of $w_0 = d/2 \simeq 10\,\mu\mathrm{m}$. This can also be calculated by [Sie86]:

$$d \approx \frac{2f\lambda}{D}$$

The Rayleigh length for focused 800 nm radiation is therefore $z_R = 390\,\mu\mathrm{m}$ (confer (2.14)). There are two justifactions for this choice of the focal length. On one hand

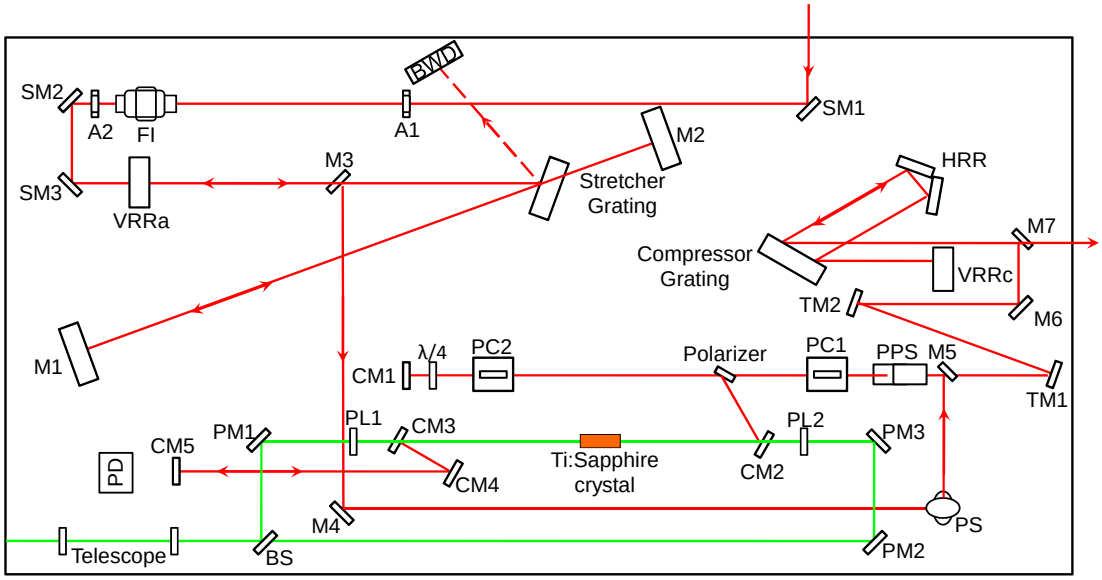

Figure 4.2.: Layout of the Spitfire Pro XP Ultrafast Regenerative Amplifier. Modification of [Spe08]. (Legend: A: Aperture, FI: Faraday Insulator, SM,M,CM,TM,PM: Mirrors, VRR,HRR: Vertical, Horizontal Roof Reflector, (P)PS: (Polarization)Periscope, PC: Pockels Cell, PD: Photo Diode, BWD: Band Width Detector, BS: Beam Splitter)

a focus diameter and thus a focal length as small as possible is preferable for high accuracy machining, on the other hand it cannot be chosen too small taking into account the dimensions of all used assembly parts. After the lens a subsequent beam splitter, placed under 45° with respect to the beam propagation axis, divides the beam onto two paths, a reflected and a transmitted one. The reflected part is imaged by a charged coupled device (CCD) camera (Basler Ace acA1300-30gm) with a microscope objective and is used to observe the shape and the size of the focal spot. The transmitted part focuses onto the sapphire crystal. It is placed inside a self-made, special designed capillary mount (cf. drawings in the appendix) and attached to a commercial, computer-controlled three-axis-stage, which is built from the LTM 60 stepper motors provided by OWIS GmbH. Via the rear side of the beam splitter the surface reflection is captured and imaged by a pair of achromatic lenses and displayed onto a second CCD with a microscope objective. Therewith in addition to the focal spot the crystal surface can also be observed.

For the initial alignment and the calibration of the focus measurement an additional CCD took the place of the capillary stage and watched the focus. The laser beam was guided through the center of all three iris apertures and viewed by this CCD. The mirrors were readjusted until the laser spot place on the CCD no longer changed by opening and dimming of the pinholes one after the other. At this point the setup was finely aligned and the reflected focus could also be observed by the aforementioned

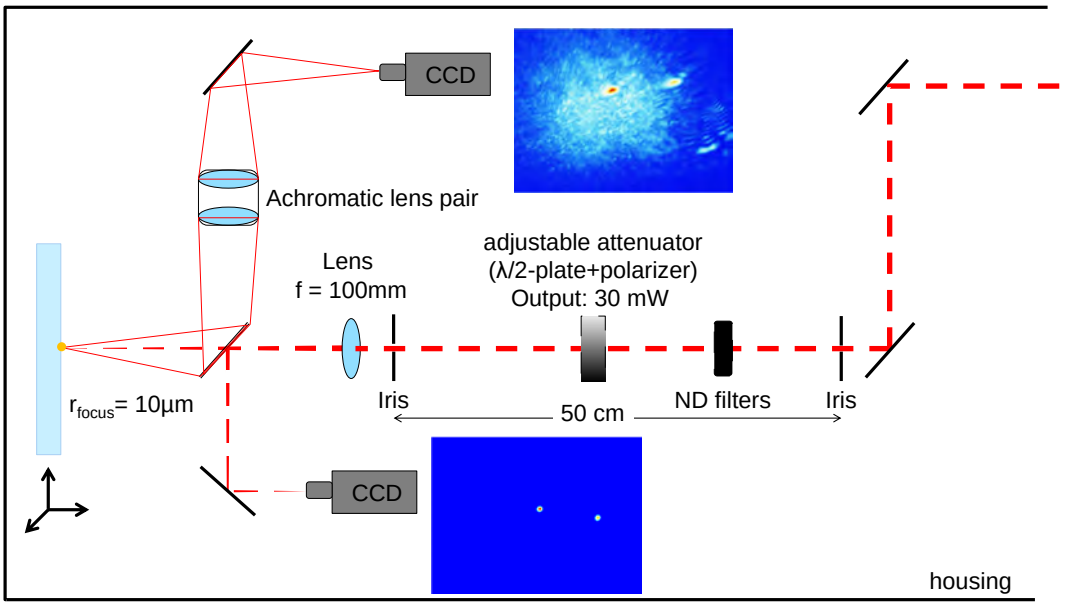

Figure 4.3.: Layout for the fs-micromachining setup with example images captured by each CCD. A picture of the setup can additionally be found in the appendix (*p.* 72).

corresponding CCD. If required, the alignment procedure can be repeated with that default camera later on.

To calibrate the CCD camera the focusing lens was removed to protect the United States Air Force resolution target (USAF-RT) which was placed in the former focal plane. A picture of the USAF-RT taken by the added CCD is shown in Fig. 4.4. The line spacings are provided with the target. After taking a picture, the USAF-RT was removed and the lens was set back to its position. The accurate orientation can be checked by the back reflection. If the backward laser focus is located in the center of the incoming laser beam, the lens is placed at the correct position. This may be determined using a lens tissue.
Then a picture of the reflected focus and a picture via the added CCD had to be taken. Both should be the same. By evaluating the spacings of the shaded regions of the USAF-RT picture, the ratio of μm/pixel could be estimated and, therefore, the focal spot size imaged with this camera. Since they are the same, the reflected focal spot has to be of the same size. Hence, the ratio of μm/pixel for corresponding main camera can be calculated and so later on taken pictures of the focus can be evaluated. The transformation factor was found to be: ~ 0.5 μm/pixel.
Finally, the additional CCD camera is again replaced by the capillary stage.

After the construction of the machining device an astigmatism was observed with the crystal surface imaging CCD, which was not recognized before. A scan of the sapphire crystal through the original focal plane is shown in Fig. 4.5. As can be seen,

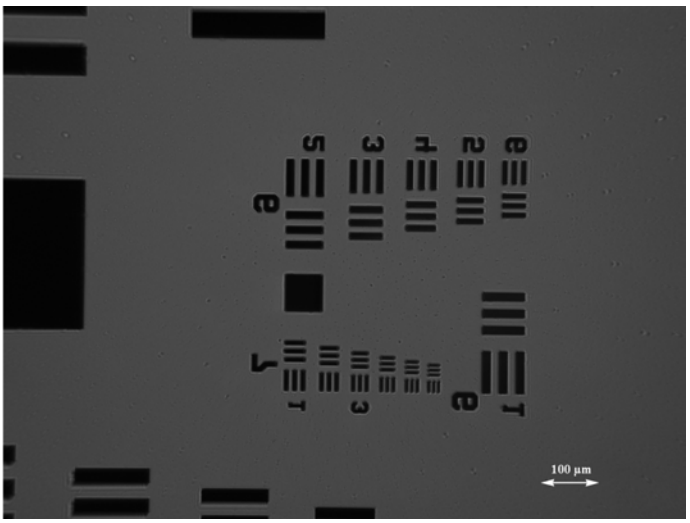

Figure 4.4.: Imaged USAF-resolution target.

the focus varies during the scan from a horizontal line over a cross to a vertical line. This is a typical symptom for astigmatism which might be explained by focusing through an angled, thick plate. Different colors or wavelengths respectively frequencies may also be focused at different distances. At that time the beam splitter was 5 mm thick with a small wedge of 0.5°. This might have introduced a pulse front tilt additionally enhancing the astigmatism. It was replaced with an ultrathin window of 200 μm thickness. The surface reflection after the exchange can be seen in Fig. 4.6. It is a double focus due to a reflection from both the front and the back surfaces of the ultrathin beam splitter. This double focus is seen at all points further down the optical line and thus also by the reflected focus camera.

Last but not least, the Strehl ratio was calculated. To achieve this, all pixel resolved intensity values of an imaged focus are summed with respect to their distance from the intensity maximum and weighted by the total sum; or in other words the intensity distribution of an imaged focal spot is integrated and normalized. This is the Encircled Energy Fraction (EEF) (Fig. 4.7). The Strehl ratio results from the comparison of the real EEF value at a distance equal to the diffraction limitation radius ($r_{dl} = 1.22 \cdot \lambda \cdot f/D$) [HLL$^+$07] and the theoretically perfect imaging, diffraction limited EEF value. Hence, the Strehl ratio is $S \simeq 0.53$. Using the following term, the root-mean square deviation of the wavefront σ and thus the optical quality of the setup can be checked [Alp11]:

$$S \equiv e^{-\left(\frac{2\pi\sigma}{\lambda}\right)^2}$$

The wavefront deviation was estimated to be $\sigma \simeq 0.10\,\mu$m. This is on the order of the beam distortion commonly observed when using mirrors with surface flatness of $\lambda/10$.

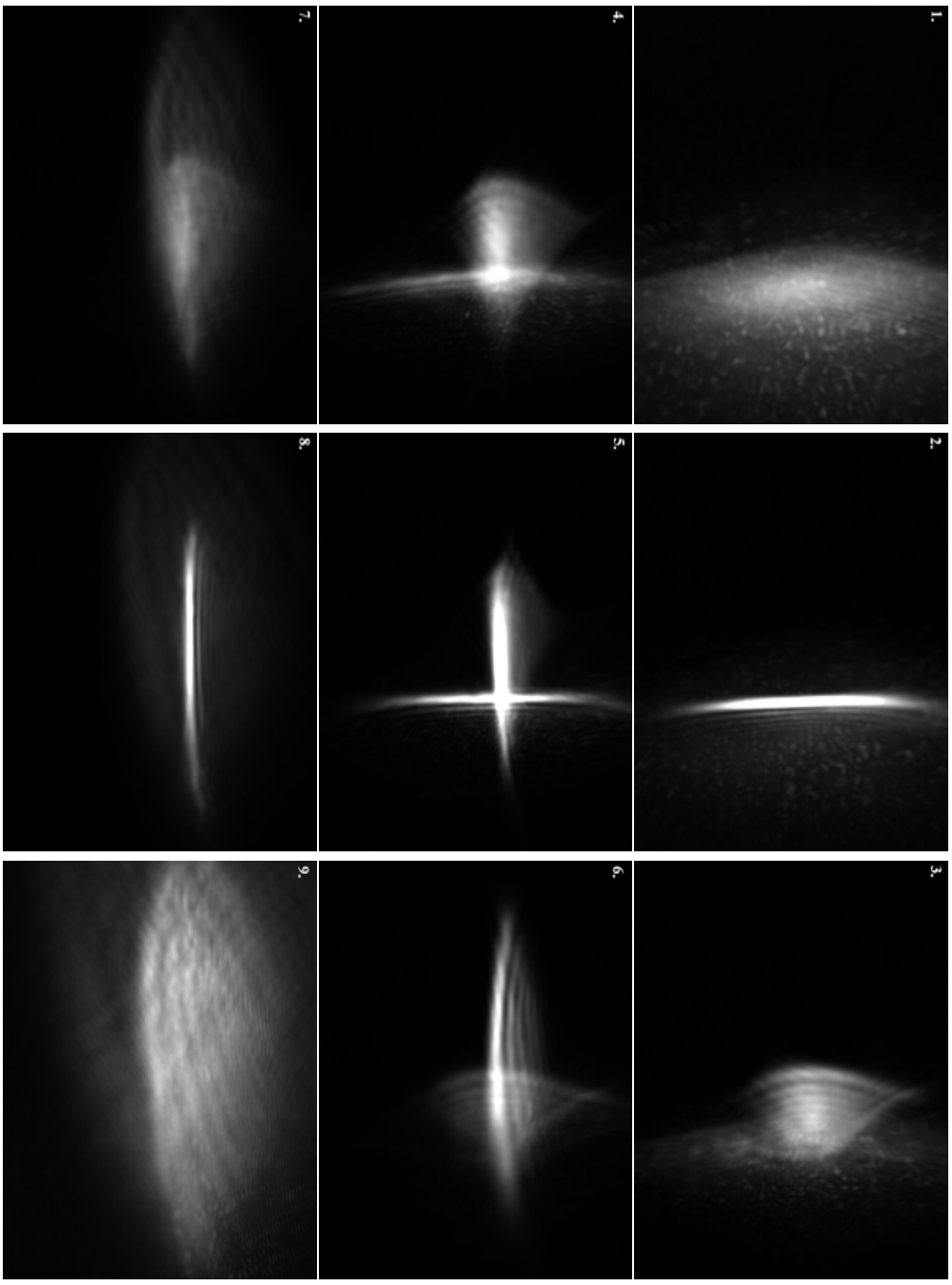

Figure 4.5.: Focus scan of a sapphire plate. The surface imaging CCD camera shows an astigmatism.

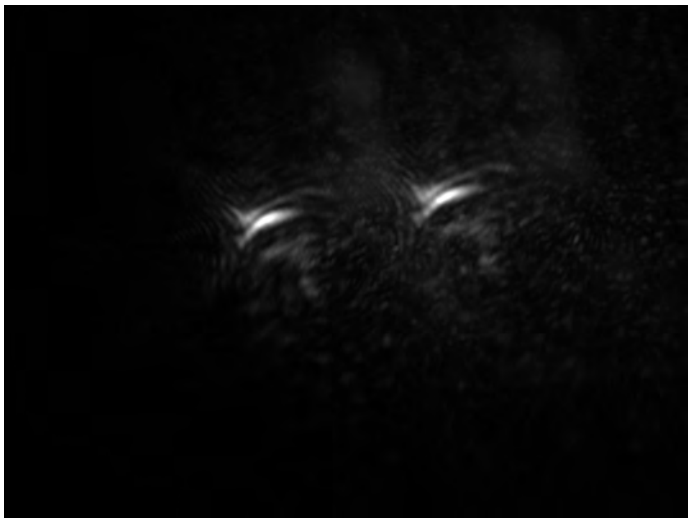

Figure 4.6.: Image of the sapphire crystal surface after beam splitter exchange. Now a double focus is seen from the front and the back of the ultrathin beam splitting window.

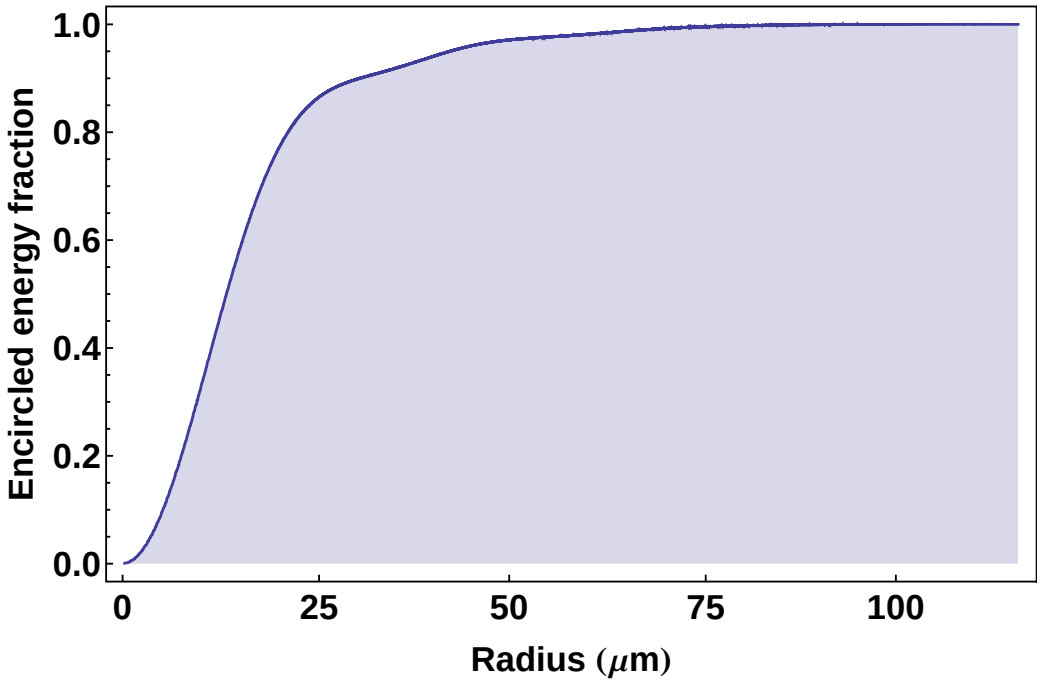

Figure 4.7.: Encircled Energy Fraction (EEF) of the laser focus against the radial distance from the focal center.

5. Safety considerations

The application of high power lasers always necessitates special attention particularly with regard to safety. The powerful laser radiation may injure the eyes or even the skin via thermal heating. As a result of being a class 4 laser system, the scattered radiation is also dangerous. The wavelength of 800 nm is hazardous for the retina since it penetrates the cornea, the lens and the vitreous, even though it is hard to see. To avoid eye damaging, those within the laser room always have to wear goggles if the system is running. Additionally, the whole setup is covered by a black housing to provide an engineered protection solution and therefore reduce the potential risk of the machining device.

Besides these typical laser-based hazards, the mechanism of ablation entails the possibility of additional health risks. Thøgersen et al. [TBH$^+$01] investigated the "X-ray emission from femtosecond laser micromachining" of metals with laser parameters quite similar to those employed here. Typically, X-rays are created at intensities of $10^{12} - 10^{17}\mathrm{W/cm^2}$. They observed X-rays of several keV. The constructed, current setup provides peak intensities of $\sim 10^{14}$ W/cm^2. The creation of X-ray was checked using an dosimeter for pulsed radiation measurements called Babyline. The testing for pulsed radiation showed no explicit signal of more than the natural surrounding background noise. Neither a change of the viewing angle nor the motion of the crystal stage changed this. Although there were no x-rays measured, the housing would provide additional protection.

Another hazardous effect of short-pulse laser machining is the potential production of nanoparticles. Barcikowski et al. [BWH$^+$09] measured the size and distribution of nanoparticles produced during the processing of brass, steel and zirconia with similar laser parameters used for this work. The typical particle size is on the order of nanometers as indicated by its name. Nanoparticles are known to cause adverse health effects [GM07]. Thereby the particles cover the lung tissue so that the respiration becomes difficult and mortality of tarnished people is increased. However, the generation of nanoparticles cannot be avoided during laser ablation. Therefore, the housing offers the best protection against their inhalation. During the machining, the fumes are captured within the housing and in some regions deposits can be seen (Fig. 5.1). After the machining the housing has to be opened to gather the probe. Left nanoparticle dust will be flushed away by the laminar airflow from the flowboxes above the optical table and will not reach the respiratory system. Finally, the laboratory has a climate system which allows the air to be exchanged at least twice a day and thus the left nanoparticles to be removed. Even without these precautions, a whole year was estimated to reach a perilous particle level.

Figure 5.1.: Machined capillary half with gas inlets. At the inlets the deposition of the ejected dusty material can be seen which is easily blown away by any kind of airflow.

6. Machining

6.1. Preexamination

At the beginning of the machining project parameter studies were performed to find a favourable working point. Therefore the sapphire crystals were placed into the machining device and exposed to the laser radiation. Afterwards, the samples and the created structures were observed and analyzed using the KEYENCE Digital Microscope VHX-600. Besides watching, this device also offers the possibility of spatial measurements.

Initially single shots and bursts of shots were send to the probe to determine the damage profile. Therefore the laser system had to be run in a special mode so that one could shoot with the laser by clicking on a "Fire" button. Although a high optical magnification was available, the single craters could not be relocated on the surface. It was quite difficult to distinguish between either damaged surface structures and dirt particles as illustrated in Fig. 6.1.

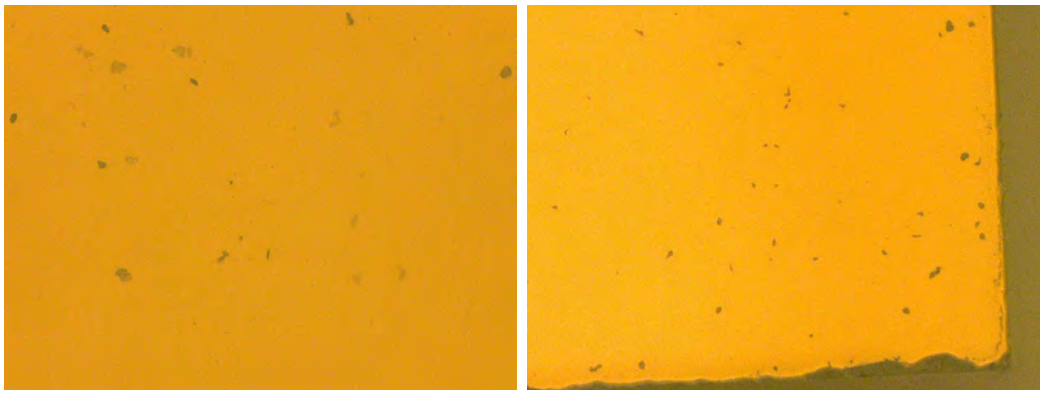

Figure 6.1.: Comparison of crystal surface. On the left picture a machined part of the crystal surface is shown, whereas on the right the natural, raw surface is illustrated. As it can be seen, they neither differ nor can a clear damage structure be found.

That is the reason why, henceforward, the crystals were always recleaned before the "observation" and later on an energy scan was performed by milling simple lines across the sapphire crystal surface so that the machined structures could easily be recovered. For the energy scan different laser power levels and thus different pulse

energies were used to cut paths of varying widths. This sample is shown in Fig. 6.2. The power was tuned via the adjustable attenuator from 10 mW to 50 mW. For each of the chosen power levels a single path was created by moving the mounting stage with a speed of 2.4 mm/s, which is the preconfigured setting of the provider. Hence, the laser shots of 20 μm in diameter should be overlapping by about 85 %. Apart from the lowest power case, all of the channels possess a smooth leveling with sharp edges. In the other case, the formation of an entire channel cannot be observed and the structure is clearly identified as the superimposing of single damage spots leading to a "wobbly" structure. This indicates that the power of 10 mW was close to the damage threshold of the sapphire crystal. The correlation of input parameters and the resulting channel diameters is displayed in Tab. 6.1. Besides the areal damage, the depth of the channels was estimated to be about 7 ± 1 μm and did not significantly vary for the different applied energies.

Table 6.1.: Results of the energy scan.

power P [mW], energy E [μJ]	channel diameter D [μm]
50	29.3 ± 0.5
40	24.9 ± 0.5
30	21.5 ± 0.5
25	20.5 ± 0.5
20	17.3 ± 0.5
10	7 - 9

These data can be utilized to determine the damage threshold of the sapphire plates. The evaluation can be done using the correlation of the squared damage size diameter D^2 and the energy fluence Φ [Liu82, WLZ+04]:

$$D^2 = 2w_0^2 \ln\left(\frac{\Phi_0}{\Phi_{thr}}\right)$$

with Φ_{thr} being the damage threshold energy fluence and Φ_0 the maximum laser fluence depending on the laser pulse energy E_{pulse}:

$$\Phi_0 = \frac{2E_{pulse}}{\pi w_0^2}$$

A fit of the data points following this distribution is shown in the logarithmic plot in Fig. 6.3. The zero line crossing, indicating the damage threshold, is at $P_{thr} \simeq 9.5$ mW. With the focal spot size of $w_0 = 10$ μm the corresponding threshold energy fluence is evaluated to be $\Phi_{thr} \simeq 6.0$ J/cm^2. Additionally, the linear slope of the graph yields the laser spot size, creating the damage structures at the crystal surface. Differing from the originally obtained value, a radius of $w_0' \simeq 15$ μm was found. This might be explained by machining slightly out of focus and indicates the difficulty of correct sample positioning. Evaluation of the damage threshold using

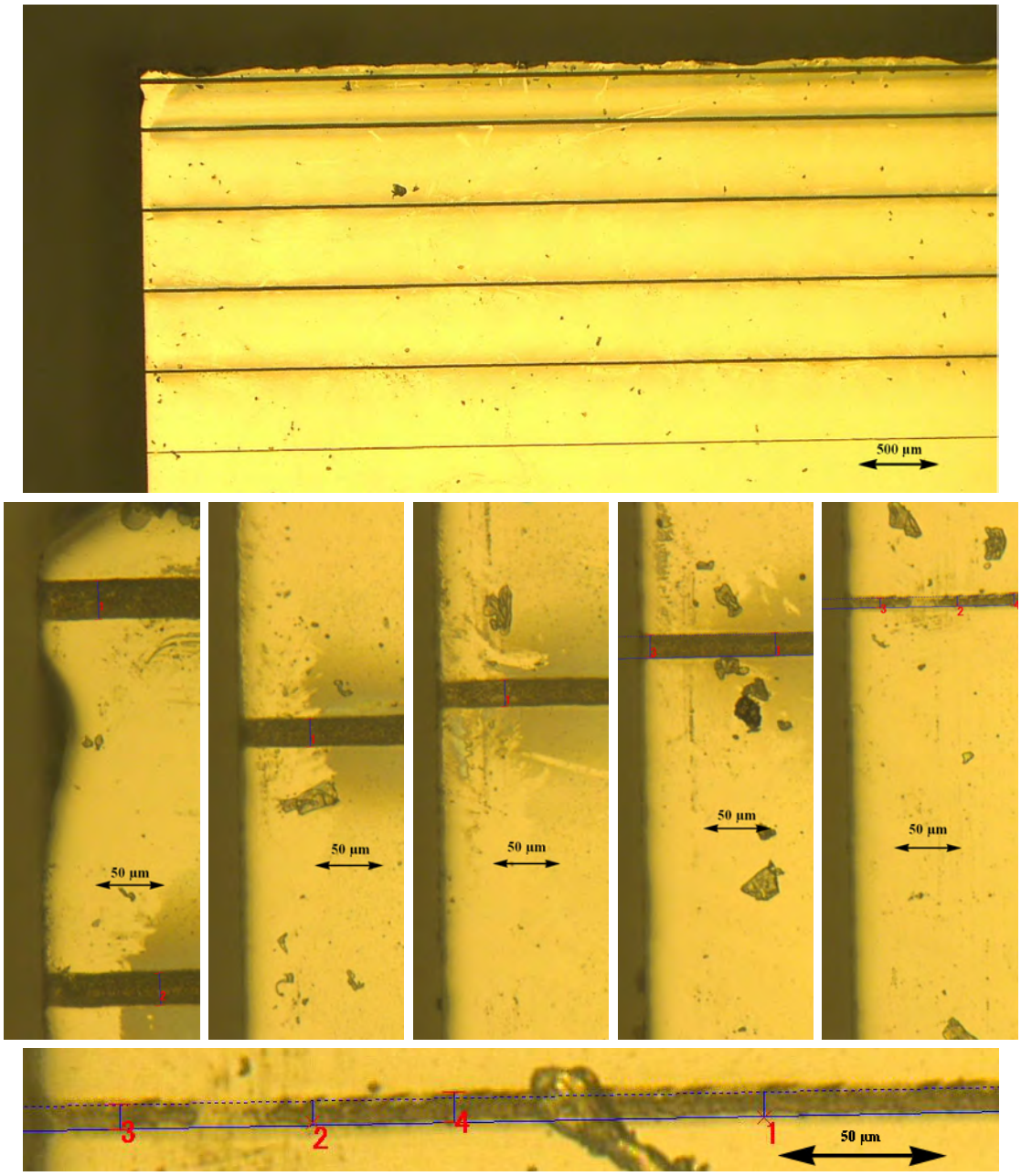

Figure 6.2.: Energy scan. Single lines milled with different laser powers (P = 50, 40, 30, 25, 20, 10 mW from top to bottom) along the sapphire crystal for damage characterization. Additionally, a part of the single channels is zoomed and imaged below corresponding the power decrease from left to right. Compared to the higher power cases, which possess a smooth leveling with sharp edges, the line cut with the lowest power has a wobbly structure (extra zoom in bottom row). This indicates milling next to the damage threshold.

this measure involves $\Phi_{thr} \simeq 2.6$ J/cm^2. Despite the inaccurate assumption of the working laser spot size, both damage threshold values match to literature values. The damage threshold fluence for fs-machining of sapphire surfaces was reported over a wide range from about 3 J/cm^2 [ARV$^+$97, WLZ$^+$04] up to $5 - 11$ J/cm^2 [Mar08, UBC$^+$07]. Taking into account the laser shot overlapping and the fact that Φ_{thr} is reduced by an increase in the laser shot number hitting the same area, the corrected damage threshold seems to match more closely.

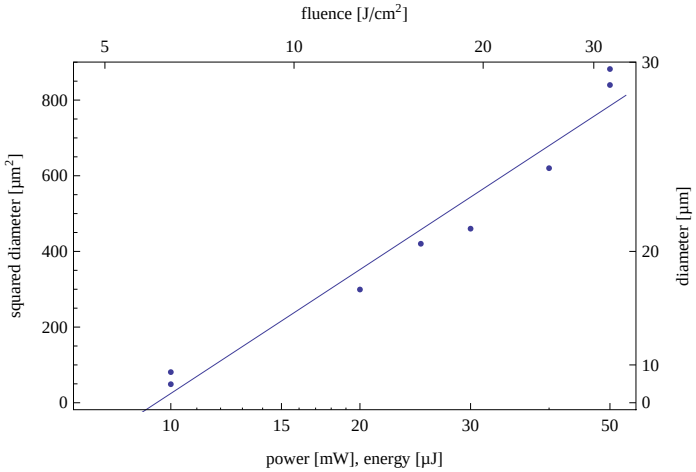

Figure 6.3.: Energy scan fit. The measured cutting diameter is plotted against the applied input power or energy. A logarithmic fit is added [Liu82]. The crossing of this graph and the abscissa displays the damage threshold. For a better comparison the power, respectively the energy, is transformed to the fluence assuming a focused beam size of radius $w_0 = 10$ μm (cf. sec. 4.2).

The power level for ongoing machining was chosen to be 30 mW. This value offers sufficient energy to properly machine the sapphire surface, far enough from the damage threshold with regard to laser instabilities. In addition it does not produce too much dust and dirt, which pollutes the surface surrounding the cut structure (shaded, darker regions in Fig. 6.2). Additionally, a damage size in the same order as the focal spot size of 20 μm diameter will be created. An increase in energy would on one hand shorten the manufacturing time, but on the other lead to less accuracy for precise channel tapering. The reverse is of course true for an energy decrease. The translation speed of the mounting stage was left at 2.4 mm/s. It might be increased up to 10 mm/s such that the laser spot is moved by a distance equal to its radius from one shot to another. This would naturally expedite the manufacturing process but would also result in a "bumpy" channel edge as indicated in Fig. 6.4.

As next step the spacings between the single lines, created as previously explained, were investigated. In order to accomplish this, the stage accompanying control software OWISoft was used in the "meander mode". After setting the length as well as amount and repetition of the displacement of the single lines, a two dimensional

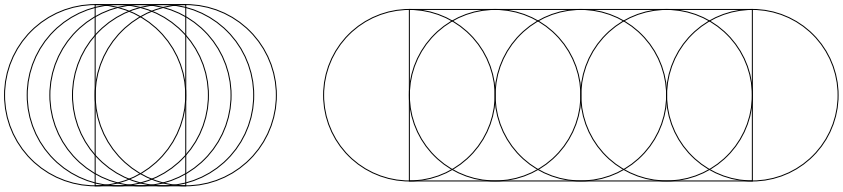

Figure 6.4.: Overlapping of laser pulses (circles) with a translation stage velocity of 2.4 mm/s and 10 mm/s (left and right respectively). The rectangular symbolizes the thereby volitional created channel. The higher moving speed results in a bumpy channel edge differing from the preferred rectangular shape.

array was machined. The spacing distance was varied from 5 μm to 15 μm as pictured in Fig. 6.5. The first try was malfunctioning due to laser beam clipping in the transferline between amplifier system and machining setup. The following manufactured channels showed a nice shape. Their machined surfaces are in one direction not very well structured depending on and enhanced by the spacing distance. To compromise about this fact and considering machining time, the median of 10 μm was chosen. Thus the laser shots are shifted by half the focal spot size. Testing all the parameters, finally a hands-on capillary of 100 μm in diameter was created in a same manner as described before, taking into account the circular shape of the depth profile. Therefore, the ablation arrays, which varies depending on the machining depth, were manually calculated and adjusted and an additional movement of the stage of 7 μm was introduced after each layer, to get the sample back to the focal plane. For the first handcrafted attempt it got a quite round shape.

6.2. Control software

To go on and machine a well sized capillary, a program was developed using the software LabVIEW from National Instruments. General virtual machines (vi's), which are the programs created with LabVIEW, for simple movements of the single axis came along with the motorized stage. These were expanded according to the requirements.

Fig. 6.6 shows the graphical user interface (GUI) of the main control vi. The upper part is the original stage GUI and the lower, boxed part is added for the capillary machining. After starting the program and initializing each of the three axes of the stage, the green lights become lit, indicating that the corresponding motor is ready to work. Using the numerical panel the actual position and the target can be set via the according button. Rough adjustment can also be performed via the turning knob. This could be used, for example, for setting the focal plane to zero so it can be easily restored. The unit of the position values can be selected by the option field, either inches or millimeters. Depending on the target mode, the selected axis moves either a certain distance, starting at the current position, (relative mode)

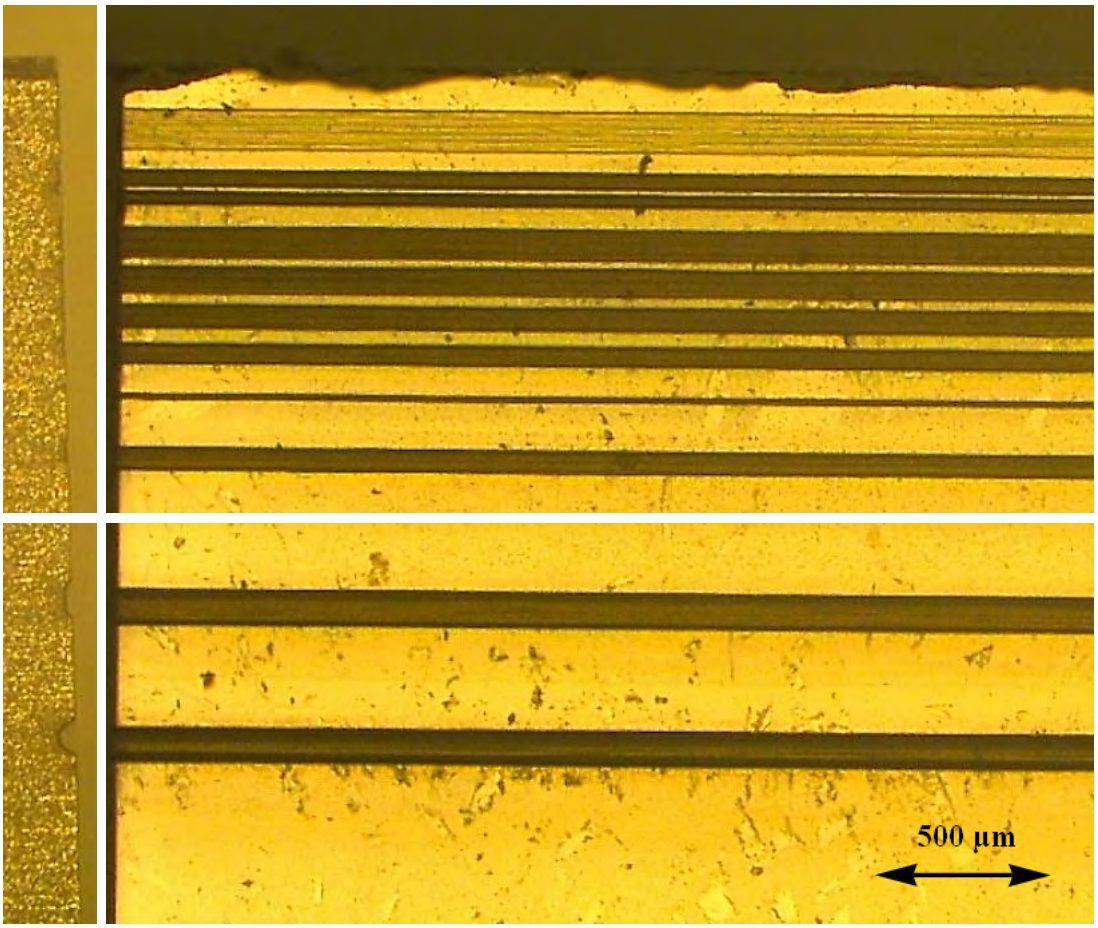

Figure 6.5.: Line spacing variation and first hands-on capillary half with 100 μm diameter in side and front view. The power was set to $P = 30$ mW with a translation stage velocity of 2.4 mm/s. The distance shifting combinations (from top to bottom) are: 10×10 μm, 5×7 μm, 5×5 μm, 5×15 μm, 5×13 μm, 5×11 μm, 5×9 μm, 1×10 μm, 5×10 μm. The first areal looks abortive due to beam clipping during the laser beam transfer from the amplifier to the machining setup, which was corrected before continuing.
Additionally, the last two channels are an aborted and an entire semi-automatic capillary half done by the following shift parameters, each set separated by 7 μm depth change to return to the focal plane after array ablation: 8×10 μm, 8×10 μm, 8×9.5 μm, 7×10 μm, 7×9 μm, 6×8.5 μm, 4×8.5 μm.

or to a certain position (absolute mode) determined by the target value. To start the motion, the "Go to position" button has to be pressed or alternatively "Go with speed", which uses the maximum available velocity. The usual velocity can be determined from a pull-down menu in the task bar, which arises after the program execution. The velocity profile characterizing the acceleration scheme is set via the position-mode menu to a trapezoidal shape instead of a s-curve. The motion of each axis can be interrupted pressing the STOP button. The buttons for a reference drive (e.g. for calibration) and switch releasing (motor restarting after stopping due to the triggering of one of the endswitches) are usually not needed. Additionally, the actual stage velocity and the axis status or possible failures are shown in corresponding panels.

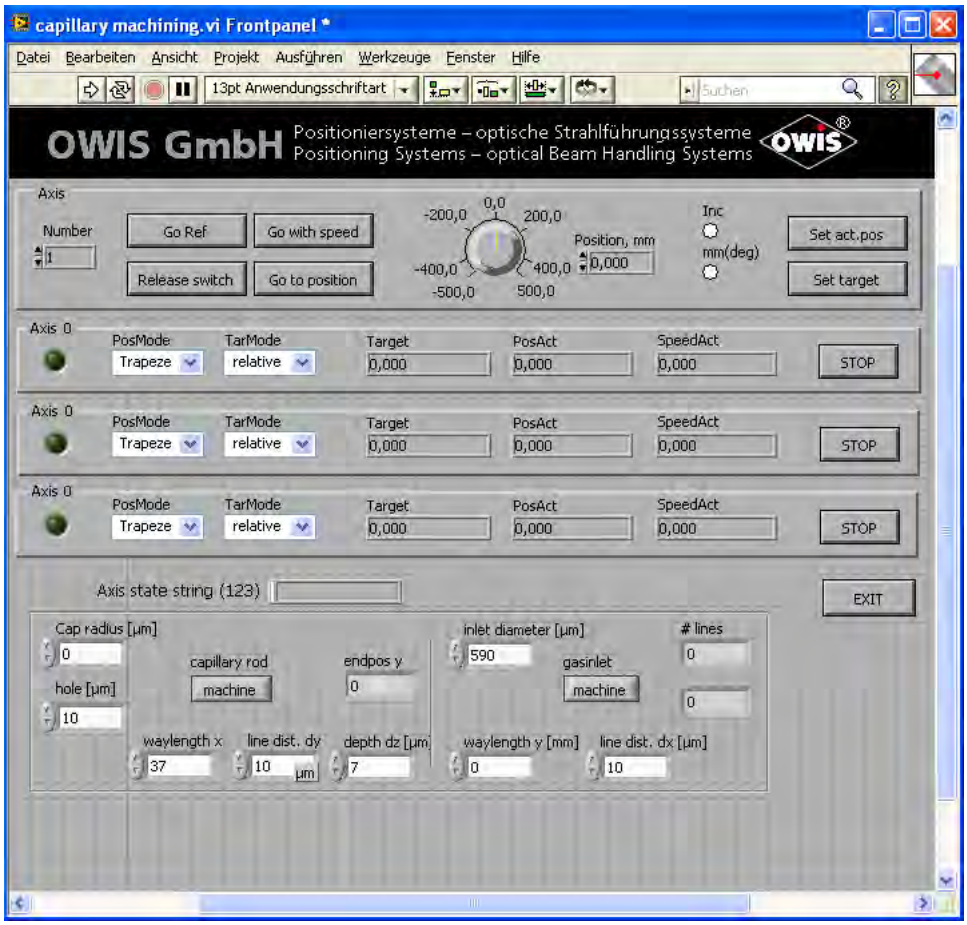

Figure 6.6.: LabVIEW machining user interface.

For the machining of either a half capillary or a gas inlet, the desired parameters just have to be set. These are for the capillary: its radius, the single shot hole radius (actually 10 μm as found beforehand), the capillary length x (horizontal direction), the line spacing dy (vertical direction) and the depth motion dz (laser propagation direction). The last three parameters are set to 37 mm for a 33 mm long

sapphire plate, such that the milling velocity is reached before the surface interaction occurs, as well as 10 μm and 7 μm respectively, as a result of the aforementioned measurements. For a gas inlet its diameter, the distance to reach the capillary from the crystal edge y and the line spacing dx have to be added. The numbers displayed in Fig. 6.6 are pre-set standard values and can of course be easily changed.

As soon as one of the "machine" buttons is pressed, it becomes red and either the capillary or the gas inlet will be machined (in horizontal or vertical direction, respectively) via a sub-vi (Fig. 6.7). Machining begins from the current motor position. Therefore, the array diameter and the corresponding number of single lines is calculated before milling it, depending on the capillary radius, the depth and the hole size. For the capillary its round shape is also taken into account. Subsequently, the sample is moved with respect to the laser beam. At first in x direction across the sapphire crystal, then one step aside, corresponding the line distance spacing, and back across the surface, followed by an additional transverse movement. This is repeated until completion of the two dimensional array. Then the z direction is incremented; the sample is re-moved to the focal plane. This procedure is repeated as long as the whole three dimensional target region is machined. Since the capillary should be centered on the sapphire plate, the stage has to be moved to the correct start position before initiating the procedure. The same concerning the start position is true for the gas inlet, such that the position has to be changed in between machining of the capillary and each inlet.

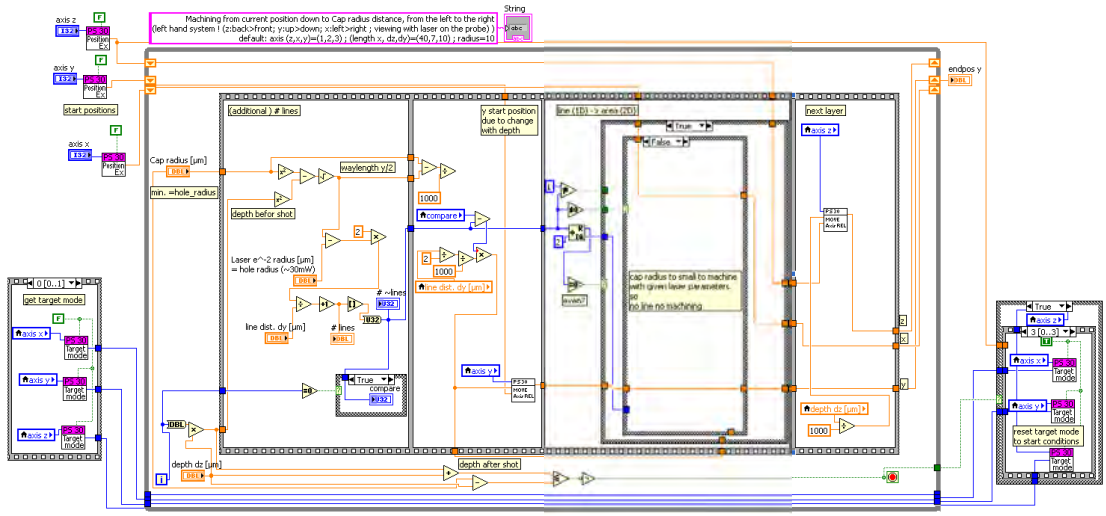

Figure 6.7.: Block diagram (code) of the capillary machining program. Pictured is the cases, where no machining is done due to missing or too small cap size (security query). The other block diagram cases can be found in the appendix. The corresponding gas inlet codes are quite similar.

6.3. Resulting sapphire capillary plates

For the capillary production two standard sapphire plates of the following dimensions are available, which have been provided by Gavish based in Israel: $15 \times 20 \times 4$ mm and the nearly doubled $33 \times 20 \times 4$ mm.

The larger crystal was used to fabricate a capillary in accordance with the simulation in chapter 3, i.e. 250 μm $\times$ 30 mm capillary with 600 μm inlets 2 mm displace from the edges. Using the LabView program, the machining of the a capillary rod half takes about 1.5 hours. The milling of a single inlet, from the top of the crystal to the capillary, takes about 7 hours due to large material removal. The final sample is shown in Fig. 6.9. A circularly shaped capillary was manufactured with inlets much bigger than the capillary itself. In this case the inlets reach to the capillary center. This might also be changed to pass across the whole diameter. The bright structures, which can be seen at the crossings, are dirt and dust from the ablation, depositing back again onto the surface. This can easily be removed by an air brush or via diamond paste, which might be used anyway for polishing the capillary surface.

If the sample crystal is not correctly positioned within the holder the capillary will not be correctly formed. Therefore, special care has to be taken when placing the crystal into the holder. An example can be found in Fig. 6.8, where the depth of capillary and inlets changed along its length, indicating a tilt of the crystal. To avoid this, in future attempts each corner of the sapphire crystal was illuminated after mounting by the strongly attenuated laser beam and checked for differences in the reflected spot size. If so, it had to be remounted and was rechecked afterwards to ensure no tilt. Once the surface alignment was corrected, the machining process could be triggered. This technique is necessary for reproducibility.

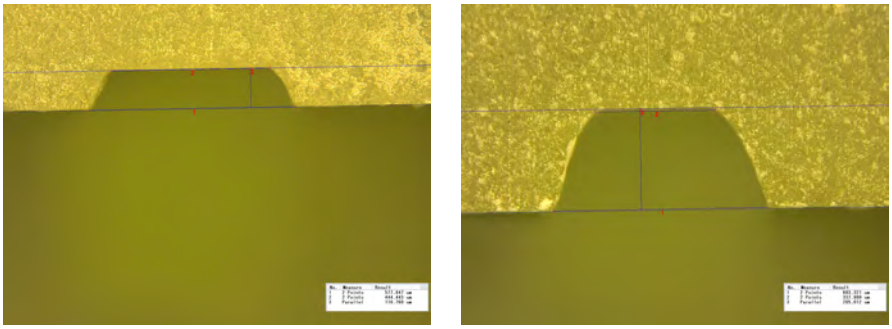

Figure 6.8.: Early attempt of inlet milling. The two inlets with the same set of parameters on one sapphire plate strongly differ. The same distortion behavior was observed for the capillary. This indicates the problem of improper crystal placing i.e. with an angle between laser axis and surface normal.

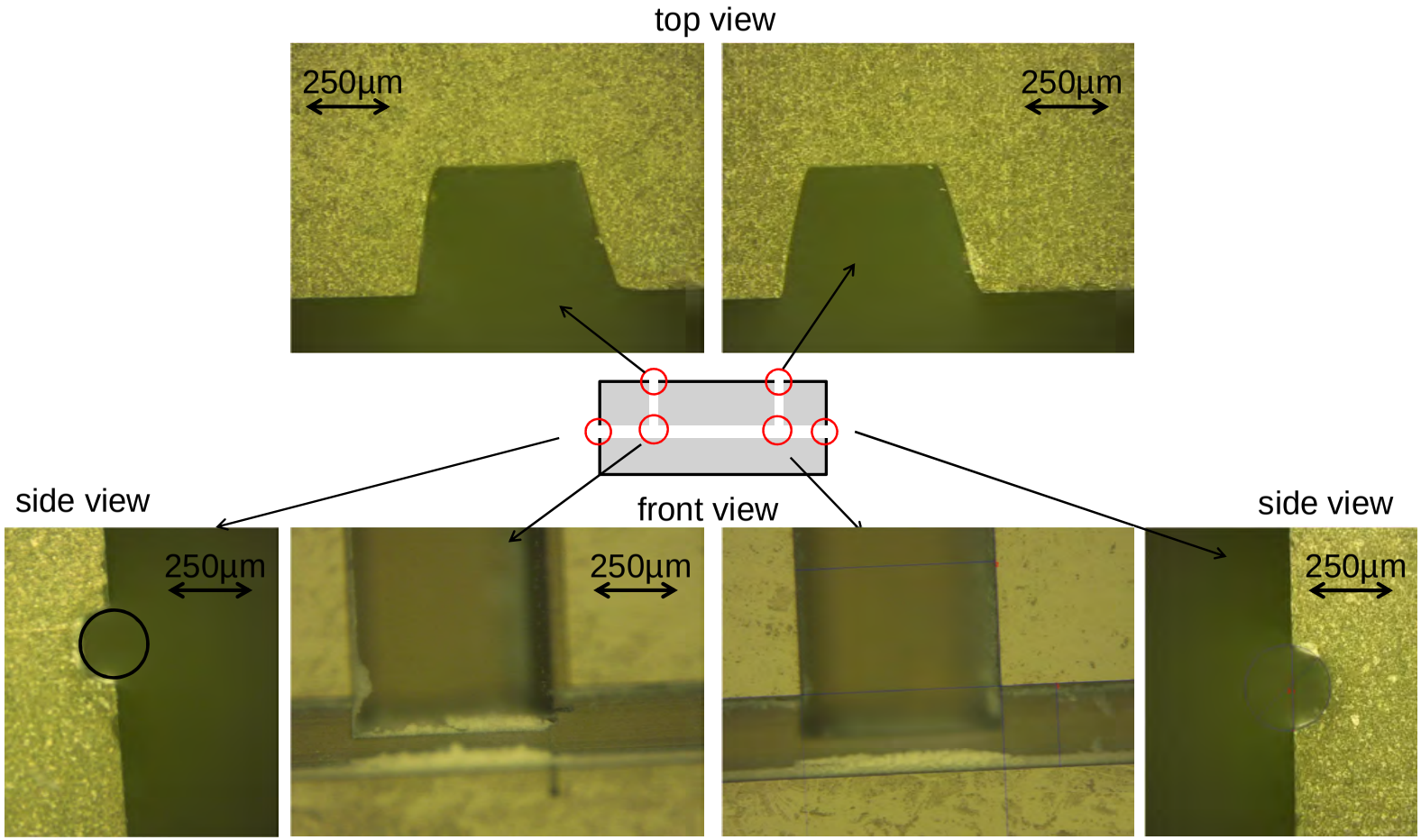

Figure 6.9.: Final capillary half. Shown are the characteristic patches. On top, the inlet profiles can be seen, whereas in the bottom row the capillary profile and the crossing of both, the capillary channel and the inlets, is imaged. All pictures are taken with the camera focus on the sapphire crystal surface, with the exception of the left-hand crossing. There, the focal plane is placed at the capillary wall. The shape of the capillary is underlined by the black circle.

7. Characterization

As the final step of the gas target development, after design and fabrication, the capillaries need to be characterized. Their resulting density profiles should be investigated to prove the validity of the simulations and the machined geometries. Previously, this has mostly been done by interferometric techniques [GRRB$^+$07, JTK$^+$03, SBH99, KSCZ99] which require rectangular capillaries with polished surfaces, in order to preserve the phase of the transmitted laser beam inside the sapphire bulk. This is not applicable to the capillaries presented here due to their rough, non-rectangular walls. Therefore the gas density profile is determined via the combination of Raman spectroscopy [RK28] and longitudinal interferometry. The Raman signal provides the spatial resolved density outline [WGS$^+$11] while the longitudinal interferometry signal is used for the absolute line-integrated calibration.

7.1. Raman spectroscopy

Energy transfer between light and particles (atoms, molecules, ...) can appear as fluorescence or scattering. Fluorescence can be observed, if the illuminating photon energy (cf. (2.8)) matches the energy difference between the particle's ground and real excited state. Such restrictions do not account for scattering, where a virtual excited state is reached. During this process, most photons are elastically scattered. However, a small fraction of them is inelastically scattered through interaction with molecular rotation and vibration modes, phonons or other internal excitations. In the elastic case, also called Rayleigh scattering [Str99], the observed, scattered light has the same frequency ν_0 as the source, whereas in the inelastic case a frequency shift occurs ($\nu_0 \pm \nu$). These are the Raman lines or bands, which are termed Stokes ($\nu_0 - \nu$) and Anti-Stokes ($\nu_0 + \nu$) depending on the direction of the shift (Fig. 7.1).

To understand this circumstance, the polarizability α has to be considered, which represents the ability of a surrounding electric field $\vec{E}$ to induce a dipole moment:

$$\vec{\mu} = \alpha \vec{E}$$

Polarizability is isotropic for atoms and may vary for molecules with respect to their position depending on their symmetry [Bal01]. The polarizability at the nuclear equilibrium geometry α_0 changes with time t due to rotations or vibrations. Assuming a sinusoidal motion

$$\Delta r = \hat{r} \cos(\omega_v t)$$

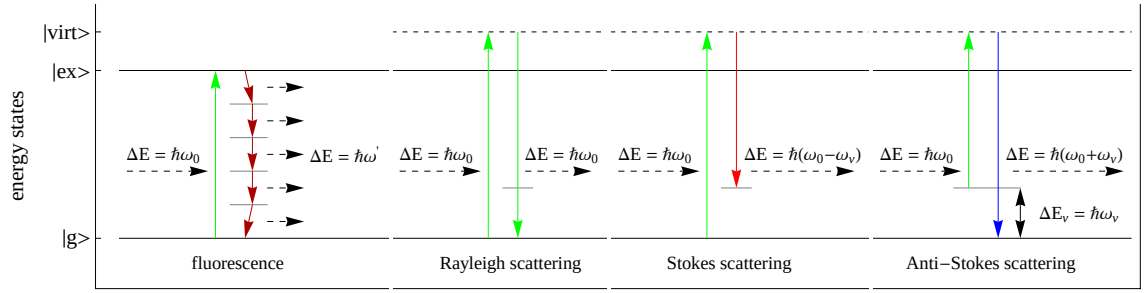

Figure 7.1.: Illustration of fluorescence, Rayleigh scattering and Raman (Stokes & Anti-Stokes) scattering. The solid lines indicate real states, such as the ground $|g\rangle$ and excited state $|ex\rangle$. The dashed line indicates a virtual state $|virt\rangle$. E_v is the vibration-state energy responsible for the typical Raman-frequency shift.

with amplitude $\hat{r}$ and angular frequency ω_v, the polarizability results in:

$$\alpha = \alpha_0 + \Delta r \frac{\partial a}{\partial r}$$

A photon-induced electric field $\vec{E}$ of amplitude $\vec{E}_0$ and frequency ν_0 reads as:

$$\vec{E} = \vec{E}_0 \cos(\omega_0 t)$$

By dint of the addition theorem $\cos(a+b) + \cos(a-b) = 2\cos(a)\cos(b)$, the polarizability evolves to:

$$\begin{aligned} \vec{\mu} &= \alpha_0 \vec{E}_0 \cos(\omega_0 t) + \hat{r}\vec{E}_0 \frac{\partial a}{\partial r} \cos(\omega_0 t)\cos(\omega_v t) \\ &= \alpha_0 \vec{E}_0 \cos(\omega_0 t) + \frac{\hat{r}\vec{E}_0}{2} \frac{\partial a}{\partial r} \left[\cos\left((\omega_0 + \omega_v)\, t\right) + \cos\left((\omega_0 - \omega_v)\, t\right)\right] \end{aligned}$$

The first term denotes the Rayleigh scattering with no frequency shift, whereas the latter terms correspond to Stokes $(\omega_0 - \omega_v)$ and Anti-Stokes $(\omega_0 + \omega_v)$ lines of the Raman signal. The frequency shift ω_v is independent from the wavelength of the incident light, but related to the quantized motion of the molecules, which is an intrinsic property of a sample and thus might be used for their identification. Besides wavelength or frequency, the Raman shift is often expressed in wavenumbers $\tilde{\nu} = \lambda^{-1} \propto \nu$.

One of the biggest challenges of Raman spectroscopy is its measurement since the probability of an inelastic Raman scattering event is much lower than an elastic Rayleigh scattering event (about $1 : 10^7$) [Bal02]. This has to be taken into account regarding the design of the experimental setup. The setup is illustrated in Fig. 7.2. A VERDI V5, the same as the oscillator pump mentioned in sec. 4.1, is used as laser. The laser beam is focused by a $f = 350$ mm plan-convex lens into the capillary. With a focal spot size of $w_0 \simeq 81$ μm, the Rayleigh range is $z_R \simeq 38.7$ mm. The sample is placed on a remote controlled $M-824.3VG$ Hexapod from Physik Instrumente (PI)

inside a vacuum chamber, which offers all degrees of freedom for precise alignment. Through two $f = 30$ mm aspheric lenses, each with a 2 inch diameter, the scattered light is imaged by a pilot piA1900-32gm GigE CCD camera from Basler. It has a 1928×1084 pixel chip, each 7.4×7.4 μm, capturing with 12 bit resolution. Between the lenses a filter system is placed, consisting of a 532 nm longpass filter of optical density (OD) 6, a 690 nm shortpass filter and a 610 ± 10 nm flat-top bandpass filter, both of OD 4. The latter can be tuned through rotation ($\sim 10°$). Hence, the Rayleigh signal should be suppressed as well as the Raman signal from the sapphire (693 nm [WGS+11]). To hide unwanted reflections or stray light, the imaging system is additionally covered in a black lens tube. The capillary is connected to a gas system from HTK which can be used to control the pressure of filling gas. As gas species molecular nitrogen gas is chosen, which yields a Raman signal from the first vibration level at 607 nm when irradiated with 532 nm light. The density profile is obtained via the relation between the laser intensity I_L and the captured Raman signal I_R [Dem07]:

$$I_R \propto n_e I_L \tag{7.1}$$

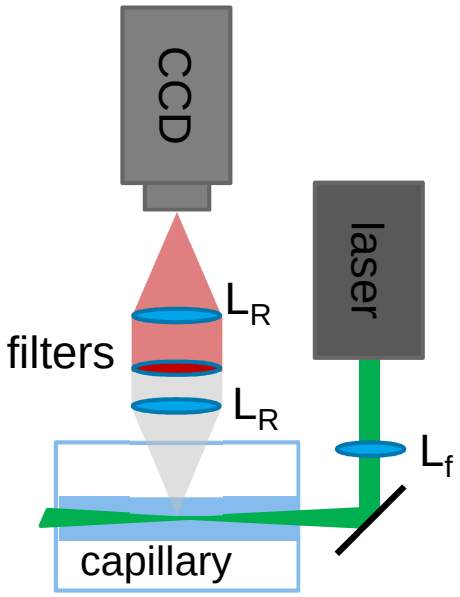

Figure 7.2.: Setup for Raman spectroscopy. (L_R: $f = 30$ mm aspheric lens; L_f: $f = 350$ mm plan-convex lens)

7.2. Interferometry

After obtaining the spatially resolved density profile along the capillary axis, the absolute calibration is done via longitudinal interferometry. Therefore, the laser beam needs to be split into two parts using a 50 : 50 beam splitter. One branch is send through the capillary (cf. Raman spectroscopy) and the other one is guided around the capillary as reference. An $f = 750$ mm plan-convex lens subsequently collimates each of the beams. Afterwards, an equivalent beam splitter is added for the recombination and superposition of both branches (Fig. 7.3). A CCD camera (the same model as used in the machining setup on page 36) images the interfered beam. An interference pattern of high and low intensity fringes is observed. Propagating through the capillary, the optical path length and thus the phase of the light field will change, depending on the including matter. The introduced phase ϕ along a distance l results from the accumulated refractive index $\eta \overset{p.21}{=} \sqrt{1-\left(\frac{\omega_p}{\omega}\right)^2} \overset{p.19}{=} \sqrt{1-\frac{e^2 n_e}{m_e \epsilon_0 \omega^2}}$:

$$\phi(l) = \frac{\omega}{c}\int \eta(\vec{r})\, dl = \frac{\omega}{c}\int \sqrt{1-\frac{n_e}{n_c}} dl \simeq \frac{\omega}{c}\int \left(1-\frac{1}{2}\frac{n_e}{n_c}\right) dl = \frac{\omega}{c} l - r_e \lambda \int n_e(\vec{r})\, dl$$

with $n_c = m_e \epsilon_0 \omega^2 e^{-2} \sim 10^{27}\ \mathrm{m}^{-3} \gg n_e$ the critical plasma density, which is much higher than the investigated gas or plasma densities ($10^{15} - 10^{19}\ \mathrm{cm}^{-3}$), and $r_e^{-1} = 4\pi\epsilon_0 m_e c^2 e^{-2}$ the inverse classical electron radius. The first term belongs to the case of propagating through a vacuum (no matter inside the capillary). If a gas is applied, a phase variation and thus a fringe shift of the interference pattern is established. By comparison of the data or images before and after the introduction of gas, the line integrated density is measured.

7.3. Resulting measurement

Before starting the data acquisition of the Raman signal, the field of view of the camera was calibrated using a scale (cf. Fig. 7.4). As can be seen, the capillary (33 mm) cannot be imaged within a single picture. For this reason, an image was captured every 2 mm along the capillary axis such that the whole capillary can be observed by overlapping all the single images subsequently. The movement of the capillary along the laser axis was achieved using the Hexapod.

For the characterization the vacuum chamber was evacuated and the laser power was set to $P = 5$ W. At each position along the capillary an image was captured both with and without nitrogen gas supply (applied pressure $p = 500$ hPa, exposure time $t_{exposure} = 4.15$ s) Afterwards the latter was subtracted from the former to reduce background noise (Fig. 7.5). The resulting image was binned along the laser axis to obtain the Raman intensity profile $I_R(z)$. In order to retrieve the gas density n, the laser intensity $I_L(z)$ is also needed (cf. (7.1)). Therefore, the capillary was removed and the laser intensity distribution was imaged (Fig. 7.6). The relative gas

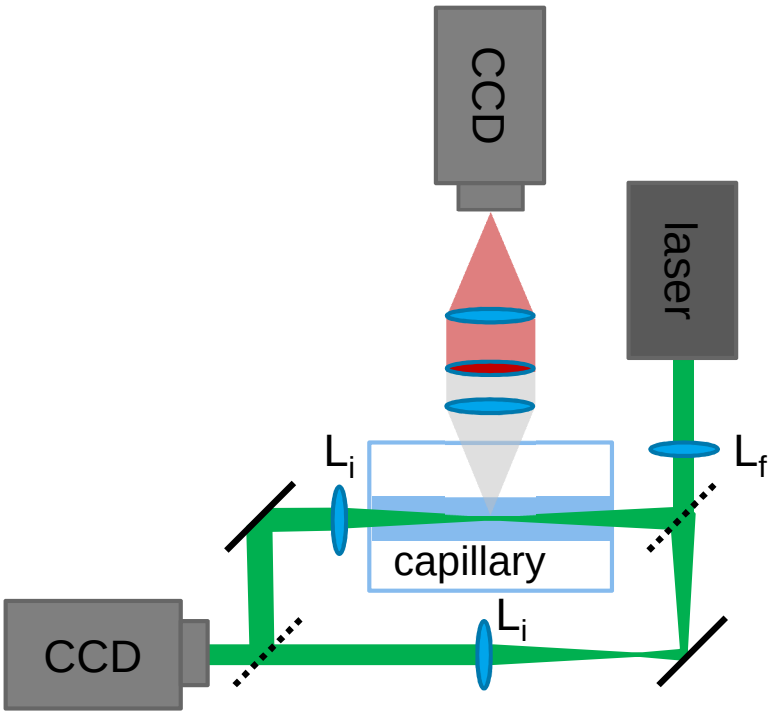

Figure 7.3.: Setup for the characterization, including Raman spectroscopy and longitudinal interferometry. (L_f: $f = 350$ mm plan-convex lens; L_i: $f = 750$ mm plan-convex lens)

density distribution $n(z)$ results from the ratio of the Raman signal $I_R(z)$ to the laser intensity $I_L(z)$ and the subsequent overlapping of all the pictures along the capillary corresponding to their offset. This is shown and fitted by a sixth order polynomial in Fig. 7.8. As it can be seen, it was not possible to measure along the whole capillary due to decreasing intensity of the laser towards the capillary's end. This dramatic intensity decrease might be caused by a too short focal length and therefore also too short Rayleigh range resulting in beam clipping at the entrance of the capillary with progressive offset. In order to obtain a gas density profile along the whole 33 mm capillary anyway, the fit was extrapolated via a shift following the central, linear density decrease.

For the absolute calibration, interferometry is used. Thirty interference pattern pairs of the pre- and post-gas-supply situation were gathered and binned to average for a range of gas pressures up to $p = 500$ hPa (cf. Fig. 7.7). Without this calibration measurement, the relative fringe shift $\Delta s/\lambda$ respectively the accumulated phase can just be determined modulo 2π. The relative fringe shift for $p = 500$ hPa was measured as $\Delta s/\lambda = 7.71 \pm 0.04$ moving in left direction.

In this case a gas and not a plasma was investigated (cf. sec. 7.2). Therefore the

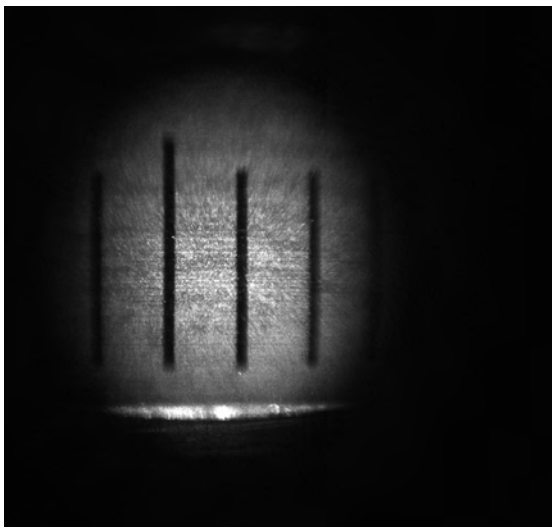

Figure 7.4.: Calibration picture of the Raman setup. The line spacing is 1 mm.

line-integrated gas density cannot be calculated as aforementioned. The phase shift $\Delta\phi$ respectively the relative fringe shift $\Delta s/\lambda$ evolves as follows:

$$\frac{\Delta\phi}{2\pi} = \frac{\Delta s}{\lambda} = \frac{1}{\lambda} \cdot \int (\eta - 1)\, dl = \frac{K_{Gladstone}}{\lambda} \cdot \int n\, dl$$

$K_{Gladstone} = \frac{\eta-1}{n}$ is the Gladstone-Dale constant [GD63], which describes the ratio of the refractive index (compared to the vacuum) to the particle density. For nitrogen it is given by: $K^{N_2}_{Gladstone} = (\eta - 1) \cdot k_B T/p = 2.9944 \cdot 1.38 \cdot 10^{-23}$ J/K $\cdot$ 273.15 K/101.325 hPa $= 1.114{\cdot}10^{23}$ cm^{-3}, assuming the ideal gas equation and standard conditions. Values for η under standard conditions can be found in [Web95]. Hence, the gas density can be calibrated via its line integral.

The result of the characterization depicts a gas density profile with values similar to the theoretical simulation (Fig. 7.9). But it is conspicuous that the density decreases along the capillary. This must be due to different pressures at the two inlets. After mounting the two capillary plates in the holder and connecting the gas feed, some leaking was noticed. The o-rings, used as washers, could not completely seal the connection.

In general it was shown that the characterization setup can be used to verify the gas or plasma density distribution inside a capillary gas target, even though the setup might be improved.

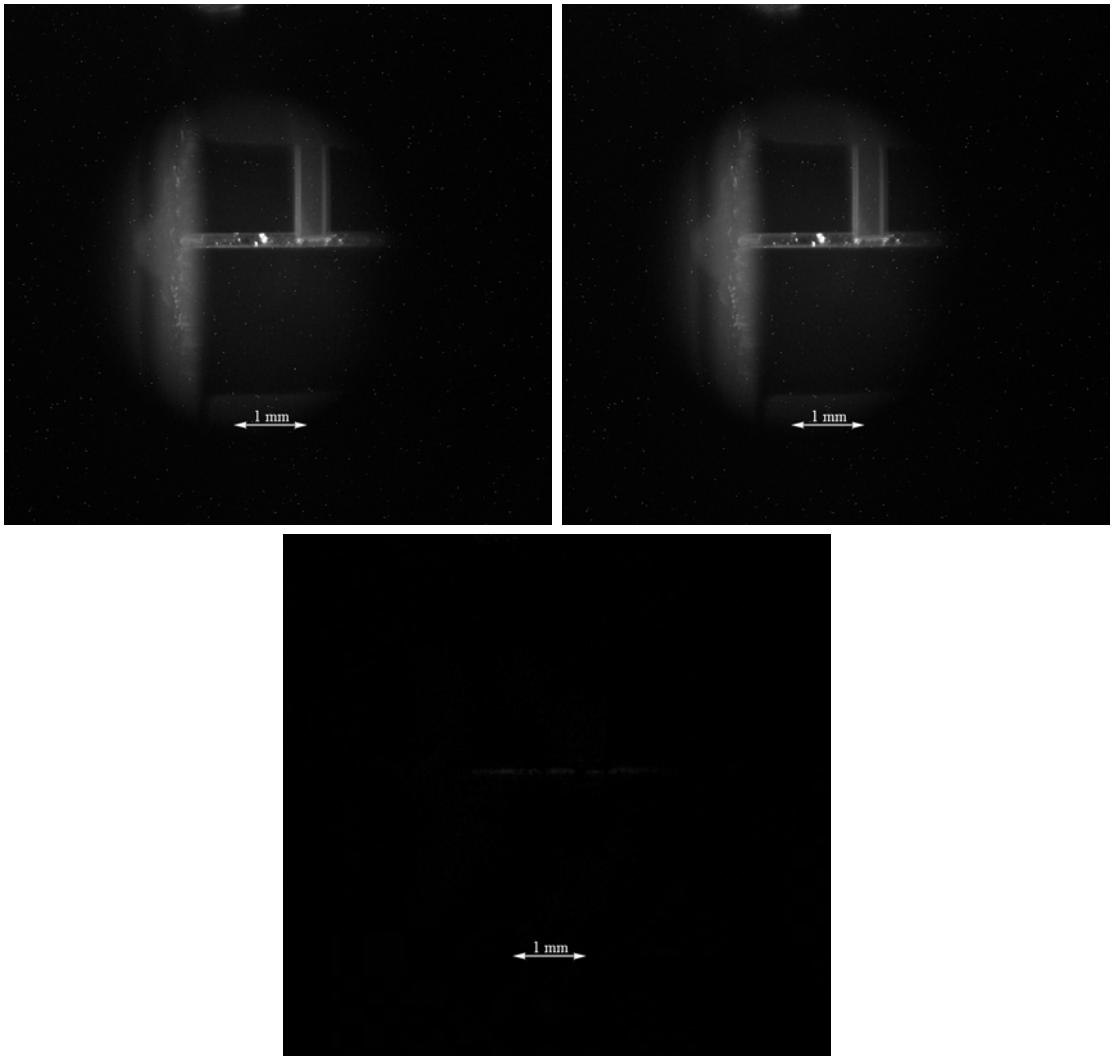

Figure 7.5.: Raman signal at the beginning of the capillary. On the left the raw data and on the right the background signal is shown. The capillary and the gas inlet can be seen in addition to some impurities in the sapphire (bright spots). Below, the background subtracted Raman signal is presented.

Figure 7.6.: Convolution of Laser intensity distribution and the efficiency of the imaging system: On the left the raw data (with gas supply), on the right the background signal and below the background subtracted intensity. The pictures were taken without the capillary to measure just the laser intensity distribution.

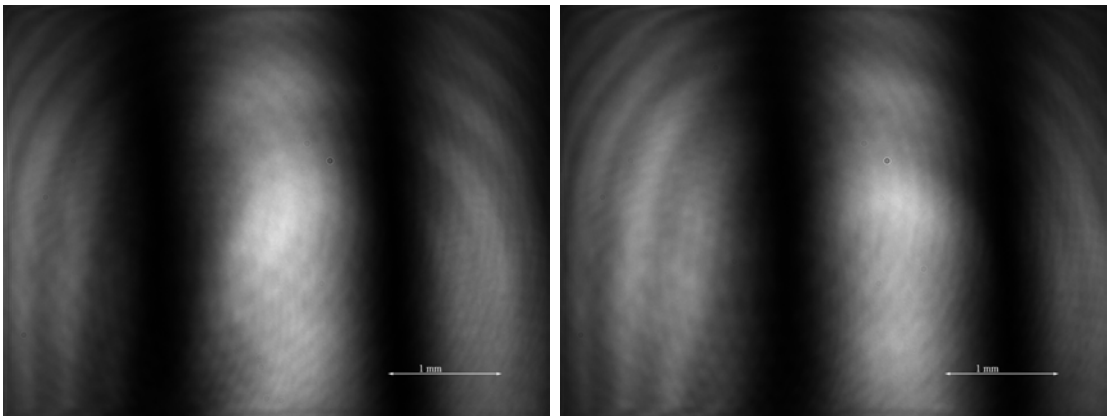

Figure 7.7.: Fringe shift at $p = 500$ hPa. Interferometry fringes before (left) and after (right) N_2 gas supply.

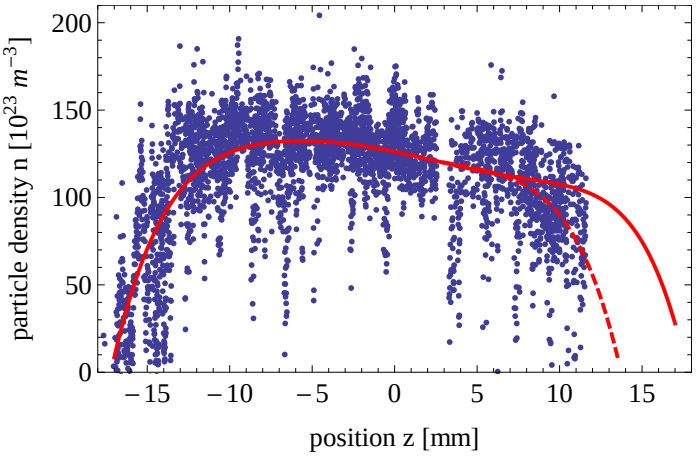

Figure 7.8.: Density profile of the investigated capillary with an applied pressure of $p = 500$ hPa. The data obtained by Raman spectroscopy (blue) is fitted by a sixth order polynomial (dashed red). The data acquisition was not possible along the whole capillary; therefore, the fit was extrapolated over the capillary length by a shift along the nearly linear part in the middle of the fit. Thus, the resulting density line-out (solid red line) could be calibrated by the interferometer results to get absolute numbers.

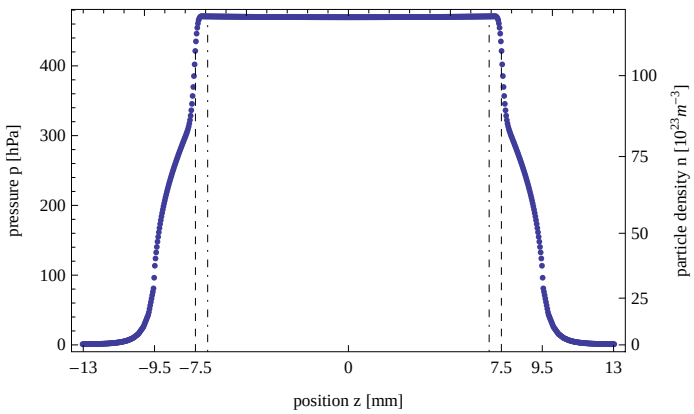

Figure 7.9.: Simulation result (2D) of the pressure p respectively the particle density n (confer Fig. 3.2) for an applied N_2-pressure of $p = 500$ hPa to compare with the characterization result. Remember, the capillary was shortened in the simulation to decrease the computation time. The "real" position values are received by adding 7 mm to each absolute number.

8. Conclusion and Outlook

Plasma wakefield acceleration, for example, driven by a laser (LWFA), is a method, which offers the possibility of high energy particle acceleration on affordable and small scales. Therefore persistent gas targets are required, which contain the energy transferring plasma. Additionally, these structures are suitable for controlled particle injection and acceleration via shaping the gas density profile. This thesis has investigated the design and manufacturing of such gas targets built of sapphire.

The design of targets for different gas-density profiles is makes use of by CFD simulations. The open source software package OpenFOAM allows the simulation of the gas particle flow inside the target and the optimization of its shape. Thereby, it offers a free and powerful toolset for CFD simulation with the possibility of custom, problem-specific modifications.

To fabricate the developed gas targets a fs-micromachining device was constructed and calibrated. A beforehand already disposable Ti:Sapphire amplifier setup was extended by a beamline and a three axis stage with micrometer precision. Although the laser system showed a user friendly behaviour, the laser stability over the day-long machining time is not assured. The manufacturing time could be shortened by an increased motor speed, however this might lead to a rougher channel structure and has not been tested yet. Another possibility would be the outsourcing of the inlet milling, the most time consuming portion of the machining process. The inlets do not need to have as high precision as the capillary channel itself. Therefore, the laser-time could be reduced by other milling principles as for example water-jet milling, diamond sawing or supersonic drilling. All these techniques are available at the university machine shop and could thus be used after testing. To allow angular adjustment and alignment of the sapphire plates and to improve the reproducibility a rotational stage will be added to the stage during the next days, thus the capillary channel can be machined absolutely perpendicular to the crystal edge. Hence, both crystal halves will fit perfectly together and the leakage of the gas feed will be reduced respectively even stopped.

For examination of the simulation results and the real gas-density distributions inside the capillaries a characterization station consisting of transverse Raman spectroscopy and longitudinal interferometry was set up. The Raman signal provides the gas density profile whereas the interferometry allows absolute calibration. Besides the aforementioned capillary mounting challenges, the acquired data fits quite well to the simulation results. For the future it might be desirable to image the entire capillary at once to avoid the overlapping procedure of its single parts. Addition-

ally, a focusing lens with a longer Rayleigh range needs to be inserted for such small capillary diameters to prevent beam clipping and stray light at the laser incoupling into the capillary channel such that the whole gas density profile could be directly measured without linear interpolation. The next step involves the installation of the discharge for measurement and characterization of plasma densities.

A nozzle and an outlet will also be added to the capillary for application in external acceleration experiments at the Lund laser facility and later on at Desy to create a gas density peak at the beginning of the channel for density down-ramp injection. This nozzle will be machined in the same manner as a usual inlet just with the diameter decreasing towards the capillary channel. The software code needs to be slightly adapted to achieve this. The outlet of the nozzle is an inlet at the opposite side of the capillary channel. Generally, the setup is created to machine almost arbitrary shapes. The inclusion of a remote controllable shutter technique, to turn the laser on and off during the machining process, is desirable. In the future, the control of the motorized stages should be realized via a graphical input for arbitrary shaping. It is thought of a pixel resolved graphics-data format, which symbolizes the front, laser-processed surface of the sapphire plates. The machining depth is color coded. Finally, a software, which has to be developed, should read a drawn picture array and perform the capillary machining automatically from the included information.

An example of arbitrary shapes is planed by turn of the year. Instead of the presented standard straight capillary channel it is planned to use a wiggled respectively wavelike structure. Such a gas target could later on possibly be used as a combination of accelerator and undulator for radiation sources. In the experiment first guiding and acceleration test will be performed.

A. LabVIEW block diagrams

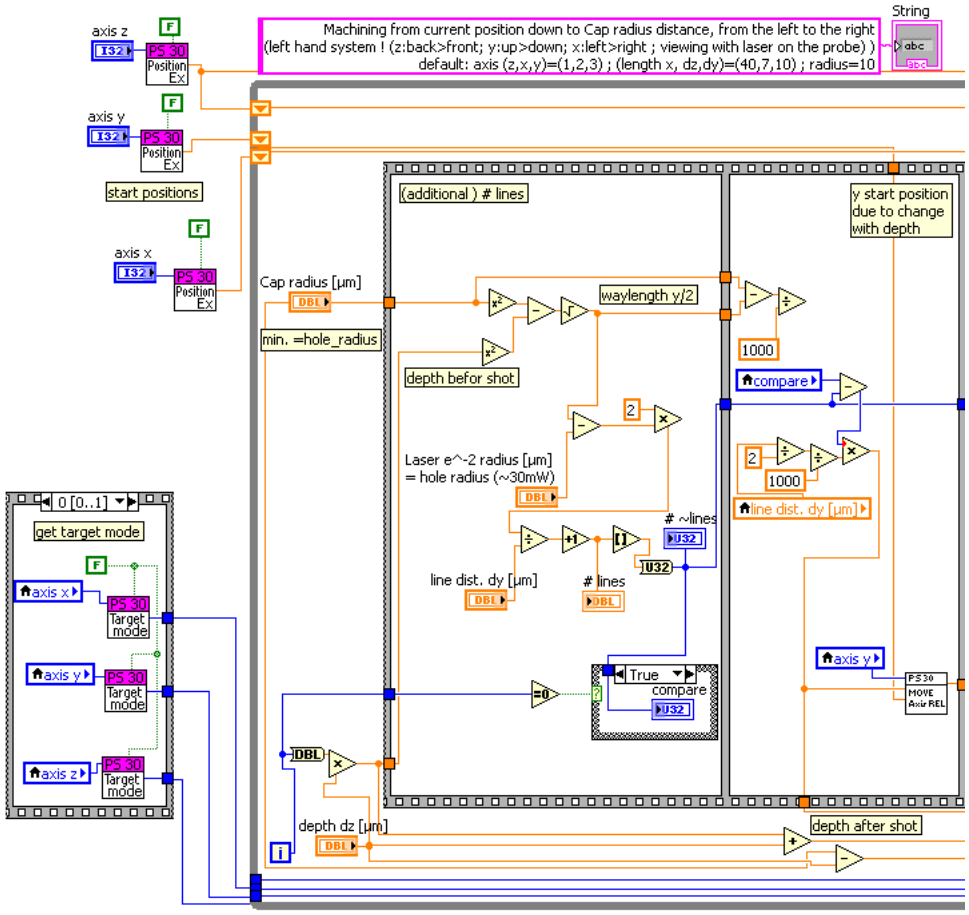

Figure A.1.: Block diagram part 1: First part of the machining block diagram to determine the ablation layer width and start position, which changes depending on the actual machined capillary depth. Additionally, the formerly selected positioning mode is grabbed and set to the used mode.

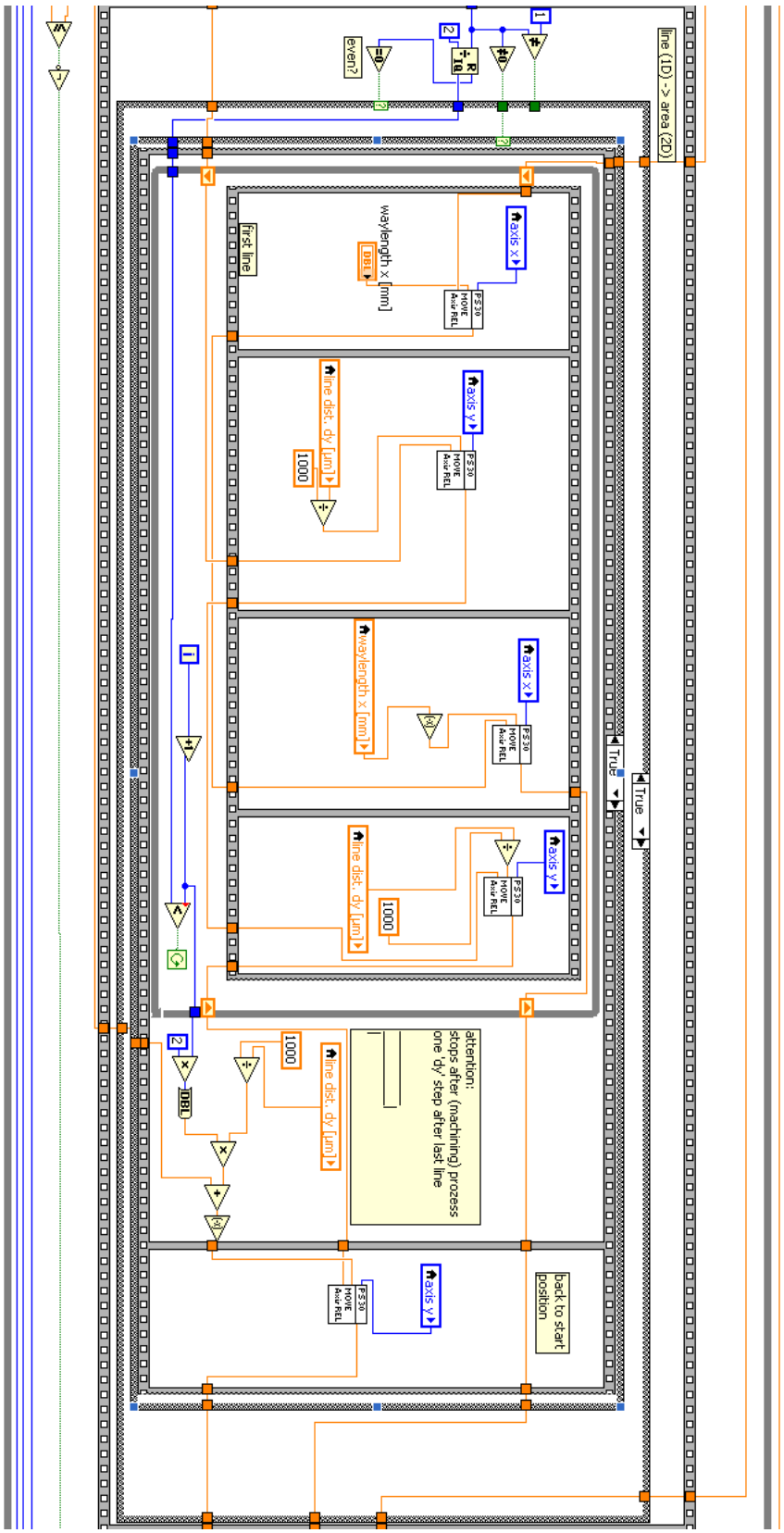

Figure A.2.: Block diagram part 2 case a: Loop to machine ablation layer with even number of single lines and subsequent return to starting position.

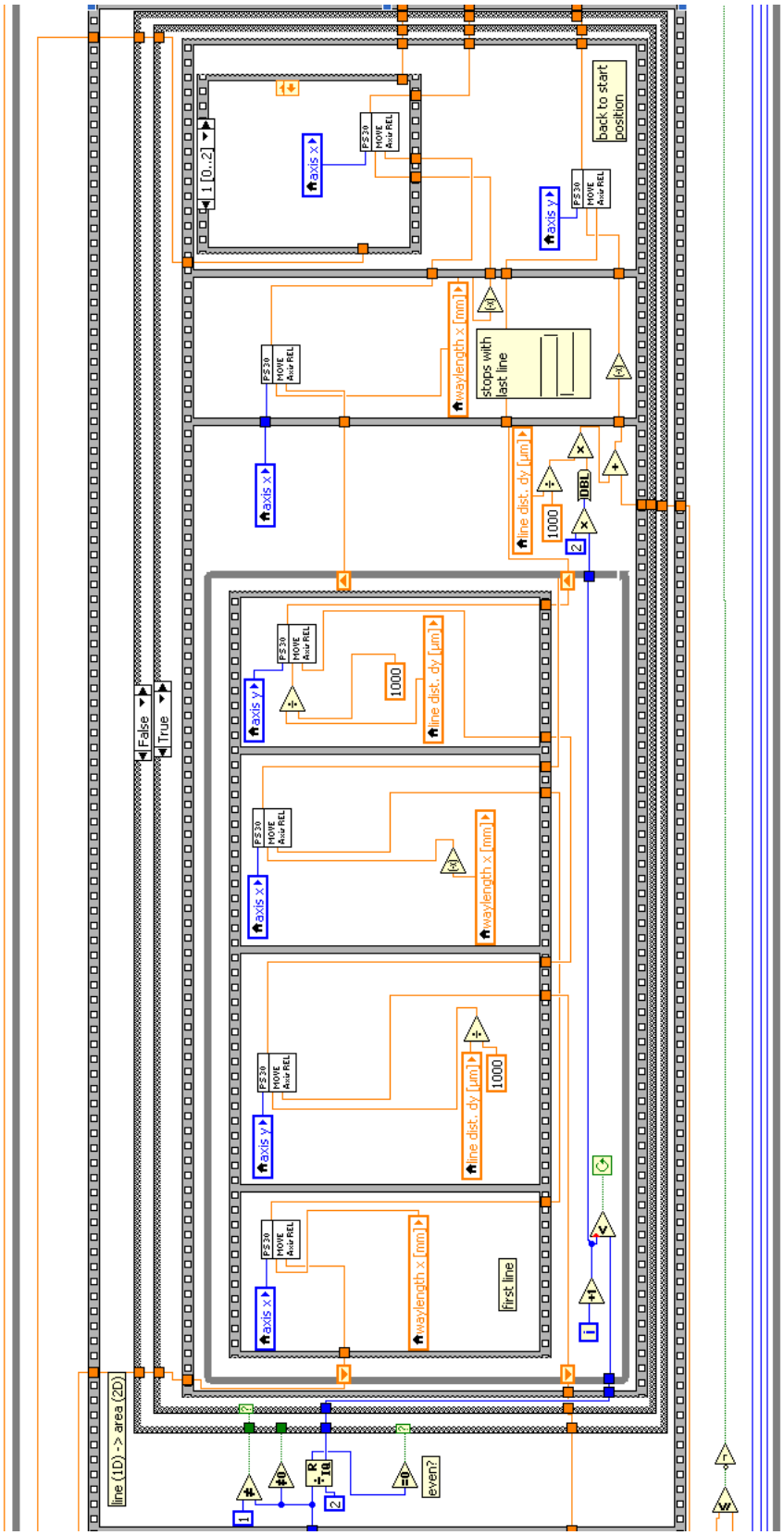

Figure A.3.: Block diagram part 2 case b: Loop to machine ablation layer with odd number of single lines. To return to starting position the stage is moved out of the focal plane.

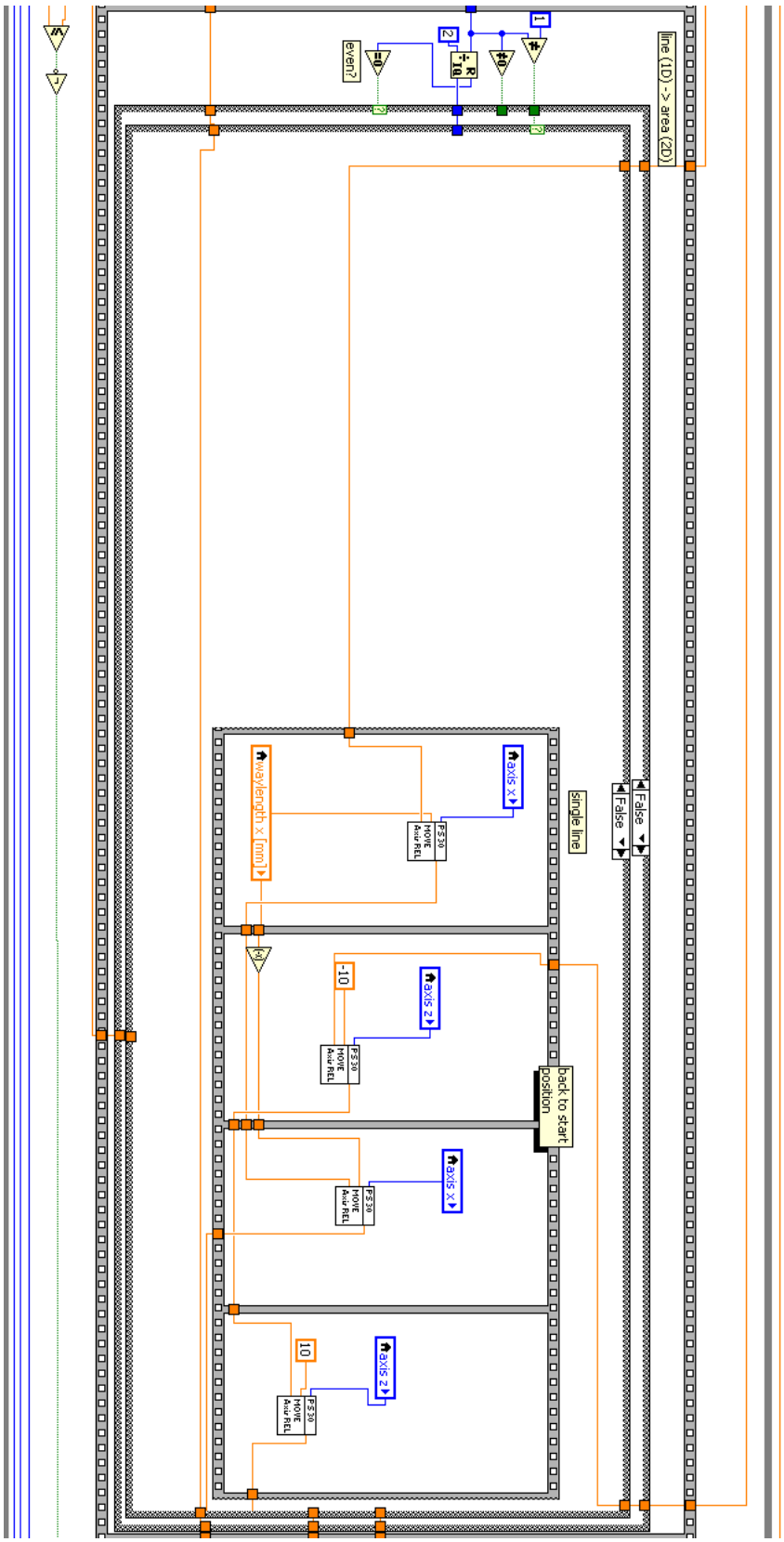

Figure A.4.: Block diagram part 2 case c: Machining of single line ablation layer and subsequent return to starting position.

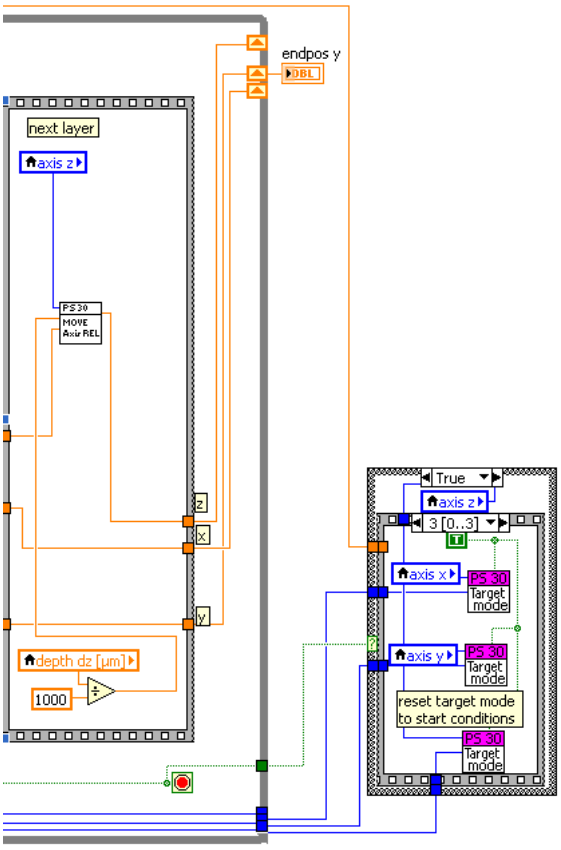

Figure A.5.: Block diagram part 3: Last part of the block diagram including the focal plane shift to get to next ablation layer and finally restoring of initial positioning parameters after capillary machining.

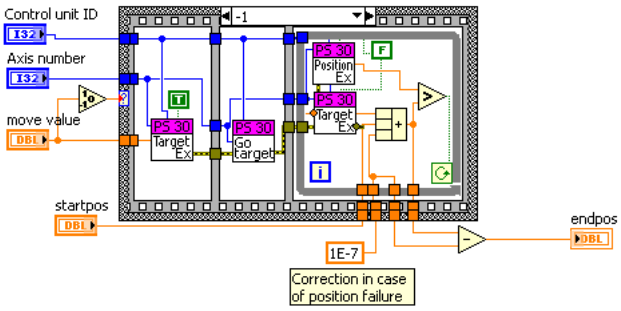

Figure A.6.: Sub-vi "Move Axis REL": Initiating of and time delay for axis movement. The pictured block corresponds to negative direction with respect to the internal coordinate system of the motor.

B. Setup

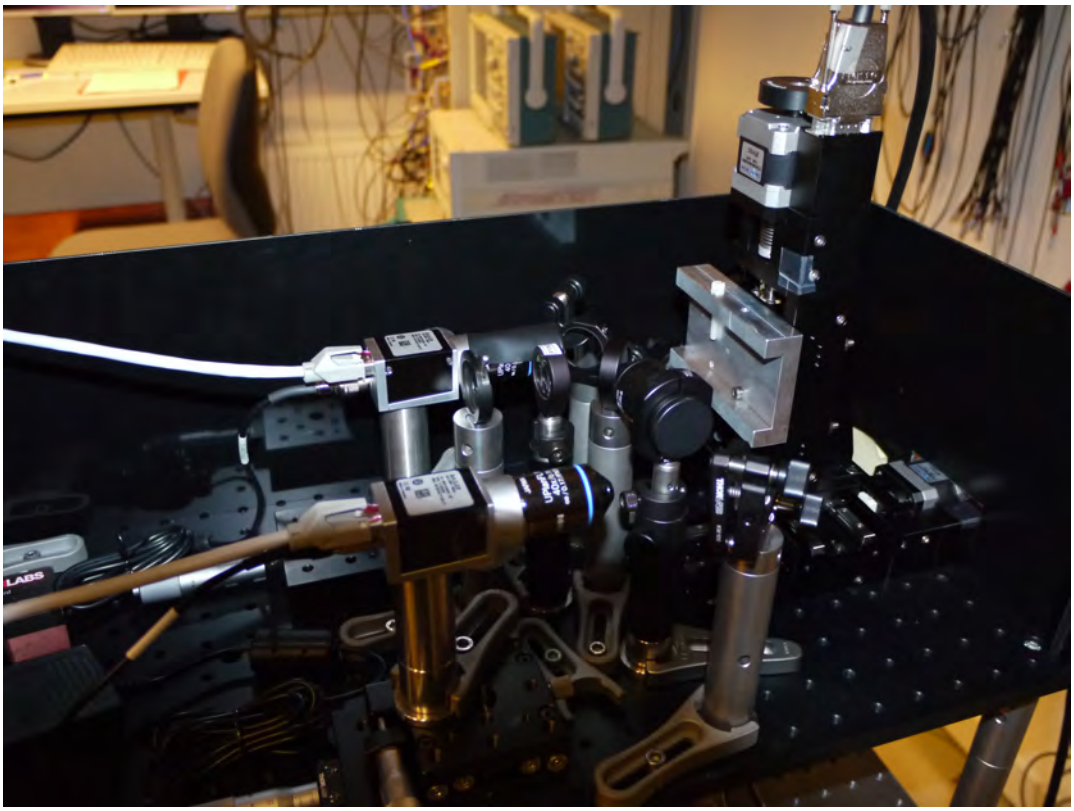

Figure B.1.: Machining device

C. Capillary holder

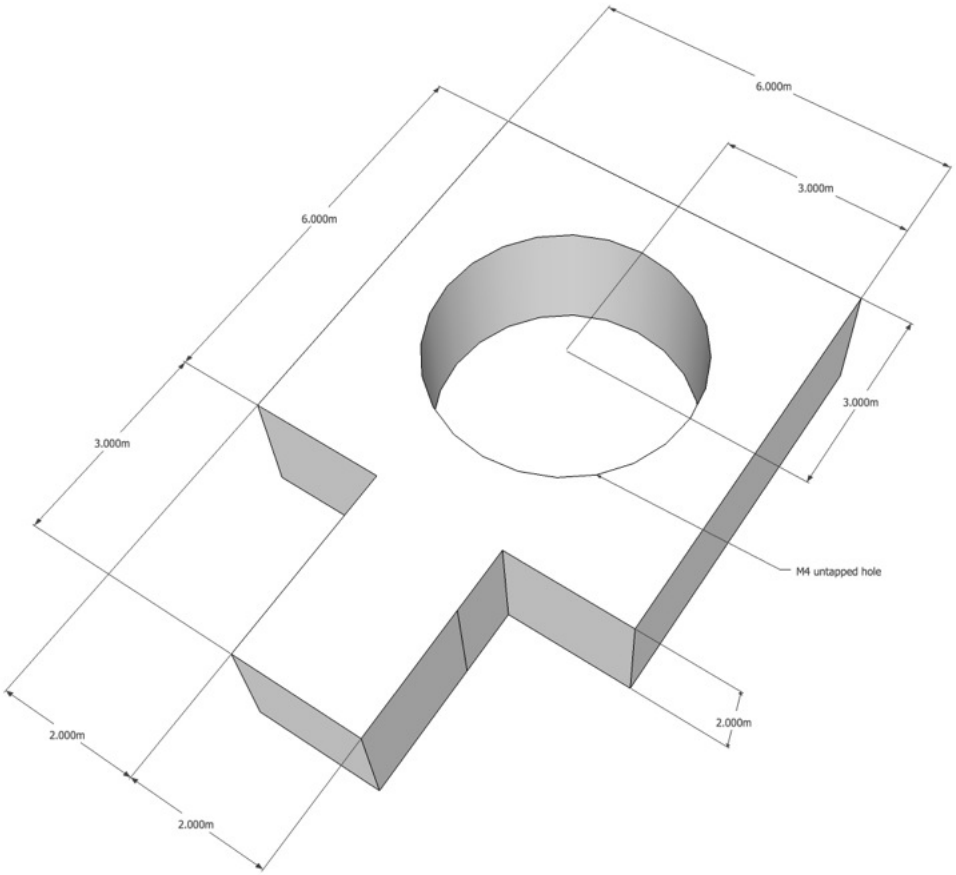

Figure C.1.: Flexible counter nip holding the crystal at the front surface. Can be placed as desired allowing for free inlet placement. (By courtesy of C. Palmer)

Figure C.2.: Capillary mount. Left-hand side hole to place the sapphire crystals and right-hand side slots for stage mounting. (By courtesy of C. Palmer)

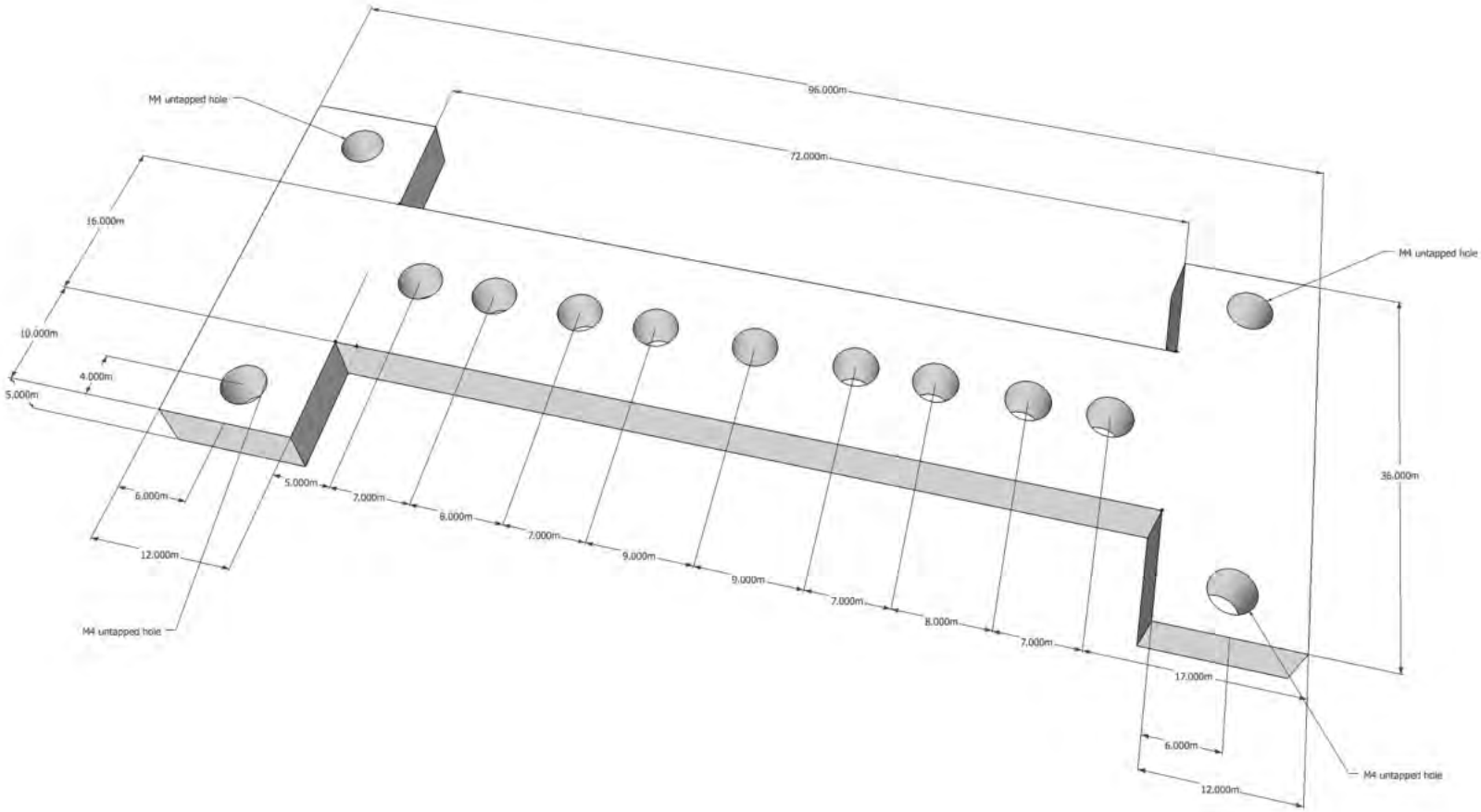

Figure C.3.: Backplate to fix the crystals. (By courtesy of C. Palmer)

Bibliography

[ADK86] M. V. Ammosov, N. B. Delone, and V. P. Krainov. Tunnel ionization of complex atoms and atomic ions in an alternating electromagnetic field. *Soviet Physics, Journal Of Experimental and Theoretical Physics*, 64(6):1191–1194, 1986.

[Alp11] Wolfram Alpha. Strehl ratio. http://www.wolframalpha.com/input/?i=Strehl+ratio, 2011.

[ARV+97] D Ashkenasi, A Rosenfeld, H Varel, M Wähmer, and E.E.B Campbell. Laser processing of sapphire with picosecond and sub-picosecond pulses. *Applied Surface Science*, 120(1-2):65 – 80, November 1997.

[Bal01] Ball. Theory of raman spectroscopy. *Spectroscopy*, 16(11):32–34, 2001.

[Bal02] D. W. Ball. Raman spectroscopy. *Spectroscopy*, 17(2):50–52, 2002.

[BCS11] Philippe Bado, William Clark, and Ali Said. Micromachining handbook. http://www.cmxr.com/Education/Introduction.html, 2011.

[BG49] D. Bohm and E. P. Gross. Theory of plasma oscillations. a. origin of medium-like behavior. *Physical Review*, 75(12):1851–1864, 1949.

[BIK+92] S. Bulanov, I. N. Inovenko, V. I. Kirsanov, N. M. Naumova, and A. S. Sakharov. Nonlinear depletion of ultrashort and relativistically strong laser pulses in an underdense plasma. *Physics of Fluids B: Plasma Physics*, 4(7):1935–1942, 1992.

[BMS95] D. Bauer, P. Mulser, and W.-H. Steeb. Relativistic ponderomotive force, uphill acceleration, and transition to chaos. *Physical Review Letters*, 75(25):4622–4625, 1995.

[BNPS98] S. Bulanov, N. Naumova, F. Pegoraro, and J. Sakai. Particle injection into the wave acceleration phase due to nonlinear wake wave breaking. *Phys. Rev. E*, 58(5):R5257–R5260, Nov 1998.

[Bri26] L. Brillouin. La méchanique ondulatoire de Schrödinger: une méthode générale de resolution par approximations successives. *Comptes rendus de l'Académie des sciences*, 183:24–26, 1926.

[BW99] Max Born and Emil Wolf. *Principles of Optics: Electromagnetic theory of propagation, interference and diffraction of light*. Cambridge University Press, Cambridge, 1999.

[BWH+09] Stephan BARCIKOWSKI, Jürgen WALTER, Anne HAHN, Jürgen KOCH, Hatim HALOUI, Thomas HERRMANN, and Antonietta GATTI. Picosecond and femtosecond laser machining may cause health risks related to nanoparticle emission. *JLMN-Journal of Laser Micro/Nanoengineering*, 4(3):159–164, December 2009.

[CES+12] M. Chen, E. Esarey, C. B. Schroeder, C. G. R. Geddes, and W. P. Leemans. Theory of ionization-induced trapping in laser-plasma accelerators. *Physics of Plasmas*, 19(3):033101, 2012.

[Dem07] Wolfgang Demtröder. *Laserspektroskopie*. Springer Berlin / Heidelberg, 5 edition, 2007.

[Dir27] P. A. M. Dirac. The quantum theory of the emission and absorption of radiation. *Proceedings of the Royal Society of London. Series A*, 114(767):243–265, 1927.

[Dre10] Markus Drescher. Ultrafast optical physics. Lecture notes, Universität Hamburg, 2010.

[EHHT98] E. Esarey, B. Hafizi, R. Hubbard, and A. Ting. Trapping and acceleration in self-modulated laser wakefields. *Phys. Rev. Lett.*, 80(25):5552–5555, Jun 1998.

[EHL+97] E. Esarey, R. F. Hubbard, W. P. Leemans, A. Ting, and P. Sprangle. Electron injection into plasma wakefields by colliding laser pulses. *Phys. Rev. Lett.*, 79(14):2682–2685, Oct 1997.

[Ein05] A. Einstein. Über einen die Erzeugung und Verwandlung des Lichtes betreffenden heurisrischen Gesichtspunkt. *Annalen der Physik*, 322(6):132–148, 1905.

[Ein09] A. Einstein. Über die Entwicklung unserer Anschauung über das Wesen und die Konstitution der Strahlung. *Physikalische Zeitschrift*, 10(22):817–825, 1909.

[EK35] H. Euler and B. Kockel. Über die Streuung von Licht an Licht nach der Diracschen Theorie. *Naturwisschenschaften*, 23(15):246–247, 1935.

[ESKT96] E. Esarey, P. Sprangle, J. Krall, and A. Ting. Overview of plasma-based accelerator concepts. *Plasma Science, IEEE Transactions on*, 24(2):252 –288, apr 1996.

[ESL09] E. Esarey, C. B. Schroeder, and W. P. Leemans. Physics of laser-driven plasma-based electron accelerators. *Rev. Mod. Phys.*, 81(3):1229–1285, Aug 2009.

[Fer50] E. Fermi. *Nuclear Physics*. University of Chicago Press, 1950.

[FESL06] G. Fubiani, E. Esarey, C. B. Schroeder, and W. P. Leemans. Improvement of electron beam quality in optical injection schemes using negative plasma density gradients. *Phys. Rev. E*, 73(2):026402, Feb 2006.

[FHPW61] P. A. Franken, A. E. Hill, C. W. Peters, and G. Weinreich. Generation of Optical Harmonics. *Phys. Rev. Lett.*, 7(4):118–119, Aug 1961.

[Fit06] R. Fitzpatrick. *Introduction to plasma physics: a graduate level course*. Lecture notes. The University of Texas at Austin, 2006.

[FP08] J. H. Ferziger and M. Perić. *Numerische Strömungsmechanik*. Springer-Verlag, Berlin Heidelberg, 2008.

[FRN+06] J. Faure, C. Rechatin, A. Norlin, A. Lifschitz, Y. Glinec, and V. Malka. Controlled injection and acceleration of electrons in plasma wakefields by colliding laser pulses. *Nature*, 444(7120):737–739, December 2006.

[GBS+07] F. Grüner, S. Becker, U. Schramm, T. Eichner, M. Fuchs, R. Weingartner, D. Habs, J. Meyer-ter Vehn, M. Geissler, M. Ferrario, L. Serafini, B. van der Geer, H. Backe, W. Lauth, and S. Reiche. Design considerations for table-top, laser-based vuv and x-ray free electron lasers. *Applied Physics B: Lasers and Optics*, 86(3):431–435, 2007. 10.1007/s00340-006-2565-7.

[GCME+08] C. G. R. Geddes, E. Cormier-Michel, E. Esarey, K. Nakamura, G. R. Plateau, C. B. Schroeder, Cs. Toth, D. L. Bruhwiler, J. R. Cary, and W. P. Leemans. Plasma gradient controlled injection and postacceleration of high quality electron bunches. In *ADVANCED ACCELERATOR CONCEPTS: Proceedings of the Thirteenth Advanced Accelerator Concepts Workshop*, volume 1086 of *AIP Conference Proceedings*, pages 12–20. American Institute of Physics, 2008.

[GD63] J. H. Gladstone and T. P. Dale. Researches on the refraction, dispersion and sensitiveness of liquids. *Phil. Trans. R. Soc. Lond.*, 153:317–343, January 1863.

[Gib05] P. Gibbon. *Short pulse laser interaction with matter*. Imperial College Press, London, 2005.

[GM07] Antonietta Morena Gatti and Stefano Montanari. *Nanopathology - The Health Impact of Nanoparticles*. Pan Stanford Publishing, 2007.

[GNP+08] C. G. R. Geddes, K. Nakamura, G. R. Plateau, Cs. Toth, E. Cormier-Michel, E. Esarey, C. B. Schroeder, J. R. Cary, and W. P. Leemans. Plasma-density-gradient injection of low absolute-momentum-spread electron bunches. *Phys. Rev. Lett.*, 100(21):215004, May 2008.

[GR98] R. J. Goldston and P. H. Rutherford. *Plasmaphysik - Eine Einführung*. Vieweg Verlag, 1998.

[GRRB+07] A. J. Gonsalves, T. P. Rowlands-Rees, B. H. P. Broks, J. J. A. M. van der Mullen, and S. M. Hooker. Transverse interferometry of a hydrogen-filled capillary discharge waveguide. *Phys. Rev. Lett.*, 98:025002, Jan 2007.

[Hec91] Eugene Hecht. *Optik*. Addison-Wesley, Bonn, 1991.

[HLL+07] Richard Haglund, Norbert Lindlein, Gerd Leuchs, Aleksei Zheltikov, Anne L'Huillier, Ferenc Krausz, Matthias Brinkmann, Joseph Hayden, Martin Letz, Steffen Reichel, Carol Click, Wolfgang Mannstadt, Bianca Schreder, Silke Wolff, Simone Ritter, Mark J. Davis, Thomas E. Bauer, Hongwen Ren, Yun-Hsing Fan, Shin-Tson Wu, Klaus Bonrad, Eckhard Krätzig, Karsten Buse, Roger A. Paquin, Detlev Ristau, Henrik Ehlers, Mary G. Turner, Robert P. Breault, Robert Brunner, Enrico Geißler, Bernhard Messerschmidt, Dietrich Martin, Elisabeth Soergel, Kuon Inoue, Kazuo Ohtaka, Ajoy Ghatak, Alexander Goushcha, Bernd Tabbert, Dietrich Bertram, Matthias Born, Thomas Jüstel, Orazio Svelto, Stefano Longhi, Giuseppe Della Valle, Stefan Kück, Günter Huber, Markus Pollnau, Hartmut Hillmer, Stefan Hansmann, Rainer Engelbrecht, Hans Brand, Jeffrey Kaiser, Alan B. Peterson, Ralf Malz, Steffen Steinberg, Gerd Marowsky, Uwe Brinkmann, Dennis Lo, Annette Borsutzky, Helen Wächter, Markus W. Sigrist, Evgeny Saldin, Evgeny Schneidmiller, Mikhail Yurkov, Katsumi Midorokawa, Joachim Hein, Roland Sauerbrey, Jürgen Helmcke, Matthias Wollenhaupt, Andreas Assion, Thomas Baumert, Wolfgang Demtröder, Sune Svanberg, Gerard Milburn, Motoichi Ohtsu, Stefan W. Hell, Daniel Grischkowsky, Christian G. Schroer, Bruno Langeler, Ulrich Platt, Klaus Pfeilsticker, Michael Vollmer, Mirco Imlau, Martin Falley, Hans Coufal, Geoffrey W. Bur, Glenn T. Sincerbox, and Hans-Dieter Reidenbach. *Springer Handbook of Lasers and Optics*. Springer Science+Business Media, LLC New York, 2007.

[Jac75] J. D. Jackson. *Classical electrodynamics*. John Wiley & Sons, New York, 2nd edition, 1975.

[JTK+03] T.G. Jones, A. Ting, D. Kaganovich, C. I. Moore, and P. Sprangle. Spatially resolved interferometric measurement of a discharge capillary plasma channel. *Physics of Plasmas*, 10(11):4504–4512, 2003.

[JZK06] Jan Jabczynski, Waldemar Zendzian, and Jacek Kwiatkowski. Q-switched mode locking with acousto-optic modulator in a diode-pumped Nd:YVO_4 laser. *Opt. Express*, 14(6):2184–2190, Mar 2006.

[Kel65] L. V. Keldysh. Ionization in the field of a strong electromagnetic wave. *Soviet Physics, Journal Of Experimental and Theoretical Physics*, 79(24):4810–1813, 1965.

[KLI+06] A.G. Khachatryan, M.J.H. Luttikhof, A. Irman, F.A. van Goor, J.W.J. Verschuur, H.M.J. Bastiaens, and K.-J. Boller. Conceptual design of a laser wakefield acceleration experiment with external bunch injection. *Nuclear Instruments and Methods in Physics Research Section A: Accelerators, Spectrometers, Detectors and Associated Equipment*, 566(2):244 – 249, 2006.

[Kra26] H. A. Kramers. Wellenmechanik und halbzahlige Quantisierung. *Zeitschrift für Physik*, 39(11):828–840, 1926.

[KSCZ99] D. Kaganovich, P. Sasorov, C. Cohen, and A. Zigler. Variable profile capillary discharge for improved phase matching in a laser wakefield accelerator. *Applied Physics Letters*, 75(6):772, June 1999.

[Law79] J. D. Lawson. Lasers and accelerators. *IEEE Transactions on Nuclear Science*, 26(9):4217–4219, 1979.

[Liu82] J. M. Liu. Simple technique for measurements of pulsed gaussian-beam spot sizes. *Opt. Lett.*, 7(5):196–198, May 1982.

[LNG+06] W. P. Leemans, B. Nagler, A. J. Gonsalves, Cs. Toth, K. Nakamura, C. G. R. Geddes, E. Esarey, C. B. Schroeder, and S. M. Hooker. Gev electron beams from a centimetre-scale accelerator. *Nat Phys*, 2(10):696–699, October 2006.

[LSE+96] W. P. Leemans, C. W. Siders, E. Esarey, N. E. Andreev, G. Shvets, and W. B. Mori. Plasma guiding and wakefield generation for second-generation experiments. *IEEE Transactions on Plasma Science*, 24(2):331–342, 1996.

[Mar08] Benjamin Marx. Interferometrie eines plasmadichtegradienten in einer gasentladungskapillare. Diplomarbeit, Ludwig-Maximilians-Universität München, München, 2008.

[Max61] J. C. Maxwell. On physical lines of force. *The London, Edingburgh and Dublin Philosophical Magazine and Journal of Science*, 21(139):161 et seq., 1861.

[Mey97] D. D. Meyerhofer. High-intensity-laser-electron scattering. *IEEE Journal of Quantum Electronics*, 33(11):1935–1941, 1997.

[MH62] F. J. McClung and R. W. Hellwarth. Giant Optical Pulsations from Ruby. *Journal of Applied Physics*, 33(3):828–829, March 1962.

[MKM95] C. I. Moore, J. P. Knauer, and D. D. Meyerhofer. Observation of the transition from thomson to compton scattering in multiphoton interactions with low-energy electrons. *Physical Review Letters*, 74(13):3439–2442, 1995.

[MM91] G. Mainfray and G. Manus. Multiphoton ionization of atoms. *Reports on Progress in Physics*, 54(10):1333–1372, 1991.

[MND+95] A. Modena, Z. Najmudin, A. Dangor, C. Clayton, K. A. Marsh, C. Joshi, V. Malka, C. Darrow, C. Danson, D. Neely, and F. Walsh. Electron acceleration from the breaking of relativistic plasma waves. *Nature*, 377(6550):606–608, October 1995.

[Mou86] P. F. Moulton. Spectroscopic and laser characteristics of Ti:Al_2O_3. *J. Opt. Soc. Am. B*, 3(1):125–133, Jan 1986.

[MSB+88] P. Maine, D. Strickland, P. Bado, M. Pessot, and G. Mourou. Generation of ultrahigh peak power pulses by chirped pulse amplification. *Quantum Electronics, IEEE Journal of*, 24(2):398 –403, feb 1988.

[ODK+07] E. Oz, S. Deng, T. Katsouleas, P. Muggli, C. D. Barnes, I. Blumenfeld, F. J. Decker, P. Emma, M. J. Hogan, R. Ischebeck, R. H. Iverson, N. Kirby, P. Krejcik, C. O'Connell, R. H. Siemann, D. Walz, D. Auerbach, C. E. Clayton, C. Huang, D. K. Johnson, C. Joshi, W. Lu, K. A. Marsh, W. B. Mori, and M. Zhou. Ionization-induced electron trapping in ultrarelativistic plasma wakes. *Phys. Rev. Lett.*, 98:084801, Feb 2007.

[Ope11] OpenFOAM. http://www.openfoam.org/, 2011.

[Ost09] Jens Osterhoff. *Stable, ultra-relativistic electron beams by laser-wakefield acceleration*. Dissertation, Ludwig-Maximilians-Universität München, München, February 2009.

[Ost11] Jens Osterhoff. Physik der Laser-Plasma-Beschleunigung. Lecture notes, Universität Hamburg, 2011.

[PHH89] D. M. Pennington, M. A. Heinesian, and R. W. Hellwarth. Nonlinear index of air at 1.503μm. *Physical Review A*, 39(6):3003–3009, 1989.

[Pla01] Max Planck. Ueber das Gesetz der Energieverteilung im Normalspectrum. *Annalen der Physik*, 309(3):553–563, 1901.

[Poy20] J. H. Poynting. *Collected scientific papers*. Cambridge University Press, London, 1920.

[PPT66] A. M. Perelomov, V. S. Popov, and M. V. Terent'ev. Ionization of atoms in an alternating electric field. *Soviet Physics, Journal Of Experimental and Theoretical Physics*, 23:924–934, 1966.

[QM98] B. Quesnal and P. Mora. Theory and simulation of the interaction of ultraintense laser pulses with electrons in vacuum. *Physical Review E*, 58(3):3719–3732, 1998.

[RK28] C. V. Raman and K. S. Krishnan. A new type of secondary radiation. *Nature*, 121:501, 1928.

[RSE+10] W. Rittershofer, C. B. Schroeder, E. Esarey, F. J. Grüner, and W. P. Leemans. Tapered plasma channels to phase-lock accelerating and focusing forces in laser-plasma accelerators. *Physics of Plasmas*, 17(6):063104, 2010.

[SBH99] D. J. Spence, P. D. S. Burnett, and S. M. Hooker. Measurement of the electron-density profile in a discharge-ablated capillary waveguide. *Opt. Lett.*, 24(14):993–995, Jul 1999.

[SFH+96a] B. C. Stuart, M. D. Feit, S. Herman, A. M. Rubenchik, B. W. Shore, and M. D. Perry. Nanosecond-to-femtosecond laser-induced breakdown in dielectrics. *Phys. Rev. B*, 53:1749–1761, Jan 1996.

[SFH+96b] B. C. Stuart, M. D. Feit, S. Herman, A. M. Rubenchik, B. W. Shore, and M. D. Perry. Optical ablation by high-power short-pulse lasers. *J. Opt. Soc. Am. B*, 13(2):459–468, Feb 1996.

[Sie86] Anthony E. Siegman. *Lasers*. University Science Books, Mill Valley, 1986.

[SKS91] D. E. Spence, P. N. Kean, and W. Sibbett. 60-fsec pulses generation from a self-modelocked Ti:sapphire laser. *Optics Letters*, 16(1):42–44, 1991.

[SM85] Donna Strickland and Gerard Mourou. Compression of amplified chirped optical pulses. *Optics Communications*, 55(6):447 – 449, 1985.

[SM97] E. A. Stratsev and C. J. McKinstrie. Multiple scale derivation of the relativistic ponderomotive force. *Physical Review E*, 55(6):7527–7535, 1997.

[Sol09] N. A. Solyak. Gradient limitations in room temperature and superconducting acceleration structures. *AIP Conf. Proc.*, 1086:365–372, 2009.

[Spe08] Spectra-Physics, 1335 Terra Bella Avenue, Mountain View, CA 94043. *Spitfire Pro Ti:Sapphire Regenerative Amplifier Systems*, February 2008. User Manual.

[Str99] Lord Rayleigh (J. W. Strutt). On the transmission of light through an atmosphere containing small particles in suspension, and on the origin of the blue of the sky. *Philosophical Magazine*, 47(287):375–384, 1899.

[TBB94] D. Teychenné, G. Bonnaud, and J.-L. Bobin. Electrostatic and kinetic energies in the wake wave of a short laser pulse. *Physics of Plasmas*, 1(6):1771–1773, 1994.

[TBH+01] J. Thøgersen, A. Borowiec, H.K. Haugen, F.E. McNeill, and I.M. Stronach. X-ray emission from femtosecond laser micromachining. *Applied Physics A: Materials Science & Processing*, 73(3):361–363, 2001. 10.1007/s003390100741.

[TD79] T. Tajima and J. M. Dawson. Laser electron accelerator. *Phys. Rev. Lett.*, 43(4):267–270, Jul 1979.

[TES90] A. Ting, E. Esarey, and P. Sprangle. Nonlinear wake-field generation and relativistic focusing of intense laser pulses in plasma. *Physics of Fluids B: Plasma Physics*, 2(6):1390–1394, 1990.

[TGG+03] P. Tomassini, M. Galimberti, A. Giulietti, D. Giulietti, L. A. Gizzi, L. Labate, and F. Pegoraro. Production of high-quality electron beams in numerical experiments of laser wakefield acceleration with longitudinal wave breaking. *Phys. Rev. ST Accel. Beams*, 6(12):121301, Dec 2003.

[TMK97] K-C. Tzeng, W. B. Mori, and T. Katsouleas. Electron beam characteristics from laser-driven wave breaking. *Phys. Rev. Lett.*, 79(26):5258–5261, Dec 1997.

[UBC+07] O. Uteza, B. Bussière, F. Canova, J.-P. Chambaret, P. Delaporte, T. Itina, and M. Sentis. Damage threshold of sapphire in short and long pulse regime. In *Society of Photo-Optical Instrumentation Engineers (SPIE) Conference Series*, volume 6732 of *Society of Photo-Optical Instrumentation Engineers (SPIE) Conference Series*, July 2007.

[VEL99] P. Volfbeyn, E. Esarey, and W. P. Leemans. Guiding of laser pulses in plasma channels created by the ignitor-heater technique. *Physics of Plasmas*, 6(5):2269–2277, 1999.

[Web95] M. J. Weber. *CRC handbool of laser science and technology: optical materials*. CRC Press, Boca Raton, 1995.

[Wen26] G. Wentzel. Eine Verallgemeinerung der Quantenbedingungen für die Zwecke der Wellenmechanik. *Zeitschrift für Physik*, 38(7):518–529, 1926.

[WGS+11] T. Weineisen, B. Göppner, K. Schmid, M. Fuchs, H. Schröder, S. Karsch, and F. Grüner. Density measurement in a laser-plasma-accelerator capillary using raman scattering. *Phys. Rev. ST Accel. Beams*, 14:050705, May 2011.

[WHY+01] P. X. Wang, Y. K. Ho, X. Q. Yuan, Q. Kong, N. Cao, A. M. Sessler, E. Esarey, and Y. Nishida. Vacuum electron acceleration by an intense laser. *Applied Physics Letters*, 78(15):2253–2255, 2001.

[WLZ+04] X.C. Wang, G.C. Lim, H.Y. Zheng, F.L. Ng, W. Liu, and S.J. Chua. Femtosecond pulse laser ablation of sapphire in ambient air. *Applied Surface Science*, 228(1-4):221 – 226, April 2004.

[Woo47] P. M. Woodward. A method of calculating the field over a plane. *Journal of the Institution of Electrical Engineers*, 93:1554–1558, 1947.

[Wun12] Steffen Wunderlich. Electro-optic sampling of THz pulses at the CTR source at FLASH. Diplomarbeit, Universität Hamburg, Hamburg, März 2012.

Acknowledgments

First of all I would like to thank Dr. Jens Osterhoff, my supervisor, for the opportunity to perform the work on my thesis within this young group and to start my research on this new laser based field of science. Additionally he was kind enough to send me inter alia to a summer school on Laser-Plasma Acceleration.
Furthermore I am very grateful for the support of all my colleagues, who were always helpfully assisting me. Especially Matthias Schnepp has to be mentioned for introducing me to the laser system and for being available whenever major problems occurred.
Not to forget about Dr. Stephan Roth from HASYLAB. He provided the fancy microscope to investigate the produced gas targets.

Erklärung

Hiermit versichere ich, dass ich die vorliegende Arbeit selbstständig und nur unter der Verwendung der angegebenen Quellen und Hilfsmittel verfasst habe.
Ferner bin ich mit der Ausleihe meiner Arbeit einverstanden.

Hamburg, den 17. Mai 2012

Jan-Patrick Schwinkendorf